

**Dynamic Pore-Scale Network Modelling:
A study of rheological behavior in porous media**

Master's Thesis
Petroleum Technology - Reservoir Physics

Anders Dalva



Department of Physics and Technology

University of Bergen

June 2019

Acknowledgement

I would like to thank my supervisor Professor Arne Skauge for his support and encouragement during my time as a master's student. Arne has shown a genuine interest in the topic of my master's thesis, and has provided close follow up during my study.

Further, I would also like to express my gratitude towards Iselin Cecilie Salmo and Nematollah Zamani at NORCE (Norwegian Research Centre). Their time and effort helping troubleshoot the code and discussing results have been most helpful.

I would also like to thank all my fellow master's students at Reservoir Physics and Reservoir Chemistry for all the helpful discussions on and off topic during my final two years here.

Finally, I want to thank my family and friends for their love and support.

Anders Dalva

Bergen, June 2019

Abstract

The global energy demand is rising and expected to continue increasing towards 2050. Several oil fields are produced with water and/or gas injection. This can leave large volumes of residual oil in the reservoir due to heavy oil or large reservoir heterogeneities. Polymer flooding is an enhanced oil recovery technique developed to gain a more favorable mobility ratio between the injected solution and the oil. Polymers can influence the volumetric sweep of the reservoir, but may also improve microscopic sweep by mobilizing trapped oil or by diverting the flow to recover bypassed oil.

Polymer solutions are non-Newtonian fluids that can change viscosity depending on the flow rate. An important question that has been discussed is if polymer will reduce the residual oil saturation compared to waterflooding. Fluid flowing through porous media will encounter a variety of pore-sizes and therefore varying flow rates. A dynamic pore-scale network model capable of simulating two-phase polymer flow through a pore network is used in this thesis to investigate rheology behavior of various polymers.

The simulations in this thesis act as extensions to previous work done by Zamani et al. [1]. Oil recovery and local oil mobilization trends are investigated for adverse viscosity ratios. The polymer rheology models are allowed to exhibit one of four behaviors: shear thinning, shear thickening, Newtonian or a combination labeled as complex shear. These four models are tuned so that for a single-phase displacement, they show the same apparent viscosity at a constant injection rate. Further parameter sensitivities were tested, such as polymer concentration, coordination number, pore-size distribution, injection rate and network size (in two and three dimensions).

The polymer rheology models had higher oil recoveries when compared to waterflooding for all simulations. The polymer rheology models showed different behaviors, despite being tuned to the same apparent viscosity for a constant injection rate. This is seen at pore level, where different polymer models displaced different pore sizes. The differential pressure a polymer rheology is able to maintain prior to breakthrough was seen to correlate to recovery efficiency. Trends in oil recovery for the various polymer rheology models are found to be consistent throughout the simulations and agree well with similar experimental work. For the cases studied

in this thesis, and under the conditions set, the complex rheology proves to be the optimal model for maximum oil recovery.

Nomenclature

Variables (Roman):

A	area	m^2
C	concentration	$kg \cdot m^{-3}$
d	diameter	m
E_R	recovery factor	[-]
F	force	N
F_w	fractional flow for water	[-]
f_j	fraction of bonds allowed to phase j	[-]
G	cross-sectional geometry for non-circular geometry	shape factor [-]
G_j	single-phase conductance to phase j	$m^4/(N \cdot s)$
g	bond conductivity	$m^5/(N \cdot s)$
K	absolute permeability	m^2
k_i	effective permeability	m^2
k_r	relative permeability	[-]
L, l	length	m
M	mass	kg
M^*	mobility ratio	[-]
n_1	slope of shear thinning curve	[-]
n_2	slope of shear thickening curve	[-]
N_{De}	Deborah number	[-]
P, p	pressure	Pa
Q	injection rate	$m^3 \cdot s^{-1}$
Q, q	flow rate	$m^3 \cdot s^{-1}$
R, r	radius, inscribed radius	m
S	saturation	[-]
u	Darcy velocity	$m \cdot s^{-1}$
v	velocity	$m \cdot s^{-1}$
V	volume	m^3
z	coordination number	[-]

Variables (greek):

α	shift between in-situ and bulk viscosity	[-]
β	pore half-angle	[degree/radian]
Δ	difference	[-]
μ	viscosity	Pa·s
μ_∞	high Newtonian shear rate plateau	Pa·s
μ_p^0	low Newtonian shear rate plateau	Pa·s
$\overline{\mu}_p$	apparent viscosity	Pa·s

λ	switch parameter	[-]
λ_p	onset of shear thinning	[-]
θ	contact angle	[degree/radian]
θ_f	liquid relaxation time	s
θ_p	transmit time	s
ρ	probability that a bond has hydraulic conductance	[-]
σ	interfacial tension	N·m ⁻¹
σ	standard deviation	[-]
$\dot{\gamma}$	shear rate	s ⁻¹
η	shear dependent viscosity	Pa·s
τ	shear stress	Pa
τ_r	onset of shear thickening	[-]

Subscripts:

A	areal
app	apparent
b	bulk
c	capillary
c	critical
D	microscopic
el	elongational
i	irreducible
i,j	phases i,j – nodes i,j
inj	injection
inj	injected
max	maximum
nw	non-wetting
o	oil
p	polymer
p	pore
r	residual
sh	shear
t	time
V	vertical
vol	volume
w	water
w	wetting

Abbreviations:

2D	two dimensional
3D	three dimensional

AM	arc meniscus
BT	breakthrough
CF	capillary forces
EOR	enhanced oil recovery
FW	fractional-wet
HPAM	hydrolyzed polyacrylamide
IOR	improved oil recovery
MTM	main terminal meniscus
MWL	mixed-wet large
MWS	mixed-wet small
PD	primary drainage
PNM	pore network model
PSD	pore size distribution
PV	pore volume
VF	viscous forces
VR, M	viscosity ratio

Table of Contents

Acknowledgement	iii
Abstract.....	v
Nomenclature	vii
Table of Contents	xi
1 Introduction	1
2 Enhanced Oil Recovery.....	5
2.1 Mobility Ratio.....	6
2.2 Oil Trapping.....	7
2.3 Capillary Number.....	9
2.4 Polymer Flooding.....	10
3 Properties of Porous Media	13
3.1 Petrophysical quantities	13
3.2 Wettability.....	14
3.3 Capillary Pressure.....	16
3.4 Drainage, Imbibition and hysteresis.....	18
4 Pore Network Model Overview	21
4.1 Percolation Theory.....	22
4.2 Quasi-static Approach.....	22
4.3 Properties of Quasi-static models with film behavior	23
5 Polymers	29
5.1 Rheology.....	29
5.2 Bulk and In-situ Rheology	31
5.3 Polymer Viscoelasticity	34
6 Dynamic Pore network Model.....	35
6.1 Dynamic Imbibition Pore Network Model of Li (2016).....	35
6.2 Modified Model including Polymer flow	38
6.3 Previous work using the dynamic pore network model	41
7 Results and discussion	45
7.1 Secondary Injection at Adverse Viscosity Ratios (M).....	49
7.2 Increasing polymer concentration	55
7.3 Reducing coordination number	61
7.4 Altering Pore Size Distribution	65
7.4.1 “Large Pores” Pore Size Distribution.....	67
7.4.2 Uniform Pore Size Distribution	71
7.5 Reducing Injection Rate.....	75
7.6 Expanding Network Length	81
7.7 Network Model Expanded to Three Dimensions (3D).....	85
8 Summary and Conclusions	89

8.1	<i>Summary of sensitivity analysis</i>	89
8.2	<i>Main observations</i>	92
8.3	<i>Conclusions</i>	95
9	Further work	97
	References	99
	Appendix A	104
	<i>A.1: Adverse Viscosity Ratio extended to 2.5 PV injected</i>	<i>104</i>
	<i>A.2: Pressure spike in 2D model: 100 x 25 x 1</i>	<i>105</i>

1 Introduction

The global population is expected to grow to 9.8 billion people by 2050 [2]. Growth and prosperity is particularly noticeable in emerging markets such as China and India. These regions will demand more goods and services that require energy [3]. The development in TPED (total primary energy demand) is shown in Figure 1.1 for key regions. The energy mix of 2015 was dominated by fossil fuels with an 82 % share in TPED. In a recently published report, “Energy Perspectives” by Equinor, a scenario-based prediction of the fuel-mix in 2050 was presented in Figure 1.1. Predicting the future oil demand is difficult and highly scenario dependent and is expected to vary from 59 to 122 million barrels per day (mbd), from 95 mbd in 2015.

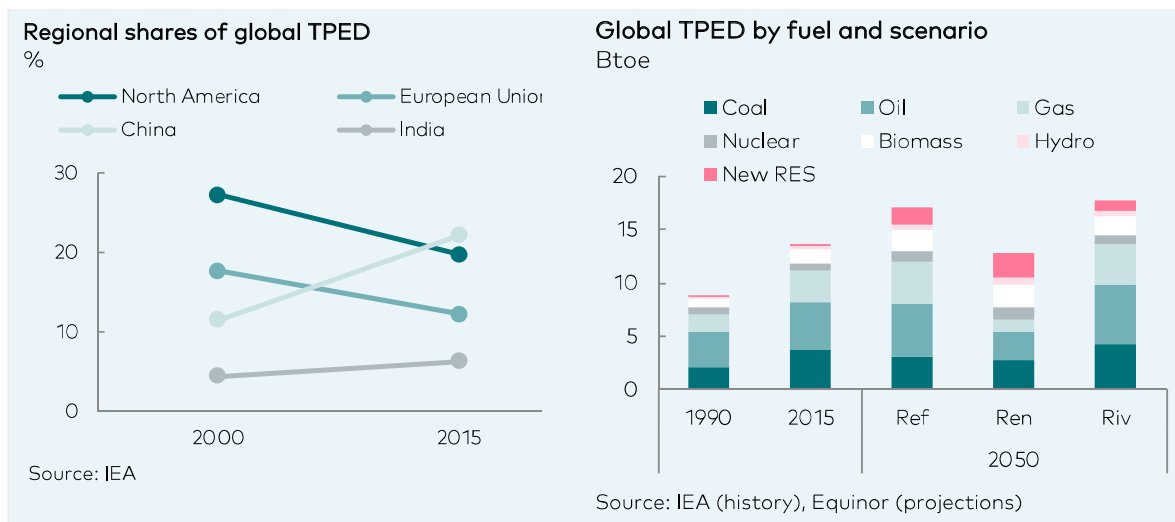


Figure 1.1 Left: The development in total primary energy demand (TPED) from the year 2000 to 2015 for key regions. Right: The historic development in global TPED from 1990 to 2015 and future projections based on a variety of scenarios. Figures from Equinor [3].

In order to meet the growing energy demand, methods of producing oil reservoirs efficiently and economically have been extensively studied. Water and gas flooding are oil recovery techniques where the aim is to recover as much of the oil as possible while simultaneously maintaining low operating costs. These have proven to be very effective at the Norwegian Continental Shelf (NCS). Many fields at the NCS carry light oils that may be efficiently produced using water flooding. In many other cases where there are dipping, high permeable reservoirs, gas injection is often preferred over waterflooding [4]. The result is that almost 50 per cent of the oil is recovered at the NCS [5] compared to the 22 per cent worldwide average

[6]. Studying gas floods is not part of the objective of this thesis, and is therefore only mentioned here.

Reservoirs are to some degree heterogeneous entities, meaning in this context that some layers are more easily flooded within the structure. When water is injected, it will follow the path of least resistance towards the producer, thereby bypassing potentially large volumes of oil. Once water has reached the producer, it tends to flow mostly in its own path. As more and more of the oil is produced, the amount of water produced increases until the well is no longer deemed economically viable, and shut down.

With the current methods employed at the NCS, about 50 per cent of the oil is left behind in the reservoirs. As this is an average value across the NCS, there are several fields with much residual oil left behind. Enhanced Oil Recovery (EOR) techniques have been developed to target the residual oil. One of these methods is polymer flooding, where polymer molecules are mixed with water, yielding a solution with more favorable characteristics. Firstly, the polymers increase the injected fluids viscosity, secondly the polymer solution shows non-Newtonian behavior, meaning its viscosity will vary depending on the flow conditions. By increasing the solution viscosity, a more favorable mobility ratio is achieved, sweeping the reservoir more efficiently.

There are several polymer projects planned for the UK North Sea. Chevron's Captain Field is a heavy-oil field with oil viscosities of 85cP, where the expected incremental oil recovery from polymer EOR is 5% [7]. Other polymer projects in the UK are the BP operated Schiehallion and Loyal fields and the Equinor operated Mariner Field which consists of two formations with oil viscosities 67cP and 508cP respectively. EOR pilots have been carried out at the NCS as well, e.g. for the Heidrun and Johan Sverdrup Fields. In regions with large onshore operations, polymer flooding has been applied successfully for more than 20 years and is now considered a mature EOR technique.

In recent years, experimental [8] and numerical [9]–[11] studies have shown that polymer flooding may reduce residual oil saturation on a microscopic level. In addition to increasing the viscosity, the polymer solutions are thought to obtain viscoelastic and shear thickening effects.

To evaluate the effect these phenomena have on a macroscopic field- or core-scale, there is a need to understand underlying physics of fluid flow on a microscopic scale. Reservoir rocks

consist of grains with large networks of interconnected void spaces between them. The physics of multiphase flow through such networks is complex and not yet fully understood. Several attempts have been made to describe the processes that occur at the pore level by the use of pore-scale network models (PNM). These models seek to mimic the properties and behavior of the real porous media investigated.

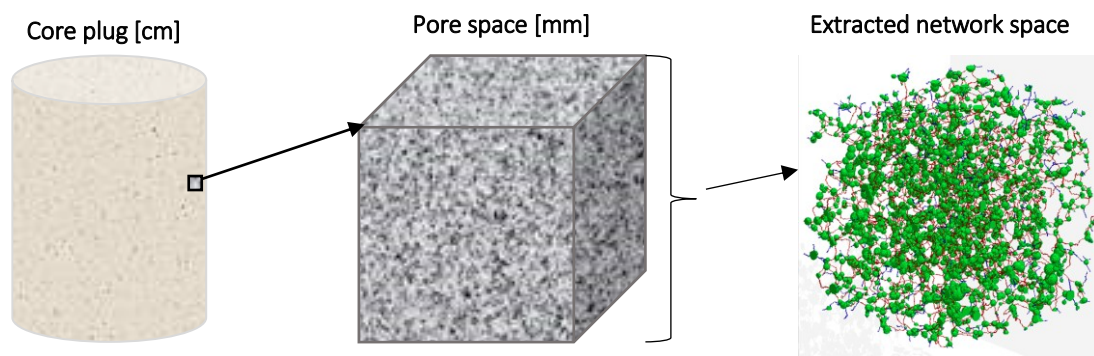


Figure 1.2: Visualization of the relative size investigated in pore-scale network models to a core plug. Modified from Skauge [4].

In 2016, Juan Li introduced a dynamic PNM that was able to simulate two-phase imbibition displacements with the ability to incorporate piston-like and snap-off displacements [12]. A modified version of this code was developed by Zamani et al. to include single and two-phase polymer flow with the ability to simulate different types of rheological behavior [1].

The main network properties of their sensitivity analysis is used as a starting point for this thesis. Further sensitivity testing is carried out in this work, modeling the in-situ rheology behavior across a variety of network parameters. The thesis addresses the question of possible changes in microscopic displacement efficiency as a function of polymer non-Newtonian behavior and contrast in viscosity ratio between oil and water. The key objectives of this thesis are to (i) test the pore-scale network code with the aim to employ the code for mechanistic studies of polymer flooding. The effect of oil viscosity, network geometry and size, injection rate and polymer concentration are tested. (ii) Investigate the impact of rheology on local oil mobilization. (iii) Evaluate if there exists an optimal rheology model under the conditions set.

2 Enhanced Oil Recovery

As the global energy demand is increasing, there is a need for better and more energy effective techniques of extracting oil from reservoirs. Technology intended to increase oil recovery is usually defined as Improved Oil Recovery (IOR) or Enhanced Oil Recovery (EOR) [13]. The distinction here is that IOR governs all economic measures that improve oil recovery factor or accelerate reserves [4]. EOR is usually defined as oil recovery by injection of materials not normally present in the reservoir.

When the first land-based oil reservoirs were produced, oil was produced by pressure depletion. Using this strategy, gas was released from the oil as soon as the pressure dropped below the bubble point resulting in a low ultimate recovery. A secondary recovery method, waterflooding, was used in order to sustain reservoir pressure and sweep more oil in a more efficient displacement process [14]. At the Norwegian Continental Shelf, waterflooding has been a huge success. Easy-to-produce light oil reservoirs, water availability offshore and low costs are main drivers for the success. The most prominent drawbacks of waterflooding are related to poor displacement efficiency for heavier oils and poor sweep efficiency in heterogeneous reservoirs. To realize the potential of oil recovery, implementation of EOR methods are evaluated for each case. Three main types of EOR operations are chemical flooding, miscible displacement and thermal recovery [15].

In a recent report, The Norwegian Petroleum Directorate assessed the EOR potential for the 27 largest fields on the NCS [16]. They found a technical EOR potential of 592MSm³. It was however stressed that financial, environmental and operational conditions were not accounted for. If say, 10 per cent of this potential yields profitable production, it would represent NOK 150 billion in gross sales at an oil price of USD 50 per barrel.

An important parameter in EOR is the recovery factor, and it is defined as [4]:

$$E_R = E_D \cdot E_{vol} = E_D \cdot E_A \cdot E_V \quad 2.1$$

where E_D is the microscopic displacement efficiency, E_{vol} is the volumetric displacement efficiency. E_{vol} can be expressed in terms of E_A : areal sweep efficiency and E_V : vertical sweep efficiency. Areal- and vertical sweep will be further addressed in Chapter 2.4.

2.1 Mobility Ratio

In order to assess how efficiently a fluid displaces another fluid it is necessary to introduce mobility and mobility ratio. Mobility is simply a ratio relating end-point effective permeability to the phase viscosity.

Mobility ratio (M^*) is the mobility of the displacing fluid to the mobility of the displaced fluid, for a waterflood, M^* can be expressed as [17]:

$$M^* = \frac{k_{rw}}{k_{ro}} \cdot \frac{\mu_o}{\mu_w} \quad 2.2$$

where k_{rw} and k_{ro} are the relative permeability to water and oil respectively. μ_o and μ_w are mobility of oil and water. It was chosen to denote the mobility ratio with a star (M^*) to avoid ambiguity with the viscosity ratio (M) later introduced in Chapter 7.

The mobility ratio can give valuable information about the displacement process. A lower mobility ratio can enable water to displace oil in a piston-like manner, whereas a higher mobility may induce instabilities and cause “viscous fingering”. Using polymers, water viscosity is increased hence reducing the mobility ratio. This will provide better sweep and delay water breakthrough. Polymer behavior (rheology) will be dealt with in detail in Chapter 5.

2.2 Oil Trapping

The oil left behind in the reservoir following a waterflood is called residual oil. The amount of trapped oil is a function of the displacement method and conditions, making it a target for EOR measures [18]. For a preferentially water-wet system, oil trapping can be explained by the snap-off and pore doublet models presented in Figure 2.1 and 2.2.

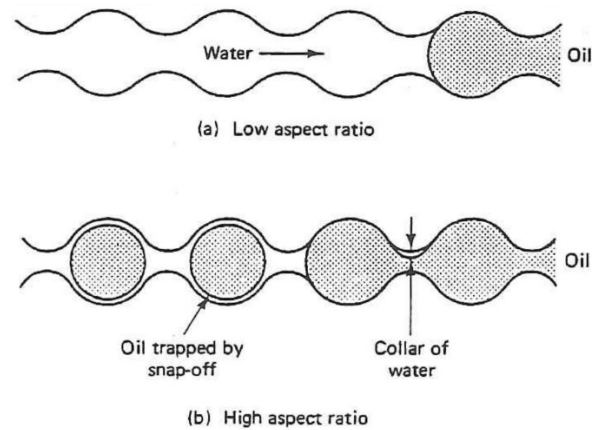


Figure 2.1: Snap-off model: (a) oil is displaced in a piston-like manner. (b) oil is left in pores as globules. Pore throats are narrower (high aspect ratio), water films swell and eventually snap off oil, Lake [13].

The purpose of including the snap-off model here is to illustrate how oil is left behind in a pore. There are several different factors influencing snap-off in a porous network. In chapter 3.4, a general description of how capillary pressure dictates what displacement type (piston-like or snap-off) is preferred for an imbibition process. The model used in this thesis however, encompasses that both displacement types can occur simultaneously. It evaluates the local competition between viscous and capillary forces within a pore to decide the magnitude of each displacement type. This model is introduced in chapter 6.1.

Oil can also be left behind as bypassed oil, and is commonly illustrated as in Figure 2.2. This trapping mechanism can affect both water and oil, depending on which is the wetting fluid. To avoid confusion using non-wetting and wetting terms, the model is described for a water-wet system.

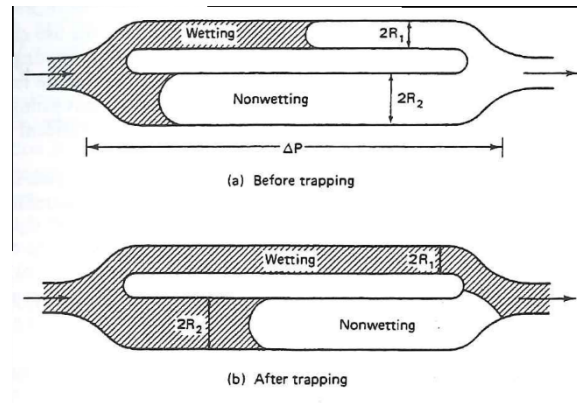


Figure 2.2: Pore-doublet model: (a) Water advances (imbibes) faster in smaller channel due to how radius influences capillary pressure. (b) Oil is left behind in larger pore because the invading water cannot overcome the capillary pressure needed to mobilize the oil, Lake [13].

Two adjacent paths containing oil are displaced simultaneously. Smaller sized pores will imbibe faster than larger pores and will form a continuous water phase at the outlet. The water pressure is unable to overcome the capillary pressure needed to mobilize the remaining oil left in the larger pore. This model shows clearly the effect pore radius has on oil trapping, and has been used mathematically to describe local capillary number. Chatzis et al. (1983) criticized the usage of this model to describe oil trapping at the microscopic level. They argued that the cross section of the pores in a doublet model would vary across its length. A more elaborate classification scheme was introduced where the snap-off model was incorporated into the pore-doublet model as shown in Figure 2.3.

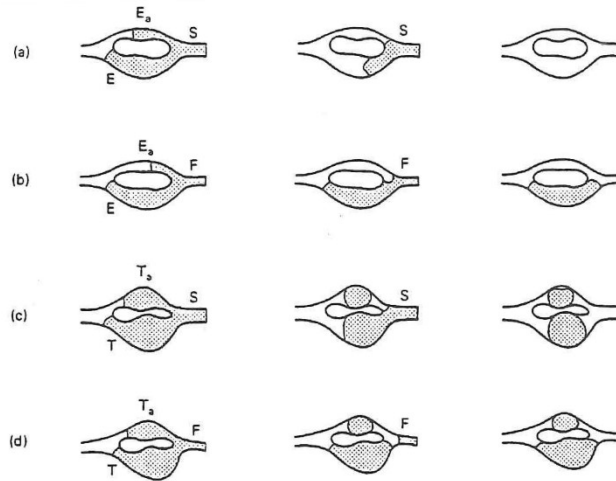


Figure 2.3: Pore-doublet trapping mechanisms, figures are read from left to right. (a) Oil is fully displaced, no trapping. (b) Oil is bypassed in larger pore. (c) Oil is trapped by snap-off in both pores. (d) A combination of snap-off and bypassed oil. (Extract from Chatzis et al. [19])

The emphasis of this model is to show that in real porous media snap-off may occur in pore-doublets in a number of different configurations. The configurations in Figure 2.3 (a-d) show some of the many trapping configurations that can occur in real porous media. The network model used in this study is capable of including all these mechanisms; piston-like displacement (no trapping), snap-off (immobile oil globule) and bypassed oil (capillary trapped oil).

2.3 Capillary Number

The capillary number is an important parameter when discussing microscopic displacement efficiency. It relates the dimensionless ratio between viscous and capillary forces. Equation 2.3 shows a common way to define it [4]:

$$N_{vc} = \frac{VF}{CF} = \frac{u \cdot \mu}{\sigma} \quad 2.3$$

Where u is the Darcy velocity of the displacing fluid, μ is the viscosity of the displacing fluid, and σ is the interfacial tension between the fluids. Experimental studies have shown that residual wetting and non-wetting saturation can be related to the capillary number as in Figure 2.4 [13].

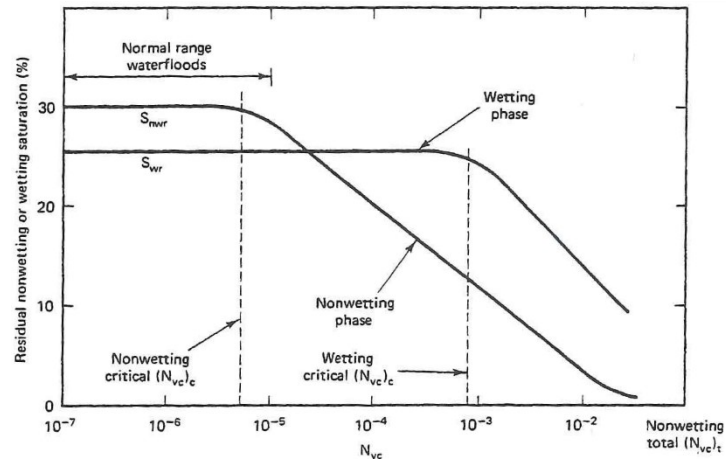


Figure 2.4: Capillary Desaturation Curve. Relates residual saturation (non-wetting and wetting) to the capillary number (Eq. 2.3) From Lake [13].

We can see from Figure 2.4 that the residual non-wetting (usually oil) saturation is at a plateau for water floods. If a water flood has a capillary number of 10^{-7} this means that the capillary forces are 10 million times stronger than the viscous forces. In order to reduce the residual oil saturation the capillary number has to be increased beyond the critical capillary number. This means increasing the capillary number by several orders of magnitude (logarithmic scale). In practice, this is only possible by reducing the interfacial tension, because increasing μ and u is limited by injection equipment. Other CDC schematics exist where the effects of varying pore-size distribution, pore-throat size distribution and how wetting states influence N_{vc} . Only the basic capillary desaturation curve is detailed here because they all have in common that they only show viscous effects. Polymers, which is the focus of this thesis, can show *viscoelastic* effects, thus reducing residual oil saturation, (see chapter 5.3).

2.4 Polymer Flooding

Polymer flooding is a recovery method where polymer is added to water to increase its viscosity. This viscosity increase results in a more favorable mobility ratio, providing better sweep efficiency. In addition to improving areal sweep (Figure 2.5), polymers also help stabilize contrasts in permeability between vertical layers (Figure 2.6) [14].

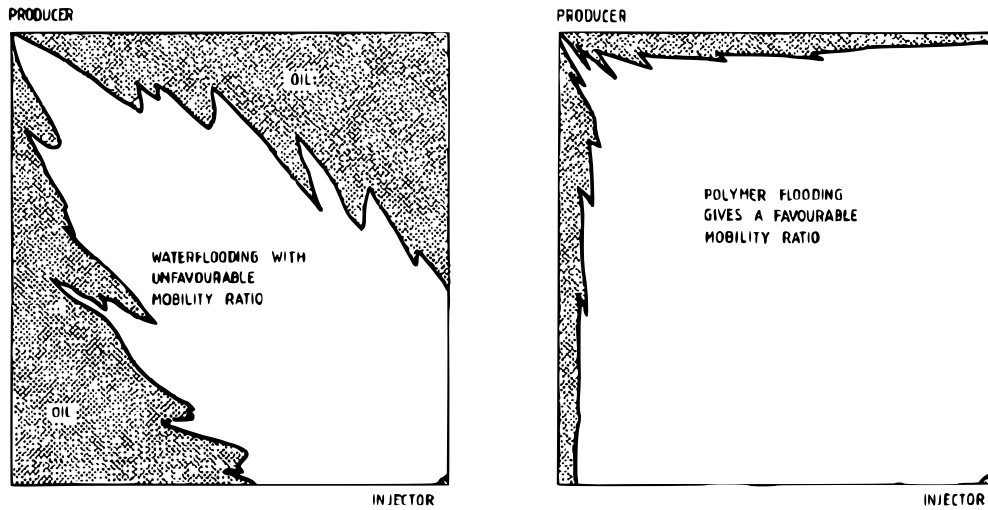


Figure 2.5: Improvement in areal sweep by polymer flooding in a five-spot well pattern Sorbie [14].

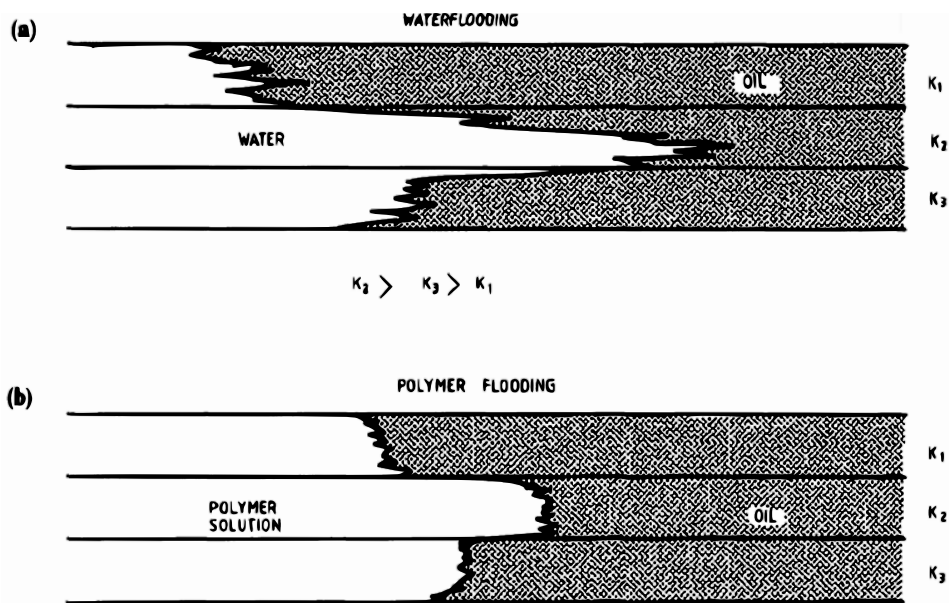


Figure 2.6: Improvement in vertical sweep by polymer flooding in a layered system Sorbie [14].

Traditionally polymer flooding has been considered to mainly accelerate oil production and thereby not affect the residual oil saturation. This idea has been challenged in recent years by a number of studies where polymers have been found to reduce residual oil saturation [20], [21].

This phenomenon has several proposed explanations, such as viscoelastic effects and shear thickening properties [1]. Polymer rheology is introduced in Chapter 5.

3 Properties of Porous Media

In this chapter, fundamental concepts in reservoir physics are presented. Some of the parameters described here are not directly altered in our sensitivity analysis (Chapter 7). Porosity, permeability and capillary pressure are examples of parameters that are indirectly influenced by pore size distribution, pore radii and coordination number (Chapter 4.3).

3.1 Petrophysical quantities

A rock's porosity is a dimensionless parameter defined as the void part of its total volume. For reservoir engineering, the effective porosity is a more meaningful parameter. This means the ratio of the total volume of interconnected voids V_p to the bulk volume of rock V_b :

$$\phi = \frac{V_p}{V_b} \quad 3.1$$

A common misconception about effective porosity is that fluids are guaranteed to flow through the pores because they are interconnected. Porosity is a static parameter, in contrast to permeability, which is the rock's ability to transmit fluid through its interconnected pores. As with porosity, there are different ways to express permeability, depending on the situation.

Absolute permeability is the permeability of a medium with only one phase present. This is a constant parameter for a particular medium, and is independent of the type of fluid. Darcy's law is typically used to describe absolute permeability, K :

$$K = \frac{Q \cdot \mu \cdot L}{\Delta P \cdot A} \quad 3.2$$

Where Q is the flow rate, μ is the viscosity, L is the length of the medium, ΔP is the pressure drop over the medium (absolute value) and A is the cross sectional area of the inlet.

If there is more than one fluid flowing through the pores, one fluid will hinder the flow of the other to some degree. Thereby, an effective permeability for each phase exists, which is dependent on the porous medium and phase saturation.

Finally, relating the effective permeability of each phase to the absolute permeability of the rock has been used to understand multiphase flow in porous media. The concept is called Relative permeability:

$$k_{r,i} = \frac{k_i}{K} \quad 3.3$$

Where $k_{r,i}$ is the relative permeability to phase i (e.g. water, oil or gas), k_i is the effective permeability of phase i , K is the absolute permeability.

Relative permeability of oil and water are usually displayed as a plot where $k_{r,i}$ is plotted as a function of water saturation.

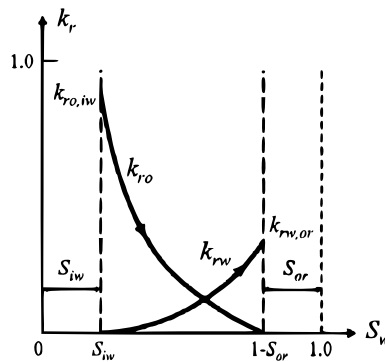


Figure 3.1: Relative permeability curves for imbibition in a water-wet water/oil-system as a function of water saturation. Lien [22].

Figure 3.1 shows typical relative permeability curves for a water-wet system. It clearly shows the saturation dependency of relative permeability seeing as when the relative permeability of one phase is zero (immobile) the other phase has its maximum relative permeability. The end-point relative permeability of oil and water, $k_{r,o,iw}$ and $k_{r,w,or}$, are found at saturations S_{iw} and S_{or} respectively.

3.2 Wettability

The wettability of a solid can be defined as the tendency of one fluid to spread on, or adhere to, a solid's surface in presence of another immiscible fluid [23]. In regards to oilfield operations,

a rock is often characterized as either preferentially water-wet or oil-wet. In reality, these characterizations are extreme simplifications of real porous media. Reservoir rocks are complex structures consisting of a variety of minerals, each with a different wettability. In addition, the saturation history of the rock may influence the wetting preference; a rock previously contacted by oil may be oil-wet.

The wetting preference of a reservoir rock can be quantified by measuring the contact angle between the liquid interface's and the solid's surface. This measurement is known as the wetting angle (θ), and is a reflection of the interfacial tension between the fluids and their adhesive force to the rock's surface. A figurative description of this phenomenon is depicted in Figure 3.2 below:

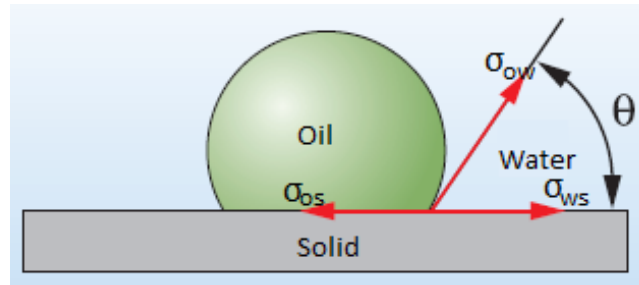


Figure 3.2: Oil drop on a solid surface with surrounding water. σ_{os} , σ_{ow} and σ_{ws} are interfacial tensions between oil-surface, oil-water and water-solid respectively. θ_{ow} is the contact angle between oil and water and in this case indicates a preferentially water-wet surface because $\theta_{ow} < 90^\circ$. Figure modified from W. Abdallah et al. [22]

From the figure, we can derive Young's equation:

$$\sigma_{ow} \cdot \cos\theta_{ow} = \sigma_{os} - \sigma_{sw} \quad 3.4$$

$$\cos\theta_{ow} = \frac{\sigma_{os} - \sigma_{ws}}{\sigma_{ow}} \quad 3.5$$

In the pore network model introduced in chapter 6 of this thesis, all simulations are carried out in a weakly water-wet system $\theta_{ow} = 50^\circ$. The value is kept constant throughout the simulations in order to know that the wetting is equal for every pore, which is important for our sensitivity analysis.

3.3 Capillary Pressure

Two immiscible fluids that are in contact with each other in a pore channel will make a convex meniscus between them. This meniscus will bulge toward the wetting-fluid as it has the stronger adhesive force of the fluids. The capillary pressure can be defined as the molecular pressure difference across the interface of the two fluids [23].

$$P_c = p_{non-wetting} - p_{wetting} \quad 3.6$$

where the non-wetting and wetting fluid in practice is oil and water respectively

$$P_{c,ow} = p_o - p_w \quad 3.7$$

This pressure difference is a result of external and internal electrostatic forces acting on the two fluids. The relationship between the pressure difference and the curvature of the interface is given by the Young-Laplace equation [23]:

$$P_c = \sigma \cdot \left(\frac{1}{R_1} + \frac{1}{R_2} \right) \quad 3.8$$

Where σ is the interfacial tension, R_1 and R_2 are the principal radii of curvature seen in Figure 3.3:

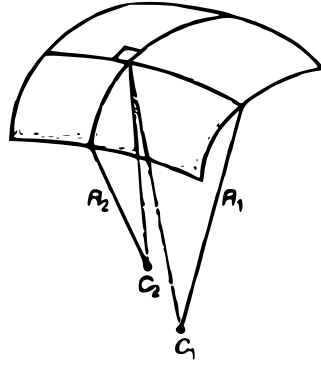


Figure 3.3: The meniscal surface between two immiscible fluids has a curvature with two principal radii, R_1 and R_2 . Figure modified from Lien [22].

If the meniscus is spherical, we have $R_1 = R_2 = R$ and Eq 3.8 becomes

$$P_c = \frac{2 \cdot \sigma}{R} \quad 3.9$$

R can be expressed in terms of pore channel radius r and wetting angle θ as such:

$$R = \frac{r}{\cos\theta} \quad 3.10$$

For a water-oil system with water being the wetting phase and oil the non-wetting fluid we can summarize the capillary pressure with the following pressure:

$$P_{c,ow} = p_o - p_w = \sigma_{ow} \cdot \left(\frac{1}{R_1} + \frac{1}{R_2} \right) = \frac{2 \cdot \sigma_{ow} \cdot \cos\theta_{ow}}{r} \quad 3.11$$

As can be seen from the equation above, capillary pressure is inversely proportional to pore radius. A reservoir rock's capillary pressure is therefore significantly affected by its' pore size distribution and heterogeneity.

3.4 Drainage, Imbibition and hysteresis

Drainage is process where the wetting fluid saturation decreases i.e. when water is displaced by oil in a water-wet reservoir. Imbibition is the opposite process, when the wetting fluid saturation increases, i.e. when oil is displaced by water. These processes are illustrated in Figure 3.4.

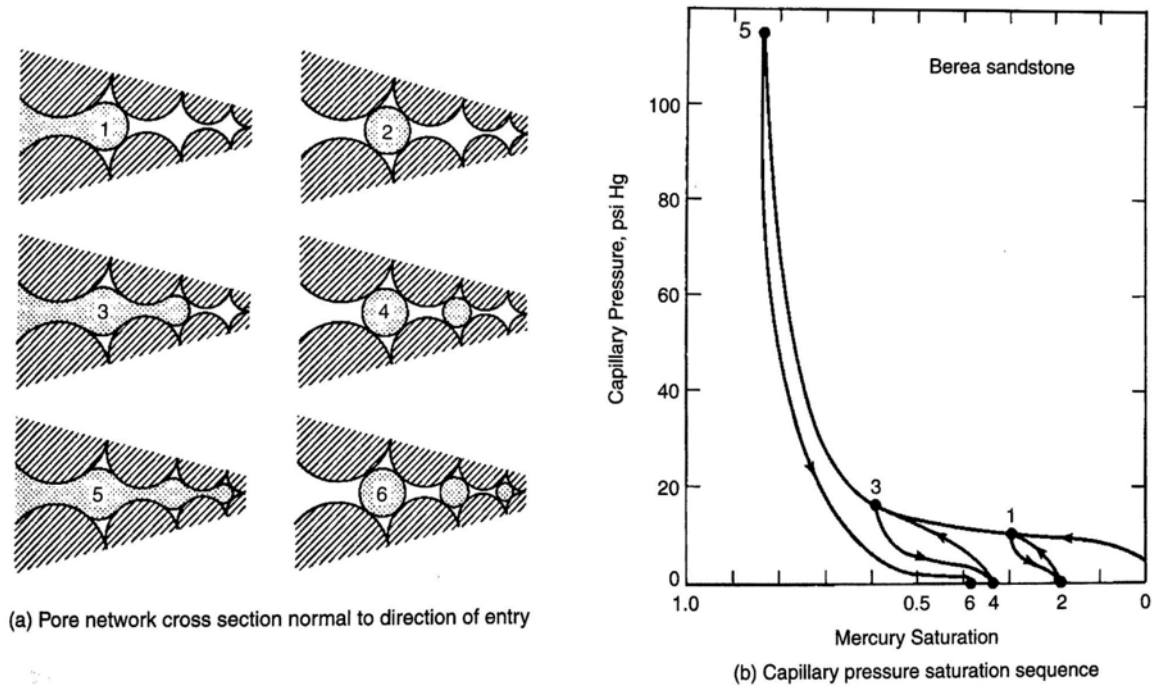


Figure 3.4: The figures shows drainage, imbibition and hysteresis effects as an illustrative cartoon to the left and the corresponding capillary pressure vs non-wetting saturation to the right. The drainage parts are labeled with odd numbers (1,3,5) and imbibition with even numbers (2,4,6). If the capillary pressure is sufficiently increased during drainage to meet condition 1, it can no longer return to the original saturation by imbibition due to snap-off in the pore body (condition 2). The model also shows oil draining into smaller pore bodies (3 and 5) and the respective imbibition conditions after snap-off (4 and 6). The observed saturation hysteresis is a result of snap-off. Lake [13].

For the mercury to start displacing water in the drainage displacement process (1,3,5) a certain capillary threshold pressure has to be overcome. Mercury enters when this equilibrium is disrupted, i.e. when $P_{c,ow} < P_o - P_w$. In condition 1, mercury displaces water by drainage as capillary pressure is increased. If this pressure is released, the wetting fluid (water) spontaneously imbibe into the pore from the right, swelling the water film between the mercury and solid, leaving a mercury globule in the pore by snap-off if conditions are right. If the pressure during drainage is allowed to increase sufficiently, the mercury invades smaller and smaller pores (conditions 3 and 5), leaving more trapped globules by snap-off during an

eventual imbibition process (conditions 4 and 6). The set of curves represented is called a hysteresis loop due to the saturation of mercury being non-reversible after a certain amount of drainage.

In our model, the drainage process is the easiest to model, because it can only occur by piston-like displacement. Imbibition is far more complicated because of the presence of wetting films that enables displacement by snap-off. The important thing here to note is that the capillary pressure for snap-off is lower than for piston-like displacement, roughly half the value. This is attributed to the two radii of the Young-Laplace equation, where one of the radii is infinite at snap-off.

$$P_{c,piston} = \frac{2\sigma}{r} \geq P_{c,snap-off} = \frac{\sigma}{r} \quad 3.12$$

If a pore is filled by oil and the water pressure is increased (imbibition), the capillary entry pressure for piston-like displacement is reached first. Thereby, the significance of Equation 3.12 is that piston-like displacements are preferred to snap-off. How the pore network model used in this thesis deals with this complication is elaborated on in Chapter 6.

4 Pore Network Model Overview

The parameters introduced in chapter 3 can be used to predict fluid flow behavior and oil recovery for a reservoir. They can be obtained experimentally by running tests on cores extracted from reservoir-rock. However, maintaining reservoir conditions for the cores during extraction is challenging and thus the fluid flow may only be representative for specific conditions [12].

It is evident that there is a need for more physically based models in order to predict multiphase flow behavior in porous media. Ideally, the models should be based on fluid flow physics for the displacement process studied (e.g. drainage, water-/polymer imbibition) [12]. To represent fluid flow through porous media the capillary bundle model (see Figure 4.1) has been widely used. This model is simple, but yields an exact analytical theory that in some cases can provide as a check on more complex models [24].

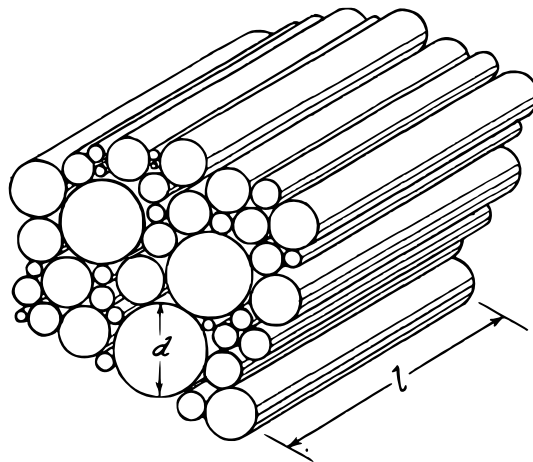


Figure 4.1: Bundle of capillary tubes from Gates and Lietz (1950) [25].

However, this model fails to capture wettability behavior, irregular geometry and branchiness of real porous media [24]. The first pore network model (PNM) simulating two-phase flow was introduced by Fatt in 1956 [26]. He filled pores and throats in a regular 2D-lattice by order of radius according to the Young-Laplace equation. His network model produced capillary

pressure and relative permeability curves that matched experimental data from core floods better than the capillary bundle model.

4.1 Percolation Theory

Percolation was introduced by Broadbent and Hammersley in 1957 [27]. Heiba et al. defined percolation as the generation of a continuous path of connectedness, and thus transport, through a randomly allowed set of bonds and nodes in a network [28]. Percolation theory is based on the static properties of porous media, which does not concern fluid flow. Invasion percolation was later introduced and was seen as an improvement over percolation theory as it included fluid flow. For a drainage process in a water-wet rock, the invading fluid fills a pore bond in order of increasing capillary entry pressure. The fraction of bonds with capillary entry pressures below a given capillary pressure is called the allowed pore segment. However, for these pores to be filled by the injected fluid, they need to be connected to an element already filled with the invading fluid (the invading fluid needs to “see” the pore). The fraction of bonds that also meet this criterion is part of the accessible pore segment.

4.2 Quasi-static Approach

In order to appreciate the advances of the dynamic pore network model used to simulate in this thesis, there is a need to cover its predecessor: the quasi-static MixWet-model of McDougall and Sorbie [29], [30]. The MixWet model is quasi-static model where flow is dominated by capillary forces. The pore-filling sequence will occur according to the order of capillary entry pressures as described in Chapter 4.1 Percolation Theory. The pore elements in this model are cylindrical and has no ability to carry wetting-films. Although the model does not incorporate wetting films explicitly, it does allow for snap-off during water imbibition wherever topology makes it possible.

During Primary Drainage, oil displaces water from a fully water-saturated network. The displacement is driven by successively increasing the capillary pressure until every pore is filled or until some condition e.g. irreducible water saturation, S_{iw} , is met. Invasion occurs in the largest pore accessible (Allowed Pore Segment) that also has a continuous path from the inlet (Accessible Pore Segment). Upon completing the primary drainage process, an aging effect can be applied to the system in the form of changing its wettability. Depending on the choice of wetting parameters, a number of pores change their wettability from water-wet to oil-wet. An

option is also to decide whether the wetting change will correlate to pore sizes or not: (i) Fractional-wet: pore size is not influenced, (ii) Mixed-wet small: smallest pores are oil-wet, or (iii): Mixed-wet large: largest pores are oil-wet.

Following the wettability changes, water is allowed to imbibe along water-wet pathways in the system and snaps off in the smallest oil-filled pores. The displacement process is controlled by successively reducing capillary pressure of the system. Unlike for the primary drainage process, the displacement is now occurring first in the smallest pores e.g. the pores with the highest capillary pressure.

4.3 Properties of Quasi-static models with film behavior

In order to accommodate film behavior in the model, triangular pore geometries were introduced. This will however, influence how petrophysical properties are calculated in the model. Porosity is calculated in the networks by summation of bond volumes, therefore for pores with a triangular cross-sectional area is calculated by:

$$A_t = r^2 \sum_{i=1}^3 \frac{1}{\tan\beta_i} \quad 4.1$$

where r is the inscribed radius, $\beta_1 \geq \beta_2 \geq \beta_3$, $\beta_1 + \beta_2 + \beta_3 = 90^\circ$ are half angles.

In this model, the wetting phase (film) is allowed to adhere mainly in the corners, whereas the non-wetting phase tends to be in the centre of the triangular pore. This two-phase setup within one pore stands out in comparison to the cylindrical pore, which could only carry one phase.

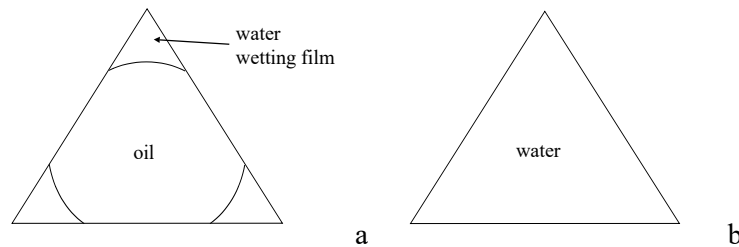


Figure 4.2: Cross section of triangular pore where (a) non-wetting oil occupies bulk of the pore and water resides in corners as wetting film, (b) wetting phase water occupies both bulk and corners of pore. From Sorbie and Dijke [31].

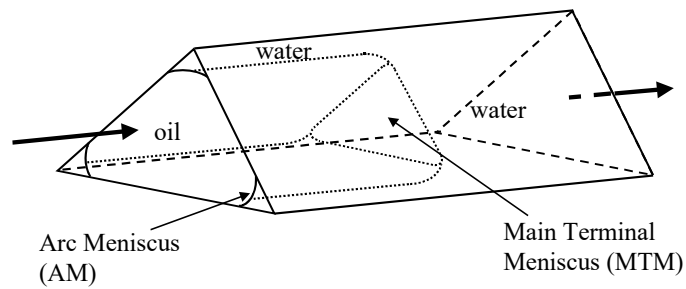


Figure 4.3: Triangular pore element where oil is displacing water (drainage) from the bulk of the pore. From Sorbie and Dijke [31].

Each pore has three corners in which the film can both flow and expand (swell). Pore element saturations are calculated for bulk fluid and corner fluids separately. The volume of corner fluid is decided by the Arc Meniscus (AM) and the pore half angle β (Figure 4.4). The AM with relevant properties can be illustrated as:

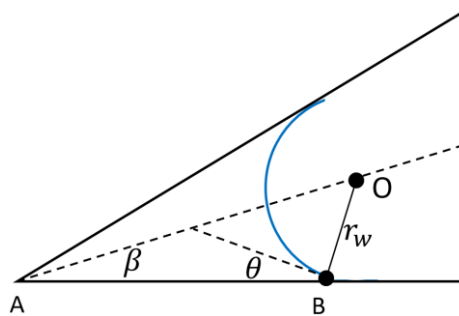


Figure 4.4: Illustration of pore corner, the blue curve represents arc menisci, β and θ are angles. Modified from Li [12].

The distance the AM moves, represented by the distance AB in Figure 4.4 and can be calculated as:

$$AB = r_w \cdot \frac{\cos(\theta + \beta)}{\sin\beta} \quad 4.2$$

An important feature of equation 4.2 is that AB needs to be positive in order to be physically sound, and therefore there exists a critical, θ_{crit} :

$$\theta_{crit} < \frac{\pi}{2} - \beta \quad 4.3$$

If, for one or more of the three corners of the pore, the above condition is not met, the model assumes there to be no wetting fluid in the corner. This means that the following AM configurations can exist within a pore:

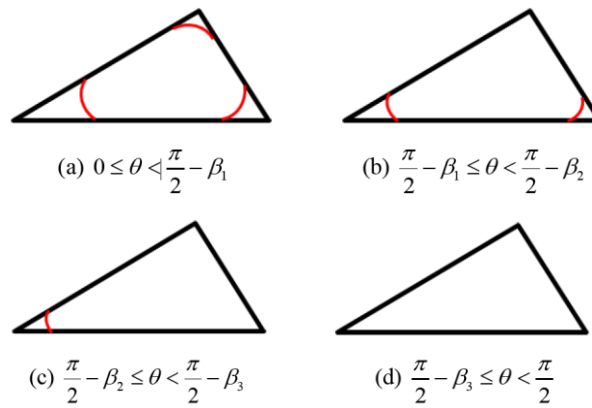


Figure 4.5: Film configuration within a pore. The red curve represents an Arc Meniscus. From Li [12].

When dealing with pore network models, hydraulic conductance is a term used to convey the ease of a fluid to move through a pore spaces (i.e. absolute permeability in petrophysical terms). For a circular pore this is commonly expressed like equation 4.4, assuming Poiseuille flow:

$$g = \frac{\pi r^4}{8\mu l} \quad 4.4$$

Øren et al. (1998) approximated the conductance for non-circular geometries to be [32]:

$$g = \frac{3A^2 G}{5\mu l} = \frac{3r^2 A}{20\mu l} \quad 4.5$$

here G and A are cross-sectional geometry and area, respectively.

Since hydraulic conductance is analogous to absolute permeability (introduced in chapter 3.1), we need a relation suitable for two-phase flow equal to relative permeability. As we know, relative permeability is dependent on phase saturations, and to extend this theory to a pore-scale network we introduce allowed and occupied pore segments.

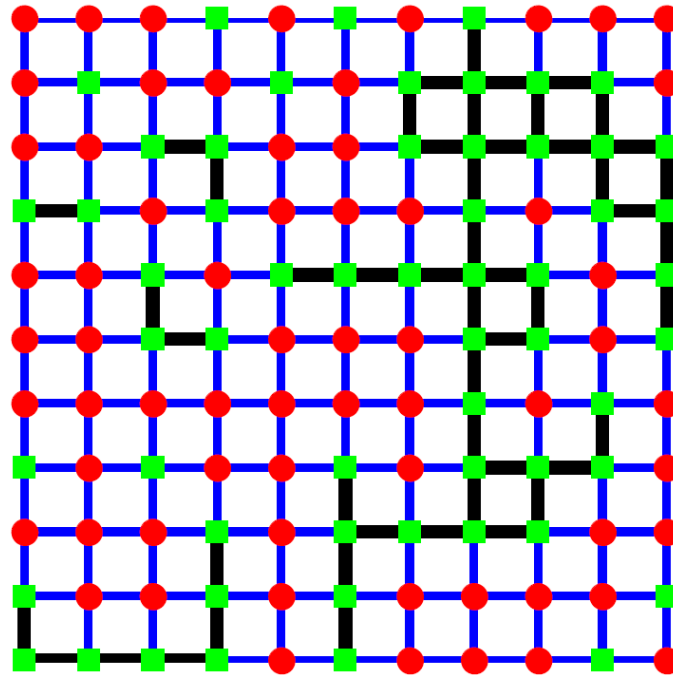


Figure 4.6: Fully connected 2D pore network with inlet at bottom and outlet at top. Node color determines if a pore is allowed to be filled, green is allowed, red is not allowed. Bonds between allowed nodes are black. From Zamani [24].

The allowed pore segment are the bonds in a network that are allowed to be filled by an invading fluid at a given time. Green nodes in Figure 4.6 are examples of pores allowed to be filled. The accessible pore segment however, has to meet an additional requirement. They need to be connected by some continuous path from inlet to outlet.

Only pores that are within the accessible pore segment contribute to the permeability of one phase. Heiba et al. [28] suggested the following equation for one-phase conductance across an entire network:

$$G_j(g) = (1 - f_j)\delta(g) + f_j\rho_j(g) \quad 4.6$$

here, f_j is the fraction of bonds allowed to phase j by the physics of displacement, $\rho_j(g)dg$ is the probability that a bond allowed to phase j has hydraulic conductance between $g + dg$.

Analogous to relative permeability of chapter 3.1, the relative permeability can be expressed as conductances as follows:

$$k_{r,j} = \frac{G_j}{G} \tag{4.7}$$

Parameters such as coordination number (how many bonds a node is connected to) and pore-size distribution are topological parameters that effect the calculation of Equations 4.6 and 4.7. The further derivation process will not be discussed here, an example for a Bethe network can be found in the work of Heiba et al. (1992) [28].

Dynamic models capable of simulating water and/or polymer floods will be covered in Chapter 6. Before that, an introduction to polymers are given in Chapter 5.

5 Polymers

Polymers are chemicals that viscosify water, thereby improving the mobility ratio between water and oil in a way that improve volumetric sweep efficiency by recovering bypassed oil [1]. In recent years, experimental and numerical studies have suggested that polymers may contribute to reducing the residual oil saturation.

Polymer solutions possess the ability to change viscosity depending on the rate that it flows [14]. Polymer molecules are relatively large and the shape of them are affected by stresses put on them. Polymer solutions generally show two characteristics: viscous effects (fluid subjected to shear stress) and elastic effects (fluid subjected to normal stress). HPAM is a synthetic, straight-chain polymer known to undergo both effects. Another polymer, xanthan gum is affected more by viscous effects.

We will not study specific polymers such as HPAM and xanthan further in this thesis. The polymers studied are generic polymers that exhibit either Newtonian, shear thinning, shear thickening or a combination of shear thinning and thickening behavior.

5.1 Rheology

In order to understand how non-Newtonian polymer solutions differ from Newtonian fluids, it is important to know their rheology behavior. Rheology is the study of how fluids flow and deform. The term is often used when describing fluids or materials that show a time-dependency to stress. Below is a figure describing Newtonian shear behavior:

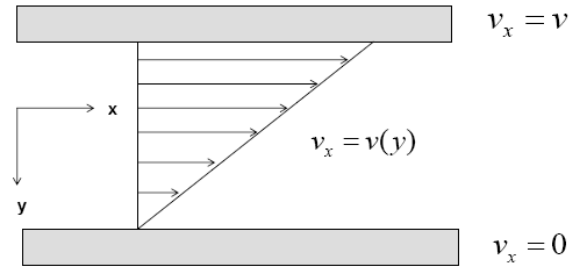


Figure 5.1: Steady-state velocity profile of a fluid between a moving and a stationary plate. The top plate has a velocity v in the x -direction, whereas the bottom plate has zero velocity. The arrows between the plates represent the linearly decreasing drag force (shear stress) that arises between fluid layers in the y -direction. Sorbie [4].

In Figure 5.1, we have two plates closely spaced with large equal areas, A . If a force is applied to the top plate in the x -direction, a shear force is transmitted through the fluid to the bottom plate. Due to the fluid flowing in layers, each layer opposes this applied force and we can see that a velocity gradient can be obtained from top to bottom.

The viscosity of a fluid may be defined as its resistance to shear. The shear stress between two sheets is given by [14]:

$$\tau = \frac{F}{A} \tag{5.1}$$

where τ is the shearing stress, F is the force applied and A the area of the sheet.

Isaac Newton expressed it for straight, parallel and uniform flow:

$$\tau = \mu \cdot \dot{\gamma} \tag{5.2}$$

where μ is the viscosity and $\dot{\gamma}$ is the shear rate

For fluids that show shear dependent viscosity behavior, e.g. polymers, viscosity has to be expressed as a function:

$$\tau = \eta(\dot{\gamma}) \cdot \dot{\gamma} \tag{5.3}$$

These relations state that viscosity is either constant (μ), or may be a function of shear rate $\eta(\dot{\gamma})$. This is illustrated in Figure 5.2:

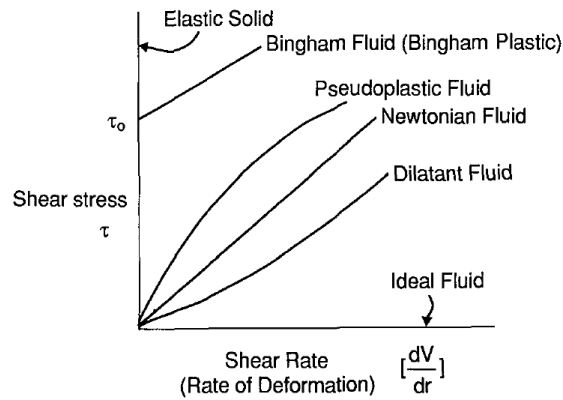


Figure 5.2: Shear behavior for different types of fluids Sorbie [14].

Newtonian behavior is depicted by a constant slope. The pseudoplastic fluid shows a decreasing slope as shear rate increases. This is also known as shear-thinning behavior because it implies that viscosity is reduced with increasing shear rate. Oppositely, the dilatant fluid show shear-thickening behavior as its viscosity is increasing with increased shear rate.

To complicate things further we know that commonly used polymer solutions (e.g. HPAM) are shear thinning at low shear rates, but may exhibit apparent shear thickening behavior above a critical shear rate in porous media. This phenomenon will be further discussed in the following paragraphs, how it is implementation in our model will be introduced later in chapter 6.

5.2 Bulk and In-situ Rheology

When discussing rheology behavior it is important to distinguish between behavior in simple capillary bundle models (bulk viscosity) and behavior in porous media (in-situ viscosity). To obtain bulk viscosity, polymer viscosity is measured in a stepwise manner using a rheometer. The polymer solution is exposed to several shear rates, the viscosity is measured when steady conditions are obtained. Rheometers are used for well-defined flows (e.g. capillary flow), and does not necessarily translate well to the complexity of porous media [14]. Skauge et al (2018) listed four reasons why flow conditions in rheometers and porous media are different [33]:

1. Porous media inherently exhibit complex geometry unlike rheometers.
2. Mechanical degradation may alter rheological properties
3. Polymers that show shear-thinning behavior in rheometers may exhibit apparent shear-thickening behavior above a critical flow rate
4. Polymers show apparent shear-thickening behavior when subjected to varying shear-rates in porous due to its inherent tortuosity and aspect ratio.

Relating in-situ to bulk viscosity has proven to be difficult because most of these models are based on non-Newtonian flow through capillary bundles, which is too simplistic. In Figure 5.3 a schematic comparison between bulk and in-situ viscosity is presented.

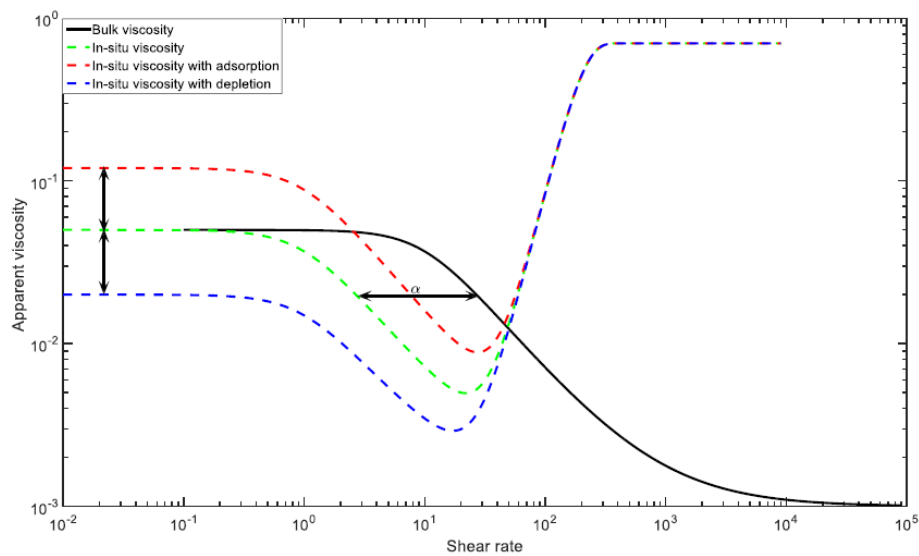


Figure 5.3: Comparison of bulk and in-situ viscosity from Skauge et al. (2018) [33].

Bulk-viscosity show shear thinning behavior and in-situ viscosity show a more complex behavior; a combination of shear thinning and thickening. The horizontal shift (α) between in-situ and bulk viscosity arises because of a conversion factor between in-situ shear rate and Darcy velocity. The red line shows increased apparent viscosity, and thus increased pressure, because polymer adsorption leads to blocking of small pores, which in turn obstructs flow. The blue line represents a decrease in apparent viscosity because of depleted layer effects. Sorbie [14] attributed this effect to polymer molecules not able to rotate freely in close proximity to walls, hence reducing its concentration in this region. This results in a reduction in pressure allowing polymers to flow more easily.

The focus of this thesis is the in-situ rheology, and therefore a segmented diagram of apparent viscosity is included and further described in Figure 5.4.

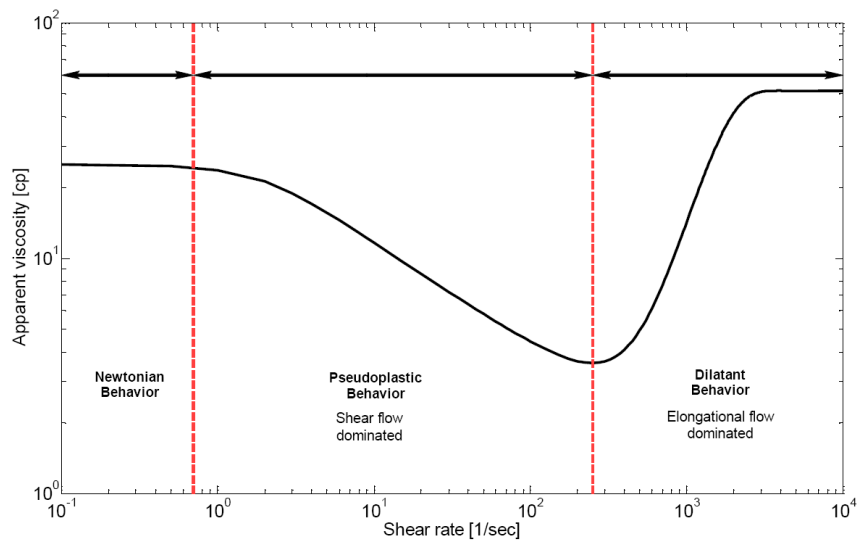


Figure 5.4: Diagram showing apparent in-situ viscosity segmented into Newtonian-, Pseudoplastic- and Dilatant regions, from Skauge et al. (2018) [33].

At low shear rates, the polymer shows Newtonian behavior (viscosity independent on shear rate). At this stage, the polymer viscosity is determined by the hydrodynamic radius of the polymer coils and the concentration of the polymer [34]. Increasing the shear rate beyond a critical shear rate the polymer starts showing non-Newtonian behavior. As can be seen from Figure 13, this part is dominated by shear flow, and is called the pseudoplastic region. The polymers start to stretch in this region and align with the flow resulting in less intermolecular friction and a decrease in viscosity. At some higher shear rate, there are no interactions between the polymer coils and a minimum viscosity is reached. Beyond this point, the polymer solution show elongational dominated flow. The behavior in this region is often referred to as shear-thickening, dilatant behavior or elongation thickening. This behavior is not yet adequately understood, but two popular theories are the transient network model and the coil stretch model [33]. De Gennes (1974) found that when shear rate is increased beyond a critical shear rate the polymer coils unwind abruptly, and viscosity increases [35].

5.3 Polymer Viscoelasticity

When polymer molecules are propagating through porous media it encounters variable pore throat sizes thereby forcing the molecules to decelerate and accelerate. This situation can be imagined by a series of contracting and expanding channels.

Upon entering contractions, the polymer is forced to compress and stretch. If the flow is below a certain critical velocity, the molecules tend to go back to their original configuration [14]. However, if the molecules are not given enough time to go back to their original state in between contractions, stress is accumulated and stored and acts as a “memory effect”. This eventually leads to the polymers resisting flow, increasing the pressure drop and apparent viscosity. Viscoelastic effects such as these are governed by the Deborah number, which helps us predict the onset of extensional viscosity.

$$N_{De} = \frac{\theta_f}{\theta_p} \tag{5.4}$$

where θ_f is the liquid relaxation time and θ_p is the characteristic time for fluid flow (transmit time).

Viscoelastic effects take place if N_{De} exceed a critical value i.e. if the relaxation time θ_f is large compared to the transmit time θ_p . However, several studies have pointed out that this parameter alone is insufficient to predict onset of extensional viscosity. In a numerical study by Zamani et al. (2015), it was suggested that the parameters governing the onset of extensional viscosity could be divided into two categories. These are (i) polymer solution parameters such as molecular weight and concentration and (ii) porous media properties like aspect ratio, inaccessible pore volume and coordination number [36]. Experimental studies by Skauge et al. (2016) reported that extensional viscosity occurred at higher shear rates for radial flow than for traditional core floods [34].

6 Dynamic Pore network Model

In Chapter 4, relevant PNM literature was provided in order to give sufficient background on network modelling. Basic concepts of percolation theory was covered with a subsequent piece regarding the quasi-static MixWet model of McDougall and Sorbie [29]. Now, as this thesis deals with EOR imbibition processes, the following two sections deals with a dynamic imbibition model developed by Li, and a modified code based on the aforementioned model developed by Zamani et al. to include polymer flow.

6.1 Dynamic Imbibition Pore Network Model of Li (2016)

As previously mentioned in Chapter 4, a network model based on the capillary bundle model is unable to carry wetting films. In the model by Li, this is enabled by the use of triangular pores that can carry wetting films in the corners. To accommodate triangular pores the formulae for capillary pressure, pore saturation, pore conductance and pore cross section has to be modified. The basics of this was covered in Chapter 4.3, for more details the reader may refer to the work of Juan Li [12].

Triangular pores enables the coupling of piston-like advancement and film swelling. Which of these mechanisms are dominant is decided by a rate-dependent parameter, λ , relating capillary forces to capillary and viscous forces.

$$\lambda = \frac{\text{capillary force}}{\text{capillary force} + \text{viscous force}} = \frac{P_{c,entry}}{P_{c,entry} + (P_i + P_j)} \quad 6.1$$

where $P_{c,entry}$ is the capillary entry pressure for piston-like displacement in one element and $P_{i,j}$ are the nodal pressures at the water- and oil-filled ends of the pores, respectively. The coupled piston-like/film swelling displacement is illustrated in Figure 6.1.

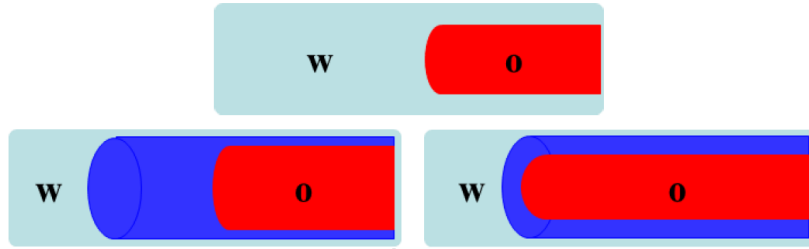


Figure 6.1: Illustrations of partially filled pores where light blue is initial water, dark blue is invading (new) water and red is oil. The situation on top is the initial case, bottom left shows viscous dominant displacement and bottom right shows capillary dominant displacement. Modified from Juan Li [12].

When the flow rate is high, viscous forces dominate and we would see a piston-like displacement as is shown in Figure 6.1 bottom left. The water tends to stay in the center of the pore and push the oil in a piston-like manner, hardly affecting film swelling. Oppositely, at low flow rates, capillary forces will dominate and the water will tend to swell the water film, as is the case in Figure 6.1 bottom right.

Due to the nature of equation 6.1 it is evident that when $\lambda = 1$, only capillary forces exist leading to snap-off displacement. Conversely, if $\lambda = 0$, only viscous forces exist thus giving piston-like displacement. A combination of these displacement occur for intermediary values of λ .

For the triangular pores in this model, four different cross-sectional configurations of water can exist due to film swelling and snap-off as in Figure 6.2.

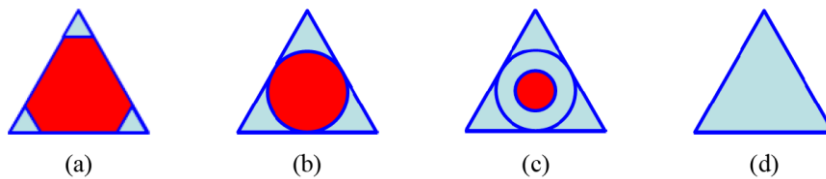


Figure 6.2: Cross-sectional fluid configurations allowed in the triangular pores. (a) is the state after drainage. (b-d) shows the water/oil configuration in stages for imbibition. Blue is water and red is oil [12].

Initially water exists as a thin stable lens occupying the corners of the pore (a). Water is allowed to swell from the corners if the oil is not trapped (b). From here, the next sequence is either (c)

or (d). The piston-like displacement in (d) is allowed to occur if upstream adjacent bulk water is available *and* the nodal pressure from water to oil filled pores is greater than the capillary entry pressure $(P_i + P_j) > P_{c,entry} \Rightarrow \lambda$ is closer to 0 than 1. The situation in (c) describes the intermediate stage between piston-like and snap-off displacement.

Bond conductance can be calculated once the fluid configurations inside the pores are known. Mass conservation for the volumless nodes in this model implies that

$$\sum q_{i,j} = 0 \quad 6.2$$

Here i and j still represents oil or water filled pores respectively.

Flow rate for pores without bulk menisci is calculated by:

$$q = g \cdot (P_i - P_j) \quad 6.3$$

Where q, i and j is consistent with the previous formulae, g is the bond conductivity.

Flow rate for pores with bulk menisci has to include capillary entry pressure thus:

$$q = g \cdot (P_i - P_j + P_c) \quad 6.4$$

Equations 6.3 and 6.4 form a set of linear equations that can be solved using mass conservation. The pressure- and flow field can then be updated.

This model presumes water to be injected at a fixed flow rate. To maintain a constant injection rate throughout the displacement processes, adjustments to the global pressure drop, ΔP , are needed. If we at first ignore capillary pressure, the global pressure (ΔP) and injection rate (Q) can be related by

$$Q = \alpha \cdot \Delta P \quad 6.5$$

where α is a constant parameter depending on fluid configuration and pore conductance.

Including capillary pressure Equation 6.5 simply becomes:

$$Q = \alpha \cdot (\Delta P + \bar{P}_{c,entry}) = \alpha \cdot \Delta P + b \quad 6.5$$

here $\bar{P}_{c,entry}$ is the systems average capillary pressure, $\alpha \cdot \Delta P$ is Darcy's law and b is the capillary pressure between the fluids.

In order to keep a constant injection rate, Q_{inj} , a iterative process called Aker's method [37] is used to obtain a target injection rate, Q_{target} , that is in satisfactory agreement with the predefined injection rate Q_{inj} .

Following the calculation procedure described above, the minimum time steps are calculated using bond flow rates. A minimum time step is chosen so that for each step no more than one pore is filled completely.

6.2 Modified Model including Polymer flow

The following modifications to the dynamic imbibition model are further elaborated on in the paper by Zamani et al. (2019) [1].

As mentioned previously, a key study for this thesis is the flow of non-Newtonian and Newtonian fluids through porous media. Fluids are assumed to display one of the following types of flow in the model:

(1) Newtonian	Polymer viscosity dependent on polymer concentration but independent on shear rate.
(2) Shear thinning	Polymer viscosity decreases with increased shear rate.
(3) Shear Thickening	Polymer viscosity increases with increased shear rate.
(4) Complex	Polymer viscosity show two or more of the behaviors listed in (1), (2) and (3).

A model that related apparent viscosity by a shear dominant and an elongational dominant part was proposed by Delshad et al. [38].

$$\mu = \mu_{sh} + \mu_{el} \quad 6.6$$

Polymers that show shear-thinning behavior is usually described by the Carreau model proposed by Canella et al. in 1988 [39]:

$$\mu_{sh} - \mu_{\infty} = (\mu_p^0 - \mu_{\infty}) [1 + (\lambda_p \cdot \dot{\gamma})^{\alpha}]^{(n-1)/\alpha} \quad 6.7$$

For the apparent shear-thickening regime, μ_{el} , Delshad (Delshad *et al*., 2008) proposed the following model:

$$\mu_{el} = \mu_{max} \cdot [1 - \exp(-(\lambda_2 \cdot \dot{\gamma} \cdot \tau_r)^{n_2-1})] \quad 6.8$$

Combining equations 6.6, 6.7 and 6.8, Delshad found an expression incorporating all the fluid viscosity behaviors we would like to investigate:

$$\mu = \mu_{\infty} + (\mu_p^0 - \mu_{\infty}) \cdot [1 + (\lambda_p \cdot \dot{\gamma})^{\alpha}]^{(n-1)/\alpha} + \mu_{max} \cdot [1 - \exp(-(\lambda_2 \cdot \dot{\gamma} \cdot \tau_r)^{n_2-1})] \quad 6.9$$

If we assume the constants are $\alpha = 2$ and $\lambda_2 = 1$ then we are left with the model used in this thesis:

$$\mu = \mu_{\infty} + (\mu_p^0 - \mu_{\infty}) \cdot [1 + (\lambda_p \cdot \dot{\gamma})^2]^{(n-1)/2} + \mu_{max} \cdot [1 - \exp(-(\dot{\gamma} \cdot \tau_r)^{n_2-1})] \quad 6.10$$

where μ_{∞} and μ_p^0 are the high and low Newtonian shear rate plateaus respectively. μ_{max} is the maximum polymer viscosity at high shear rates for a polymer with shear-thickening properties. λ_p and τ_r determine the onset of shear-thinning and shear-thickening behaviors, whereas n and n_2 governs the slopes of shear-thinning and shear-thickening parts.

To include rheology models in the imbibition model, there is a need to describe polymer concentration locally in the network. A “transport” equation is thereby suggested in the work of Zamani et al. where the concentration, C , is a dimensionless fraction ($0 \leq C \leq 1$, where $C =$

1 at injection). Polymers are assumed able to flow through bulk water and waterfilms and its concentration through the network follows mass-conservation laws. To visualize the calculation process we can look at flow through a node connected to four bonds.

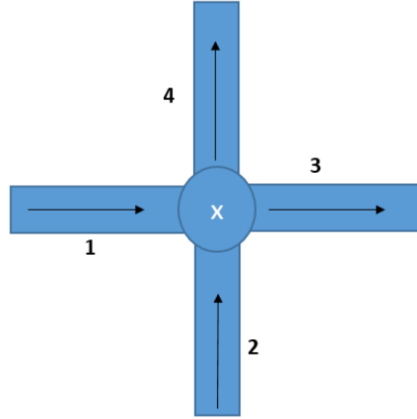


Figure 6.3: Schematic showing flow in (1 & 2) and flow out (3 & 4) of a node connected to four neighboring nodes. From Zamani et al. [1].

For each time-step, the following procedure is carried out:

Mass flowing in for every node

$$M_{in} = Q_1 \cdot C_1 + Q_2 \cdot C_2$$

Rate of flow out for every node

$$Q_{out} = Q_3 + Q_4$$

Updated concentration

$$C_i^t = \frac{S_w^{t-1}}{S_w^t} \cdot C_3^{t-1} + \left(\frac{Q_i}{Q_{out}} \cdot M_{in} - Q_3 \cdot C_3^{t-1} \right) \cdot \left(\frac{\Delta t}{S_w^t \cdot V_p} \right)$$

After the calculations above are done, polymer viscosity, local velocity, bond conductivity and node pressures are updated. For each iteration, local velocities may change because of fluctuating inlet pressure. Other iteration processes are followed depending on the fluid being Newtonian or Non-Newtonian to ensure a satisfactory accuracy to the calculated local pressures, see Figure 6.4.

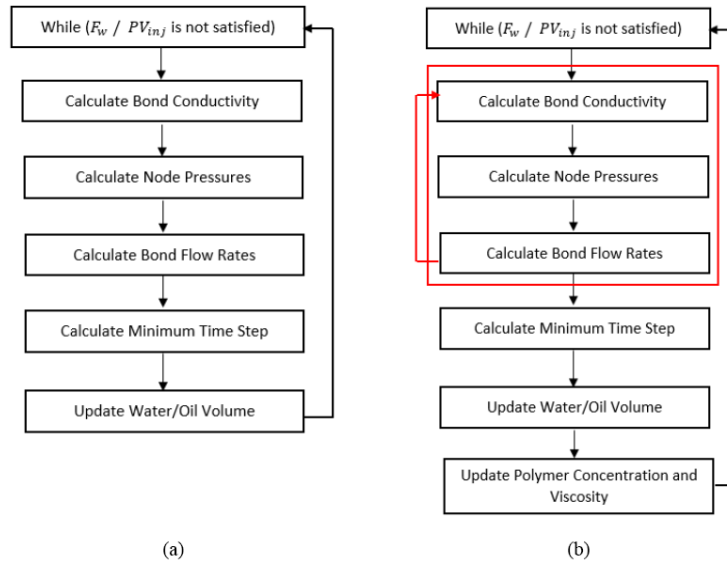


Figure 6.4: Simulator flow chart for (a) water imbibition and (b) polymer injection. In both cases the stopping criteria is either pore volume injected PV_{inj} or fraction of water at outlet F_w . From Zamani et al. [1].

Some of the calculations in the imbibition model is partly or fully omitted from this thesis as the mathematics are not the primary focus here. The curious reader can find additional information about:

- How the local shear rate ($\dot{\gamma}$ in equation 6.10) can be related linearly to local velocity ($\dot{\gamma} = \alpha v$) (Zamani et al. 2017 [40]).
- How local bond stretch rate is calculated when fluids are deformed through contraction-expansion channels using the Navier-Stokes approach (Zamani et al. 2015 [36]).
- The importance of eddies in relation to contraction expansion channels (Zamani et al. [1])

6.3 Previous work using the dynamic pore network model

In addition to modifying the imbibition model to include polymer flow (chapter 6.2), the researchers involved in the paper also did a sensitivity study to evaluate the effect of polymer rheology on oil displacement in a pore network.

The network used was a two-dimensional, weakly water-wet model. They studied the performance of different polymer rheology behaviors across oil-water viscosity ratios

$(\mu_o/\mu_w) = 1, 10 \text{ and } 100$. Water and polymer injections were carried out as secondary injections only, and stopped when 1PV of fluid had been injected.

As a key part of the paper was to evaluate the performance of polymer rheology on oil displacement, the polymer properties (See Equation 6.10) were chosen so that for a constant injection rate of $Q = 10^{-8} m^3/s$ they showed the same apparent viscosity $\bar{\mu}_p = 5.44 cP$. This allows us to evaluate the rheology models from the same “starting point”. The apparent viscosity is found by applying various injection rates over the network model in a single-phase flooding. Pressure drops for polymer (ΔP_p) and water (ΔP_w) are measured and used to calculate apparent in-situ viscosity by $\mu_{app} = \frac{\Delta P_p}{\Delta P_w} \times \mu_w$. The different rheology curves and their crossing point (at $Q = 10^{-8} m^3/s$ and $\bar{\mu}_p = 5.44 cP$) are shown in Figure 6.5.

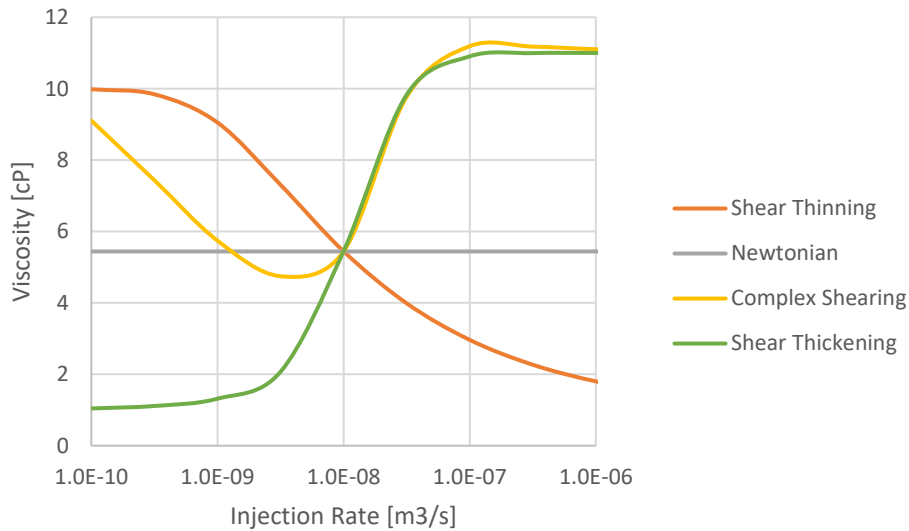


Figure 6.5: In-situ rheology for the four cases investigated. From Zamani et al. [1].

Despite the apparent viscosity being the same at a given injection rate, the polymer solutions show different viscosities when travelling through the pore network.

The key conclusions from the work can be summarized as:

1. Two-phase oil recovery using polymer were consistently more effective than waterflooding for all cases. More surprisingly however, was the varying degrees of effectiveness that different rheologies had on oil recovery. The balance between

viscous and capillary forces affect microscopic diversion. This was thought to be the reason for the observed differences.

2. The polymer showing shear thinning and thickening behavior was found to be most efficient, while the pure shear thickening polymer showed least efficient behavior. A plausible explanation for this was found when analyzing differential pressure as a function of pore volumes injected. The most effective polymer consistently had the higher pressure up until breakthrough, however the authors stressed that this may be case dependent behavior.
3. The most efficient polymer suppressed snap-off events most efficiently thus leading to more piston-like displacements.
4. Polymers can improve pore scale sweep efficiency if the balance between viscous and capillary forces can be increased in favor of viscous forces. Oil recovery depends on rheological behavior thus there might be an optimal rheology for oil recovery efficiency.

7 Results and discussion

In this chapter, the results from the sensitivity analysis carried out in this thesis is presented. An attempt is made to reproduce the results of Zamani et al. for a viscosity ratio (VR) of 100, we call this $M=100$, not to be confused with Mobility Ratio (M^*). This will serve as our base case off which subsequent alterations to our set-up will be compared. We then extend this to more adverse viscosity ratios of $M=1000$ and $M=10000$ and see if some of the findings presented in Chapter 6.3 hold here as well. Water viscosity is kept constant (1 cP) throughout this thesis, meaning only oil viscosity is changed. Later on, changes to polymer concentration, coordination number, aspect ratio and grid size (2D & 3D) are investigated.

The network model studied in this thesis is identical to the one investigated by Zamani et al. It is a 2D model consisting of volumeless nodes interconnected by bonds in a distorted fashion. The model is assigned a number of nodes in x-, y- and z-direction which in this case is fully connected (i.e. the coordination number $z=4$ for a 2D network).

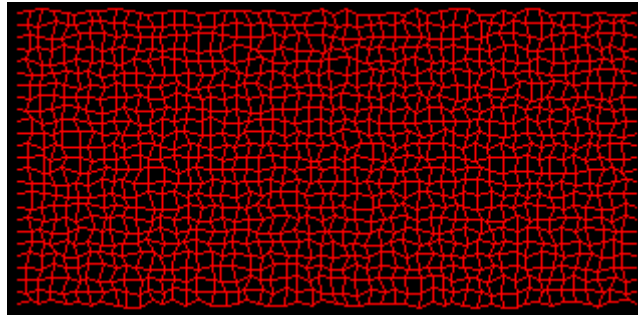


Figure 7.1: Distorted 2D (50 x 25 x 1) network model used in this thesis.

The simulations are carried out in a weakly water-wet system ($\theta_{ow} = 50^\circ$) with a truncated normal distribution with radii $0.1 \leq r \leq 30$ (μm).

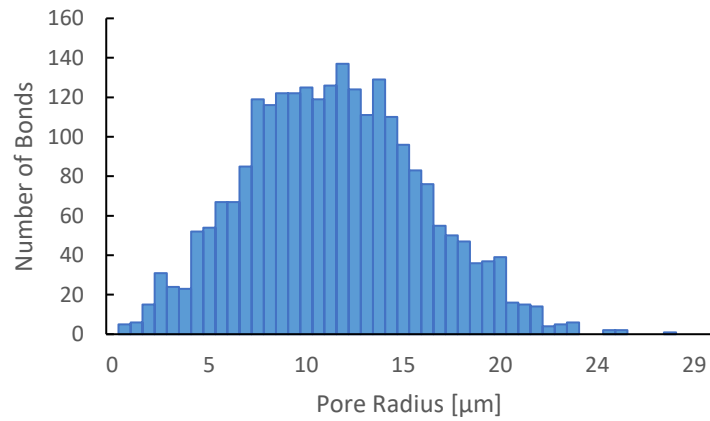


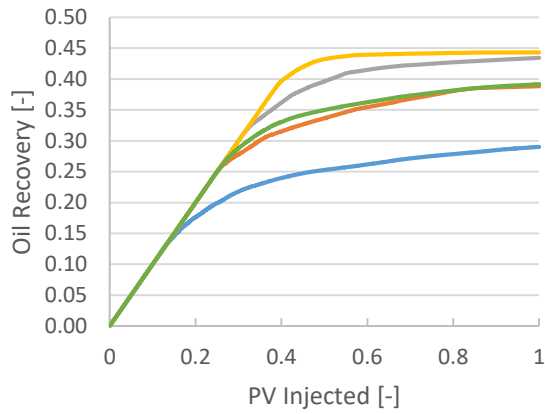
Figure 7.2: Pore size distribution (PSD) used for the Base Case. Reproduced from Zamani et al. [1].

Basic properties of the network as mentioned above and others are summarized in the table below.

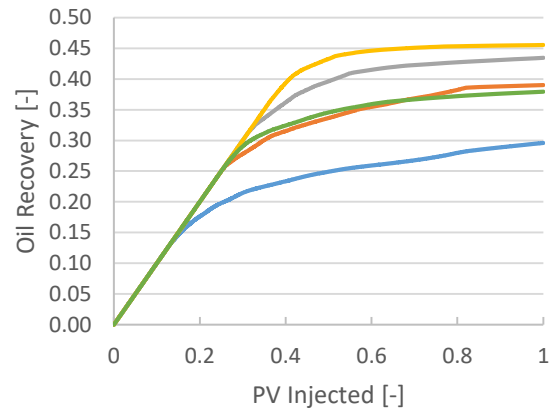
Table 1: Basic network properties used in the simulation of the base case.

Parameter	Value	Unit
<i>Network Size</i>	50 x 25 x 1	x, y, z (direction)
<i>Coordination Number</i>	4	[-]
<i>Pore Size Distribution</i>	Truncated normal around 10	[-]
<i>Bond Radius</i>	[0.1,30]	μm
<i>Distortion factor</i>	0.3	[-]
<i>Average Pore Length</i>	333	μm
<i>Pore half angles</i>	30, 30, 30	Degree
<i>Wettability</i>	Water wet	[-]
<i>Water/Oil Contact Angle</i>	50	Degree
<i>Interfacial Tension</i>	40	mN/m
<i>Injection Rate</i>	10^{-8}	$m^3 s^{-1}$
<i>Capillary Number</i>	5.4×10^{-4}	[-]
<i>Viscosity Ratio</i>	100	[-]

To confirm that the correct network and polymer parameters were used in this work an attempt was made to reproduce the simulation results of Zamani et al. for $M=100$.



(a) Original result



(b) Reproduced result

— Water — Shear Thinning — Newtonian — Complex Shearing — Shear Thickening

Figure 7.3: Graphs show oil recovery vs. pore volume injected. (a) is the result obtained by Zamani et al. [1]. (b) is the reproduced result from this thesis.

The oil recoveries of Figure 7.3 show a good match, with only slight differences between them. The simulator randomly chooses which of the 25 bonds at the inlet (y-axis) to first inject (See Figure 7.1). This is thought to be the cause of the minor differences observed between the original and reproduced result.

7.1 Secondary Injection at Adverse Viscosity Ratios (M)

In the following we investigate how simulations are affected by extending to more unfavorable viscosity ratios ($M=100$, $M=1000$, $M=10000$). The main goal is to see if some of the observations made by Zamani et al. still hold.

In Figure 7.4, fluid distributions are presented after 1 PV of injected fluid. Waterfloods and polymer floods are applied as secondary injections to a pore network fully saturated by oil after drainage.

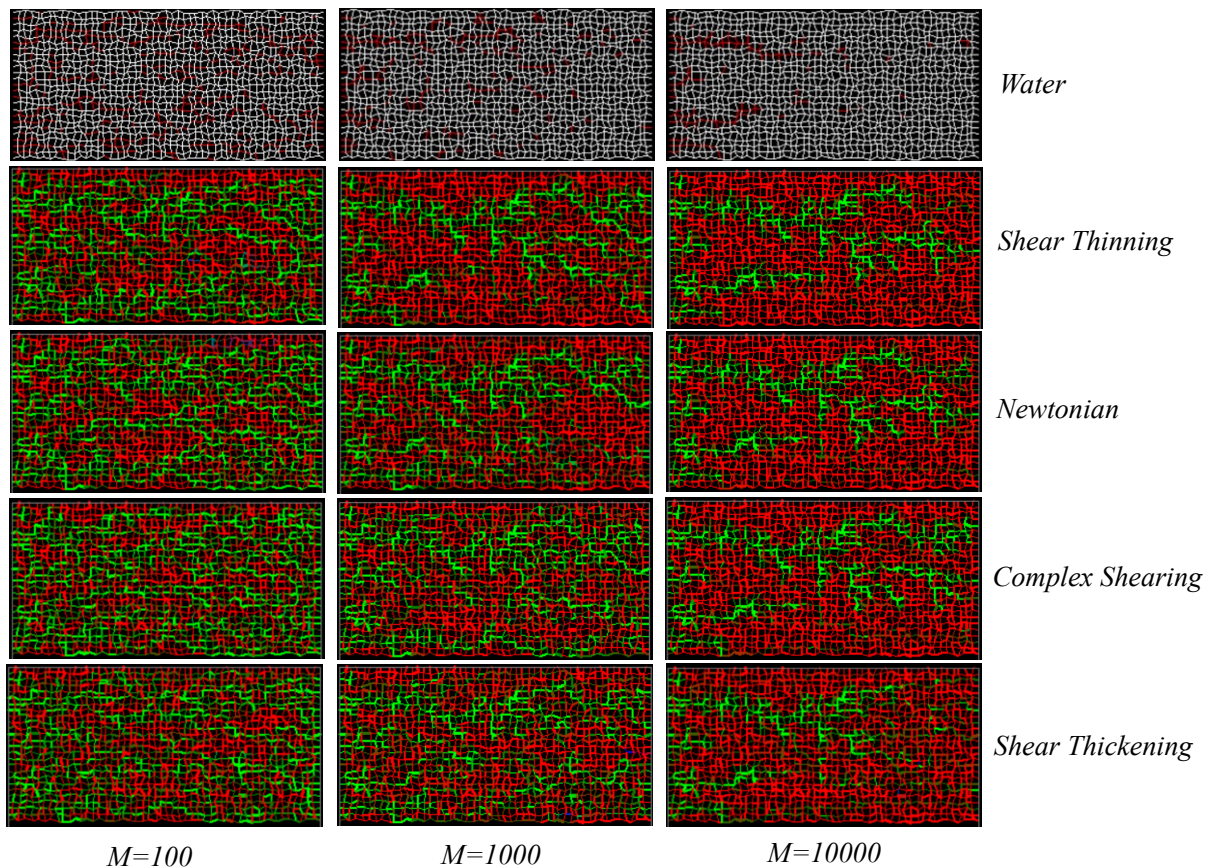


Figure 7.4: Fluid distributions after injecting 1 PV of water/polymer. For the water case, red is water and white is oil. For the polymer cases, red is oil and green is polymer.

It is clear that less oil is swept in all cases when the viscosity ratio is increased. Remember, an increased viscosity ratio implies a higher adverse mobility ratio. For the water injections, we see bonds filled by water (red) that seemingly are disconnected from the flow, and the reader may wonder if water has reached the outlet. The reason for this is water flowing in films, and

furthermore is not represented in the model unless a bond is fully saturated by water. This means that drawing comparisons between water and polymer injections based on these snapshots alone can be misleading. They are, however, useful when visualizing the effect of increased viscous fingering and snap-off between the viscosity ratios. In the case of $M=100$ it is clear that the complex shearing has the least oil (red) zones left behind, especially in the middle part of the model. This feature is still noticeable for $M=1000$ and $M=10000$, but at a lesser degree. No general trend is observed that apply when comparing the remaining rheology behaviors.

It is important to note that the snapshots only reveal which areas the polymers have swept and may not be a good measurement of how much oil has been recovered. The snapshots fail to show that bond radii vary between 0.1 and $30\mu\text{m}$, thus affecting how much oil it can hold. This is the case for $M=1000$ (Figure 7.4), where the shear thickening and Newtonian polymers seem to clearly out-perform the shear thinning polymer. Differences are present but less evident when looking at endpoint oil recovery for this viscosity ratio (b) in Figure 7.5.

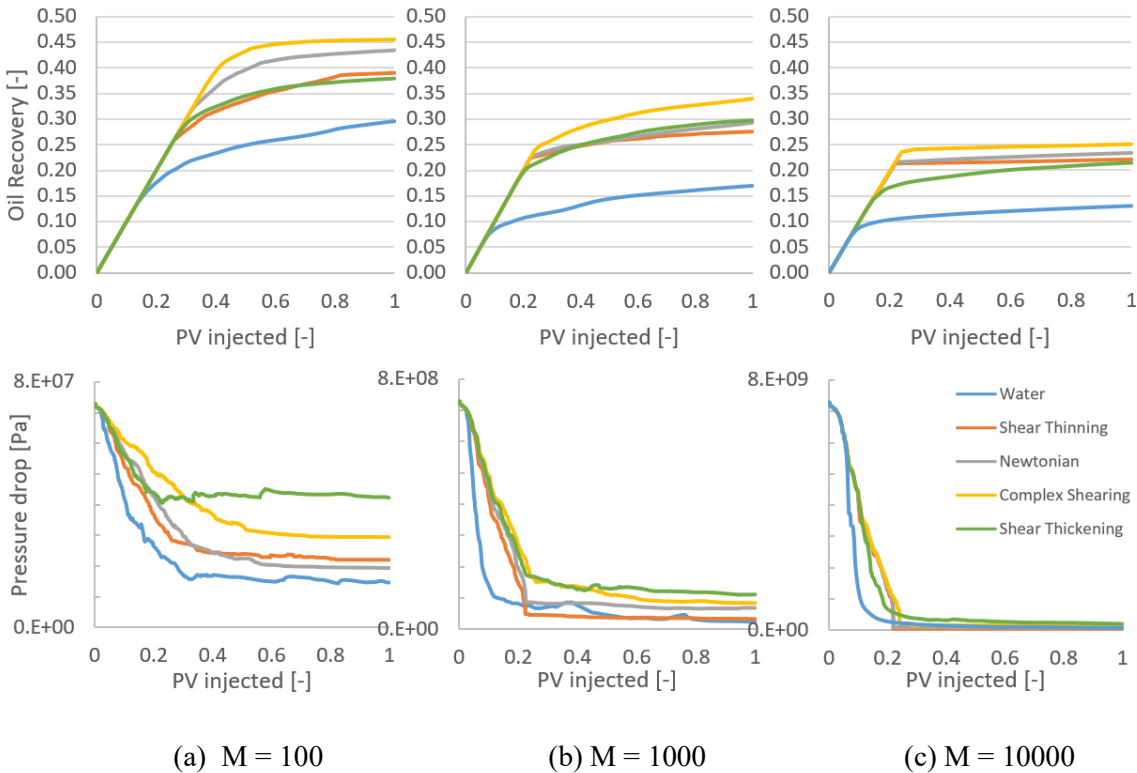


Figure 7.5: Oil recovery (top) and differential pressure (bottom) against pore volume injected for the various rheology models and viscosity ratios (M).

From the oil recoveries in Figure 7.5, it is clear that all polymers yield an increase in oil recovery. This is not surprising, but the substantial differences that exist between the rheologies

are. The apparent viscosity for all the polymers were confirmed to be the same ($\bar{\mu}_p = 5.44cP$) at the fixed injection rate ($Q_{inj} = 1 * 10^{-8}m^3/s$), see Figure 6.5. The complex shearing polymer shows the highest oil recovery across the viscosity ratios (a, b, c). The polymer cases produce significantly more oil than water; however, the differences between the polymers seem to decrease with higher adverse viscosity ratio. The Newtonian flow show second best or tied second best recoveries over the various viscosity ratios. The pure shear thinning and pure shear thickening cases produce the least oil for $M=100$ and $M=10000$, but for $M=1000$ shear thickening seems to produce similarly to Newtonian polymer, leaving the pure shear thinning to produce the least oil.

It has been suggested that the viscous pressure drops (ΔP) vs PV_{inj} may reveal information about what rheology model is most effective [1]. Zamani et al. observed that ΔP up until water breakthrough could determine the oil recovery of rheology models. Looking at the pressure curves in Figure 7.5 reveals that the complex shearing has the highest ΔP up to roughly breakthrough, hence producing the most oil. This means that this rheology model increases the viscous forces the most when most of the oil is produced (up to BT). The pressure curves for $M=1000$ and $M=10000$ show the lowest ΔP for pure shear thinning and pure shear thickening respectively. They both end up producing the least amount of oil of the rheology models.

The complex rheology model had the highest oil recovery, and it was the most dominant relatively to the other polymers at $M=100$. To investigate this further, viscosity and velocity distributions for all rheologies at $M=100$ are included in Figure 7.6.

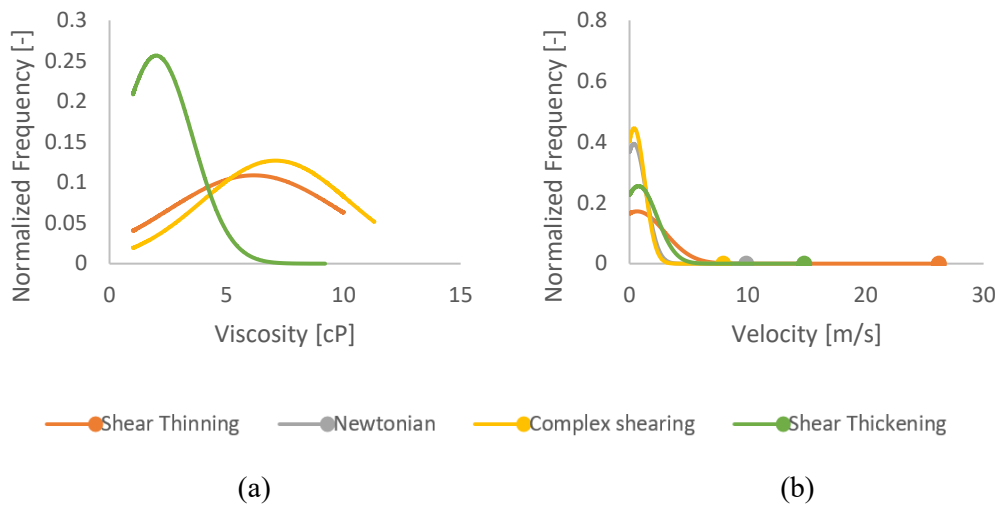


Figure 7.6: Normalized frequency of bonds at (a) a given viscosity or (b) a given velocity at the end of simulation for $M=100$.

Figure 7.6 shows that despite the discrepancy in oil recovery for complex shearing and shear thinning, they show a similar viscosity distribution. It is however evident from the velocity distribution that the complex shearing rheology has a substantially higher number of low-velocity bonds. For an imbibition case such as this, low-velocity occur in bonds of larger volume. It is therefore clear that the complex rheology has an advantage, being able to displace large bonds with a high polymer viscosity.

Another feature of the oil recovery showed that shear thinning and shear thickening performed similarly. The velocity distribution reveals that the shear thickening rheology flows more high-volume (low velocity) bonds than the shear thinning rheology. The shear thickening rheology will however, have a lower viscosity at lower velocities and displace oil less efficiently here. This relationship showcases the importance different rheology behavior can have when flowing through porous media.

Pore-scale displacements can be further analyzed by looking at water/oil occupancy at various stages through the secondary displacements. Figure 7.7 shows the pore size distribution of the network color coded to show number of bonds that are oil filled. Each of the bar diagrams have three layers, with the light blue being the backmost one, the light blue the middle and the yellow the front. After primary drainage (PD), the network is fully saturated by oil hence the top of the light blue bar represents the oil-filled bonds after PD. The peaks of dark blue represents the oil-

filled bonds after breakthrough of water (BT). The yellow bars represent oil-filled bonds after the simulation is finished (1 PV injected).

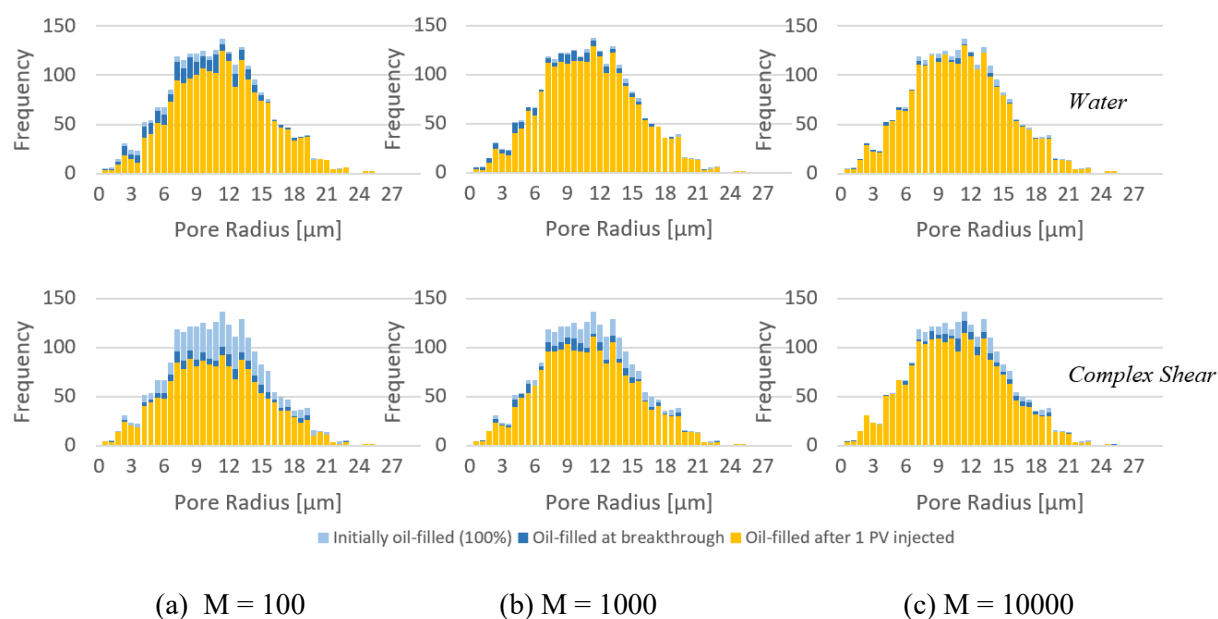


Figure 7.7: Oil occupancy in bonds across the pore size distribution for water and complex shearing. The light blue column shows how many bonds are displaced until breakthrough. The dark blue column shows the amount of displaced bonds from breakthrough. The yellow columns show how many bonds are left oil filled across the pore size distribution after 1 PV injected.

The oil occupancy graphs show that the complex shearing model produces most of its oil before breakthrough and produces oil from a wide set of pore radii. Water produces most oil from small pores, and much of the production is after water breakthrough. Generally, the polymers displace oil from medium sized pores most frequently. A trend can be seen as the viscosity ratio is increased, namely that all the polymers displace less oil from smaller radii, and larger pores are not as affected.

The oil occupancy distributions of Figure 7.7 for $M=100$ show clearly that water displaces most of its bonds after BT, whereas the complex polymer displaces mostly prior to BT. This disparity is less clear and obvious when the other rheology models are included. To make comparisons between rheology models, the accumulated fraction of bonds that have been water filled are presented in Figure 7.8.

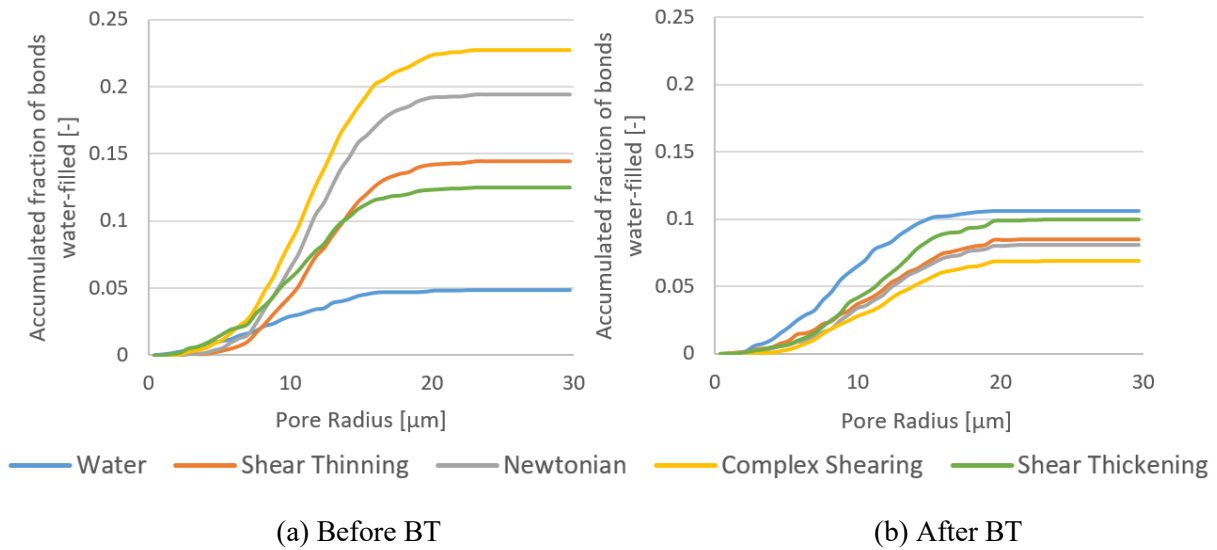


Figure 7.8: M=100: Accumulated fraction of bonds that have been filled with water (i.e. oil produced from pore) (a) prior to BT and (b) post BT.

From these plots, it is clear that all polymers displace more bonds prior to BT than after. They also reveal that the ordering of which model displaces more bonds is reversed after BT (b).

The simulations above were re-run for 2.5 pore volumes injected to see if the oil production curves converge (see Appendix A.1). For M=100 and M=10000 the curves largely flatten out or increase only very slightly. For M=1000 the Newtonian polymer nearly catches up with the complex polymer from 1 to 2.5 PV injected, the other rheology models flatten out.

7.2 Increasing polymer concentration

Increasing the polymer concentration of a solution leads to a consequent increase in viscosity. By increasing the polymer viscosity μ_p by a factor of ten for the case $M=1000$ (i.e. $\mu_o = 1000cP$ and $\mu_w = 1cP$) would make the polymer viscosity ten times more viscous. A comparison to the base case, $M=100$ would therefore be interesting.

Recall from chapter 6.2 the polymer viscosity equation used by the simulator:

$$\mu = \underbrace{\mu_{\infty} + (\mu_p^0 - \mu_{\infty}) \left[1 + (\lambda_p \dot{\gamma})^2 \right]^{(n-1)/2}}_{\text{Shear thinning}} + \underbrace{\mu_{max} [1 - \exp(-(\dot{\gamma} \tau_r)^{n_2-1})]}_{\text{Shear thickening}}$$

As indicated by the equation, only the first part is used for the shear-thinning rheology, however for both the shear thickening and complex rheology the full equation is used. In Figure 7.9, the increase in viscosity is visualized for a range of shear rates.

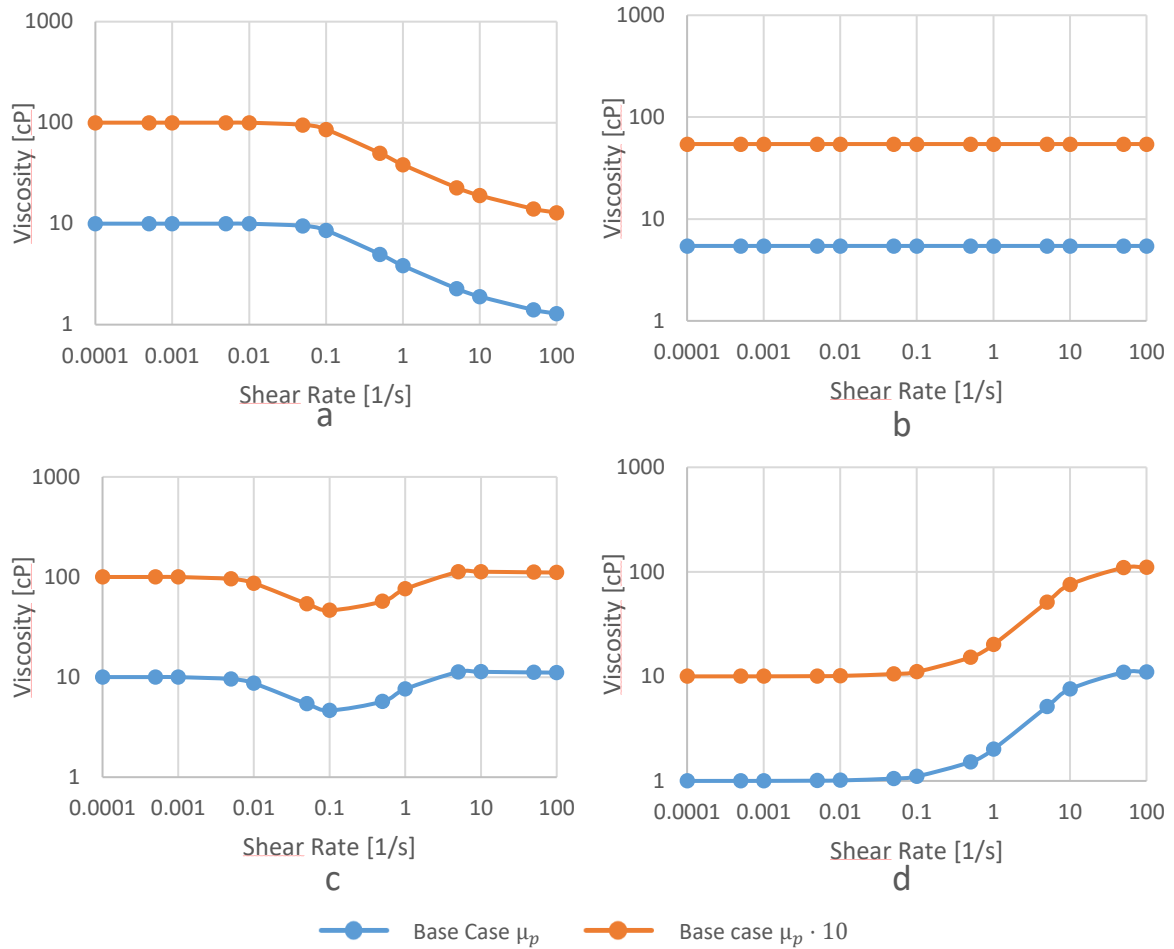
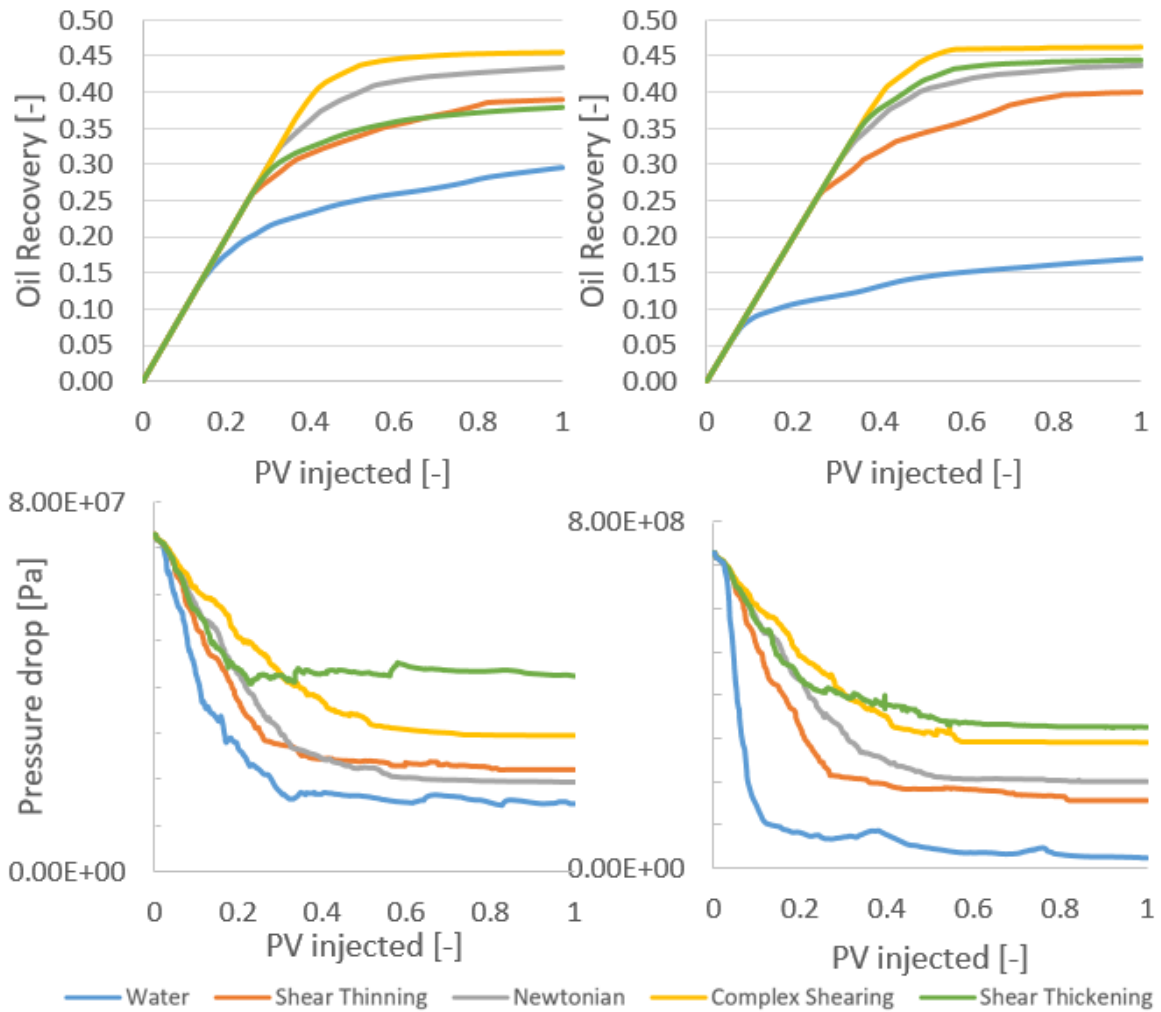


Figure 7.9: Viscosity vs. shear rate for (blue): Base case μ and (orange): Base case $\mu \cdot 10$. Rheology models (a) shear thinning (b) Newtonian, (c) complex shearing and (d) shear thickening.

The graphs verify that viscosity is increased by a factor of ten across the whole range of shear rates. Simulations for $M=1000$ with polymer viscosities increased by a factor of ten should intuitively be similar to the result obtained in the base case $M=100$.



(a) $M = 100$, base case μ_p

(b) $M = 1000$, $\mu_p \cdot 10$

Figure 7.10: Oil recovery (top) and differential pressure (bottom) vs. PV injected across various rheology behaviors.

The oil recoveries for shear thinning, Newtonian and the complex rheology models show very similar behavior in both simulations of Figure 7.10. The shear thickening model shows significant improvement in oil recovery. It is not immediately evident from the differential pressure that the shear thickening rheology would receive such an increase in oil recovery. It is however, clear that the shear thickening rheology maintains a slightly larger gap down to the shear thinning pressure during the early parts of the displacement. To find out why the shear thickening model performs so well, the viscosity and velocity distributions are presented in Figure 7.11.

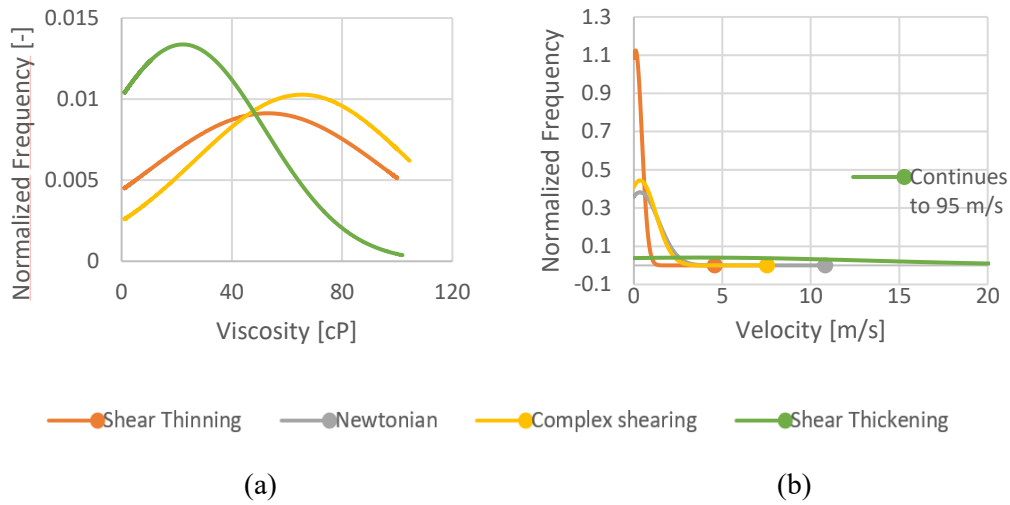


Figure 7.11: Normalized frequency of bonds at (a) a given viscosity or (b) a given velocity at the end of simulation for $M=1000$ with $\mu_p \cdot 10$.

The distributions shown in Figure 7.11 shows clearly that the shear thickening rheology model has a much wider velocity distribution than what it showed for $M=100$ in Figure 7.6. The nature of the shear thickening rheology makes it more viscous at higher shear velocities. Comparing the viscosity distribution to the one in Figure 7.6, the shear thickening rheology clearly has more width, and does not decrease as sharply in frequency towards higher viscosities.

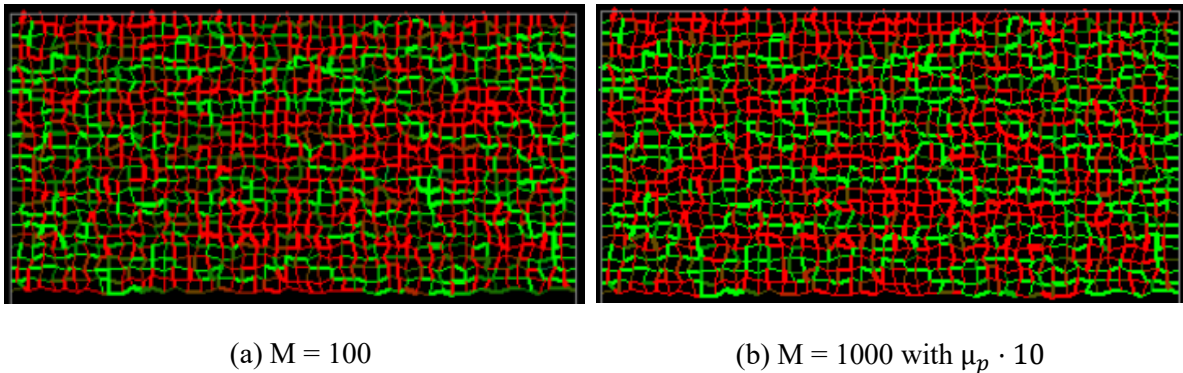


Figure 7.12: Fluid distributions for shear thickening rheology after 1 PV injected for the shear thickening rheology model.

The fluids distributions of Figure 7.12 show that there are definite differences in where the models have swept. $M=1000$ has swept more of the right hand part (outlet) and has clearly swept more in the lower middle part of the model. $M=100$ looks to sweep slightly more bonds

in the left hand side (inlet) of the model. As mentioned previously, these figures do not capture pore radii and thus the volume displaced, so we need a pore occupancy model, Figure 7.13.

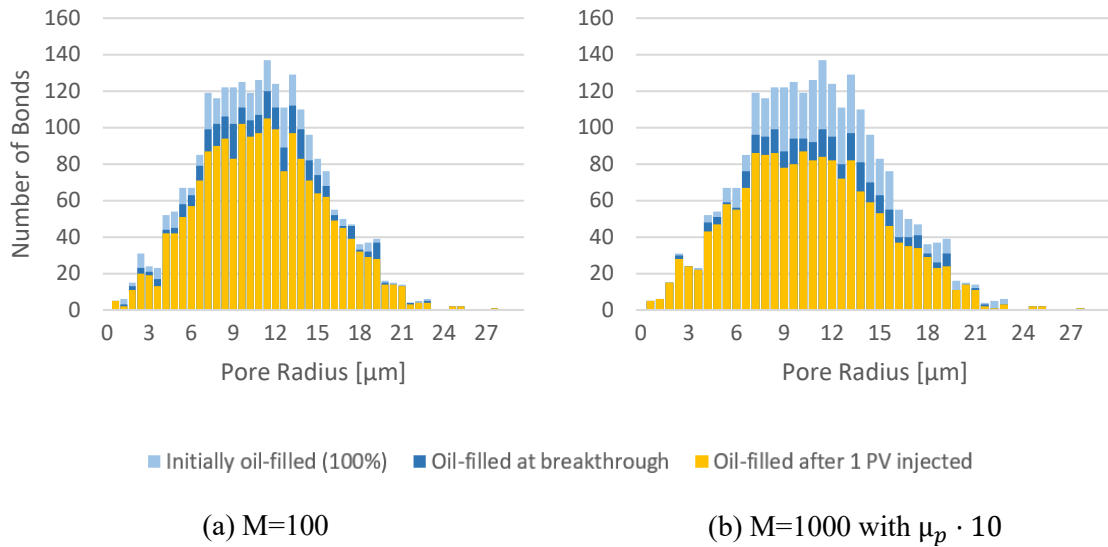


Figure 7.13: Number of oil-filled bonds as a function of pore radius for the shear thickening rheology model.

From figure 7.13 it is immediately obvious that $M=1000$ has swept much more of the medium and larger sized pores compared to $M=100$. $M=1000$ also sweeps relatively more bonds up till breakthrough, but seems to sweep similar numbers of bonds after breakthrough. A consequence to $M=1000$ sweeping larger bonds is that it does not touch the smallest bonds, which could influence conductivity in less connected models.

The shear thickening rheology model sees an increase in oil recovery and a wider viscosity distribution. This is in agreement with experimental (Chauveteau (1981) [41]) and numerical (Zamani et al. (2015) [36]) studies. They reported that an increase in polymer concentration may reduce the critical velocity, leading to an earlier onset of extensional viscosity.

7.3 Reducing coordination number

In this part, the coordination number, z , is decreased from 4 (fully coordinated in 2D) to 3.5. This is of course an average value, as every node has to be connected by an integer amount of bonds (1 to 4). The effect this has on the network model is illustrated in Figure 7.14.

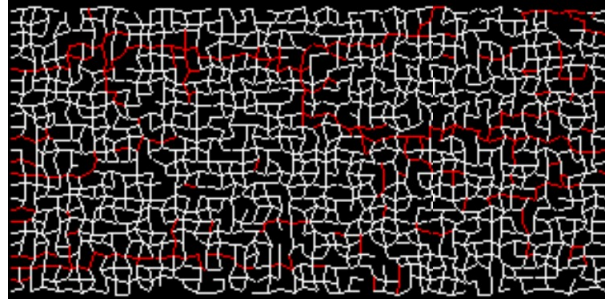


Figure 7.14: Fluid distribution after waterflooding the network model with $z=3.5$. White is oil, red is water.

By reducing the average coordination number, bonds are removed from the model at random. This affects the pressure drop over the model, thus affecting the apparent viscosity of our rheological models. The aim of this sensitivity study is to evaluate the polymers at the same apparent viscosity and injection rate. Adjustments are made to the polymer properties so that the rheology models cross $\bar{\mu}_p = 5.44 \text{ cP}$ and $Q = 1 \times 10^{-8} \text{ m}^3/\text{s}$. The parameters that are tuned governs the onset of shear thinning and shear thickening behavior, λ_p and τ_r of equation 6.10.

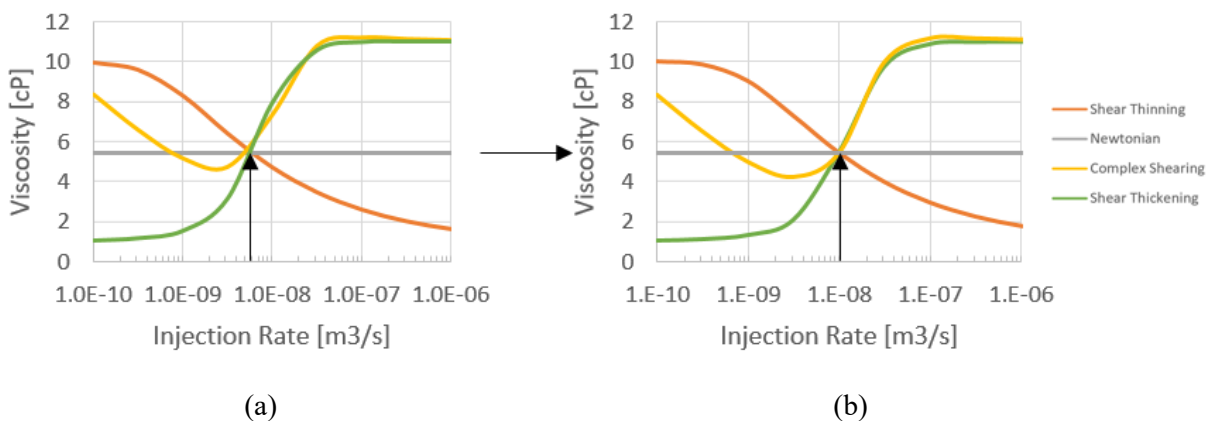
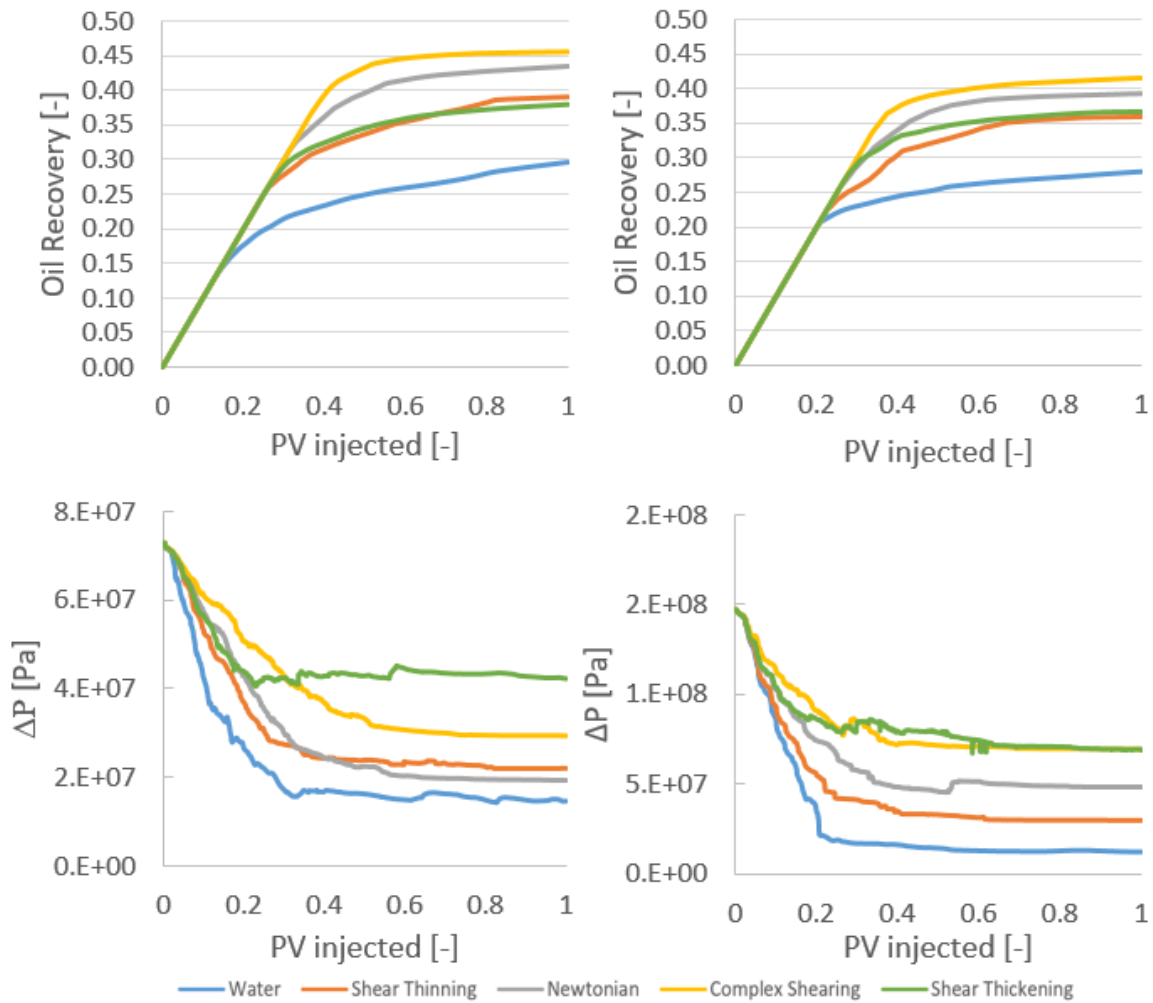


Figure 7.15: Polymer properties are modified so that the four rheology models are evaluated at the same apparent viscosity for an injection rate of $Q = 10^{-8} \text{ m}^3/\text{s}$.



(a) $M = 100, z = 4$

(b) $M = 100, z = 3.5$

Figure 7.16: Oil recovery and differential pressure vs PV injected for the fully coordinated base case (a) and the simulation with a reduced coordination number $z=3.5$ (b).

The end-point oil recovery is reduced for all rheology models as expected by reducing the coordination number. The reduction in coordination number, and thus the bond accessibility, also results in a higher differential pressure across the model. The differential pressure vs. PV injected reveal that once again the complex shearing and water maintains the highest and lowest differential pressure over the main period of oil production (before BT). This agrees well with previous observations made regarding the determination of end-point oil recovery from pressure plots.

The pressure plots for the Newtonian and shear thickening rheology models are less distinguishable in the early parts of the simulation (0-0.2 PV injected). Despite this, the shear

thickening rheology model ends up with less oil produced. This may be because the shear thickening model sees a reduction in viscosity as the pressure is reduced, making the mobility ratio less favorable. The Newtonian model maintains its viscosity and is able to displace more bonds effectively. The same argument can be used to explain why the shear thinning model catches up with the shear thickening model. When the pressure drops, the shear thinning model has its viscosity increased, making the mobility ratio more favorable.

An interesting result of reducing coordination number is the additional effect it has on breakthrough and tail production. The most prominent examples in this case is the waterflood, which has its BT “postponed”, opposite to the complex rheology, which sees an earlier BT. This is more clearly visualized by the pore occupancy plots in Fig 7.17.

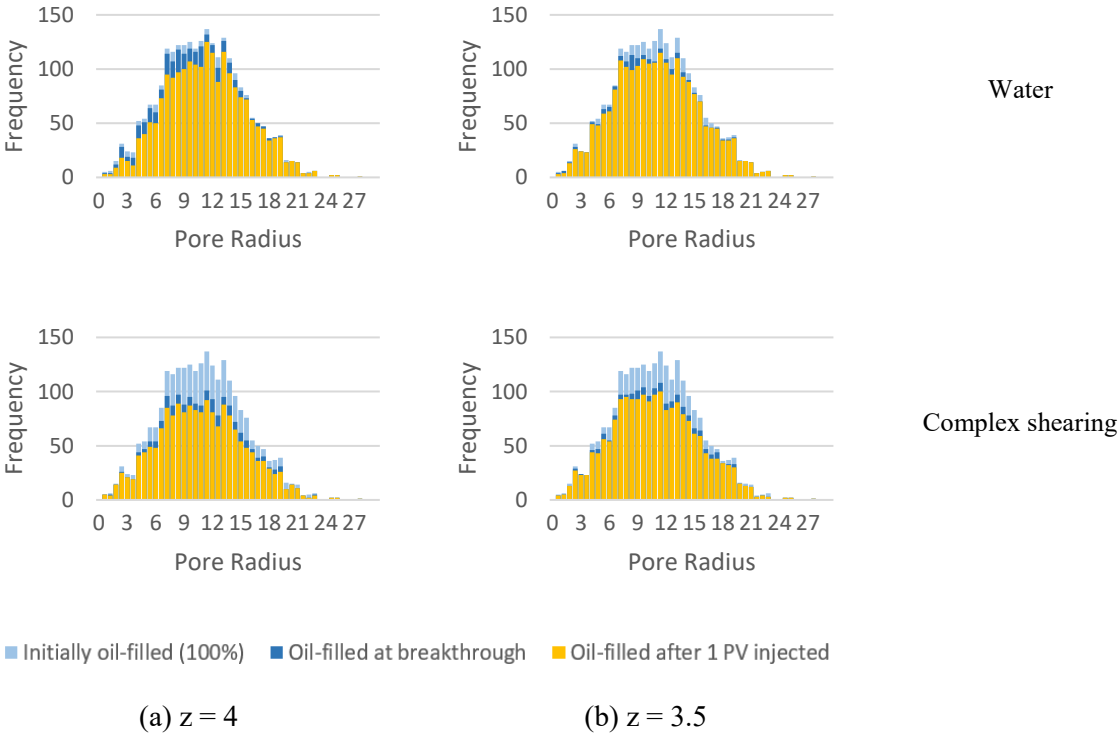


Figure 7.17: Number of oil-filled bonds as a function of pore radius for the waterflood and complex shearing rheology.

The waterflood clearly displaces more oil before breakthrough (light blue bar), but the oil production after BT is markedly reduced. Most of the displacement is centered on medium sized pores, leaving the smaller pores unswept. The complex rheology model sweeps less bonds both before and after BT, but it is most noticeable prior to BT. The reduction in sweep seems to not

be centered on a specific bond size, but rather reduces the sweep across all pore sizes in this case.

7.4 Altering Pore Size Distribution

Earlier studies have confirmed that by increasing the aspect ratio, onset of extensional viscosity is triggered at lower velocities. An in-direct way of changing the aspect ratio of the network model is to use different pore size distributions (PSD). The base case has a truncated normal distribution with a mean radius $\bar{r} = 10 \mu m$ and a standard deviation of $\sigma = 5 \mu m$. In this chapter, additional simulations are run for b) a truncated normal distribution with a mean radius $\bar{r} = 20 \mu m$ and c) a uniform PSD (see Figure 7.18).

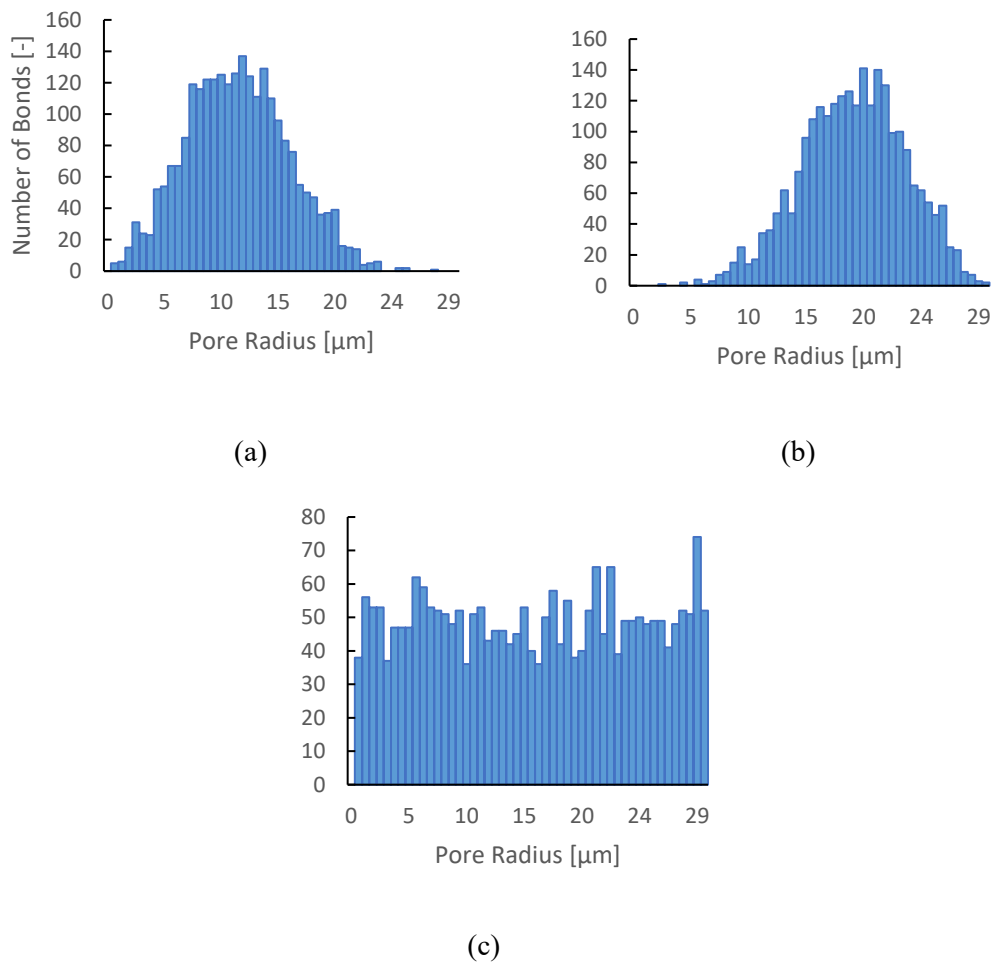


Figure 7.18: Pore Size Distributions for: (a) “Base Case” PSD (b) “Large pores” PSD (c) “Uniform” PSD

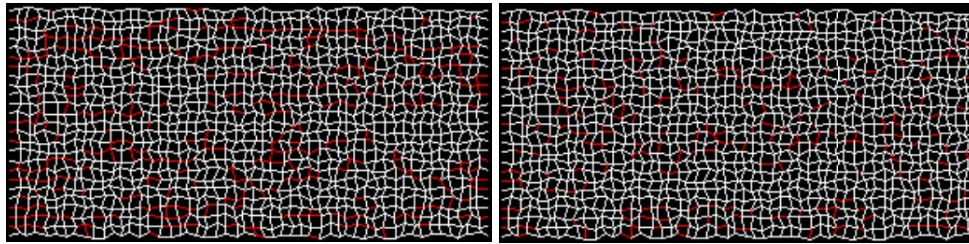
Table 2: Parameters used to alter the PSD for the various cases simulated.

PSD parameters		Base Case	Large pores	Uniform
Exponents	<i>PSD</i>	10	10	0
	<i>Volume</i>	2	2	2
	<i>Conductivity</i>	4	4	4
Radii [μm]	<i>Rmin</i>	0.1	0.1	0.1
	<i>Rmax</i>	30	30	30
	<i>Rmean</i>	10	20	10
	<i>Standard deviation</i>	5	5	5

Whenever the properties that involve the pore network is altered (such as altering PSD), the pressure drop for polymer and water over the network will be different. The parameters governing the onset of shear thinning and shear thickening has to be adjusted accordingly so that at the set injection rate, the rheology behaviors show the same apparent viscosity.

7.4.1 “Large Pores” Pore Size Distribution

In this model, the average pore size is larger than before, thus we can expect lower flow velocities and differential pressures. Generally, the polymer floods have shown to sweep middle-sized pores the most. In this case, there will be fewer of these “middle-sized” pores, and more of the larger, less swept pores. Based on this we expect the oil recovery to be lower for these simulations.



(a) “Base case” PSD

(b) “Large pore” PSD

Figure 7.19: Fluid distributions for (a) the base case PSD, (b) the “large pore” PSD. White is oil, red is water.

From Figure 7.19, it is clear that fewer bonds have been fully swept by water, probably meaning that more of the flow has transpired through wetting films. While these illustrations are useful to determine where the water has swept the network, it says little about the amount of oil recovered. The production and pressure profiles are presented in Figure 7.20.

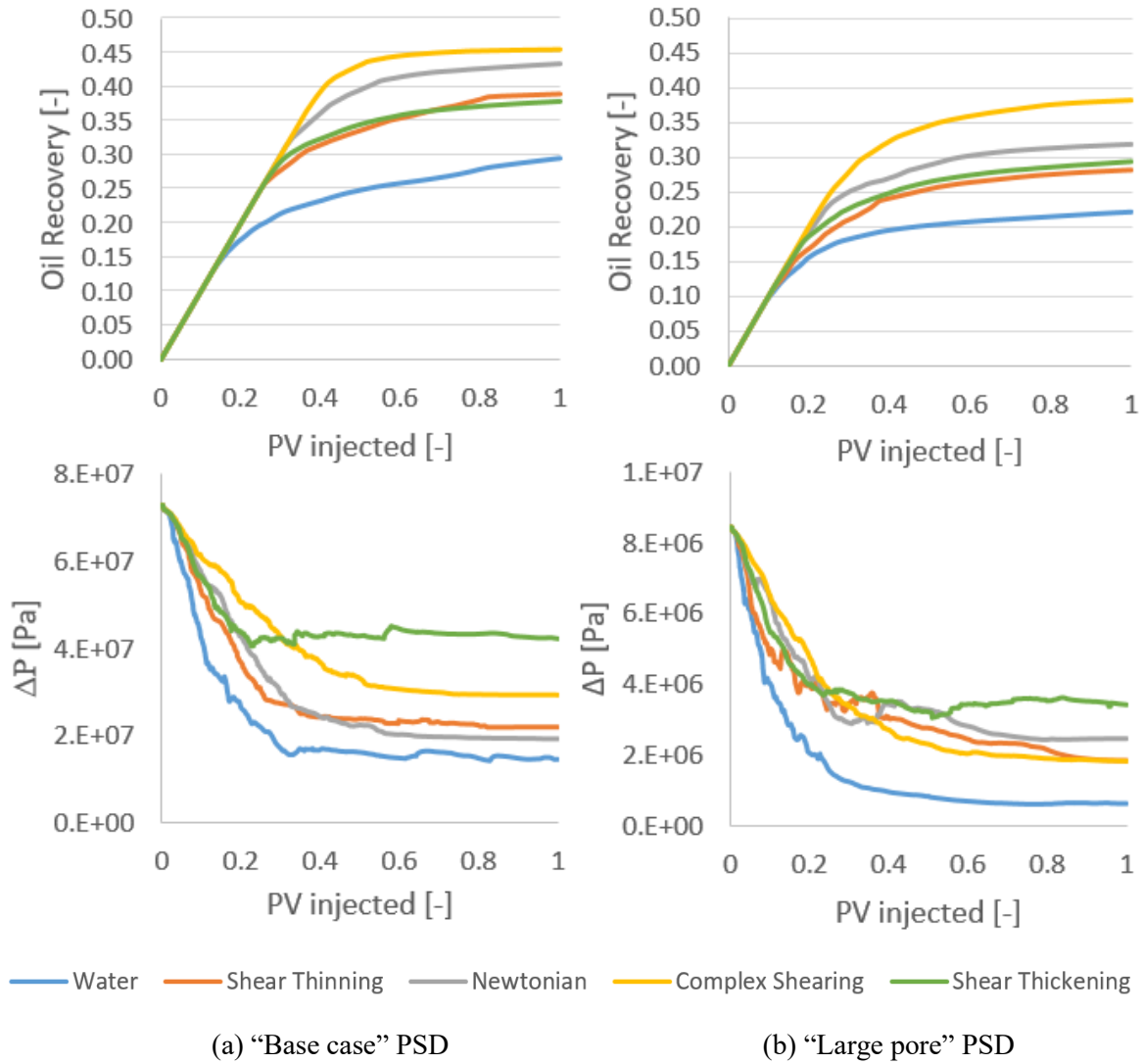


Figure 7.20: Oil production and differential pressure vs PV injected for the two PSD cases (a) and (b).

Every rheology model shows a decreased oil recovery for the “Large pore” PSD. Larger pores means lower velocity and pressure which is clear from values in pressure plot, Figure 7.20 (b). The trend of showing a high ΔP early on seems to play a similar role when predicting which rheology model performs the best. This however, has generally been observed to apply for simulations during the *main period of oil recovery*, in the case of “Large pore” PSD the rheology models seem to produce a significant amount of oil after breakthrough. This may indicate that the ordering of ΔP up to BT is significant even though large portions of the production happens after breakthrough. Oil occupancy across pore radii is presented in Figure 7.21.

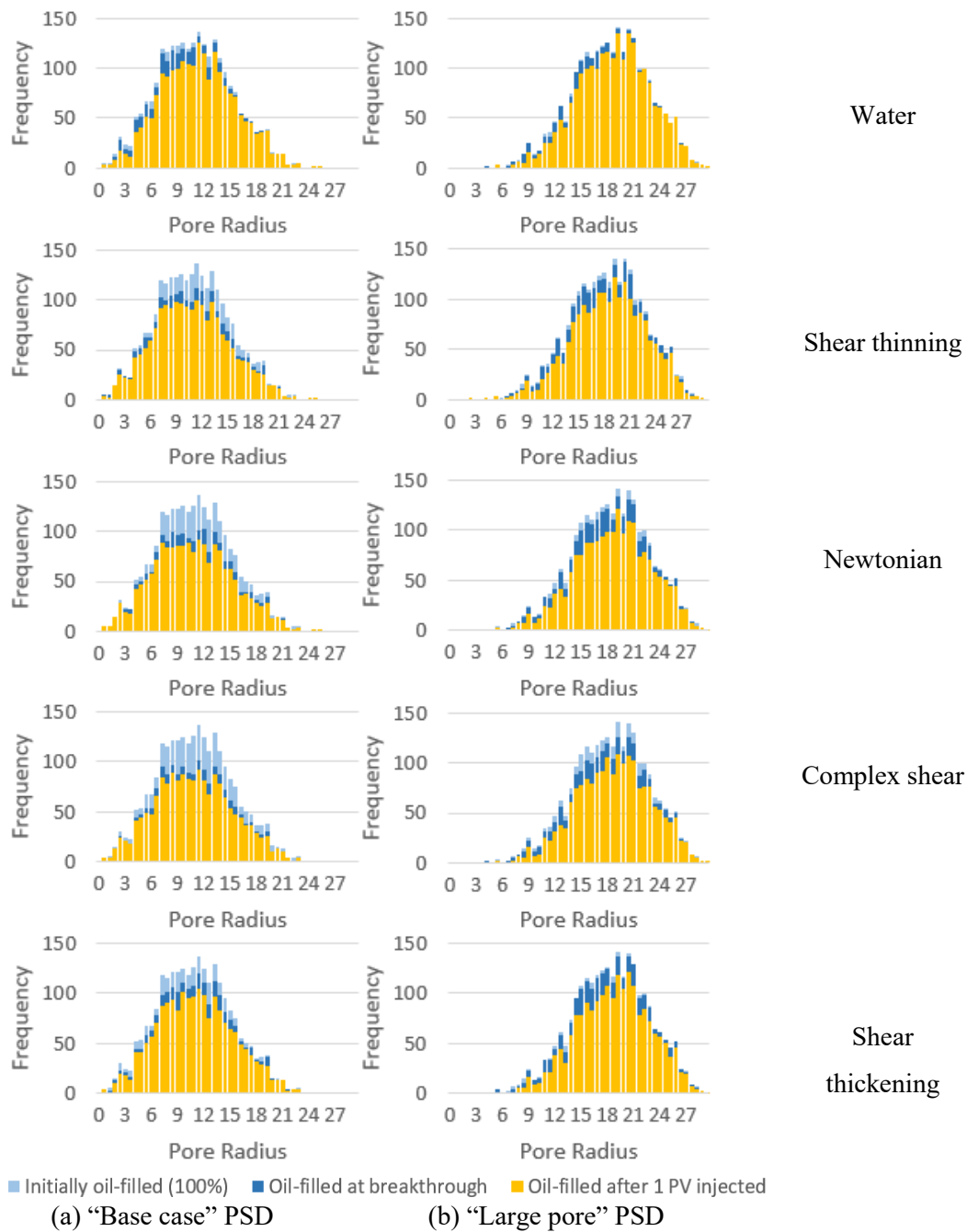


Figure 7.21: Oil filled bonds for (a) "base case" PSD, (b) "large pore" PSD. Light blue is the initial oil-filled bonds, dark blue is the oil-filled bonds at breakthrough, yellow is the oil left behind after 1 PV injected.

As previously stated, the "base case" PSD simulations displace more of the medium sized pores. When the mean radius is increased from 10 to 20, in the "large pore" PSD, there are fewer bonds of these radii. Two main observations are made here from Figure 7.21: (1) A fewer number of bonds are displaced for "large pore" PSD across all simulations. (2) All polymer rheology behaviors show a significant increase in bonds displaced *after* breakthrough for "large

jumps in intensity. This is might be due to there being more of the smaller and larger pores, making the pressure regime more volatile.

The rheology models show less of a difference in oil recovery between them with the pore size distribution being uniform. It is therefore interesting to look at the cumulative water-filled bonds after 1 PV across the radius range, as in Figure 7.24.

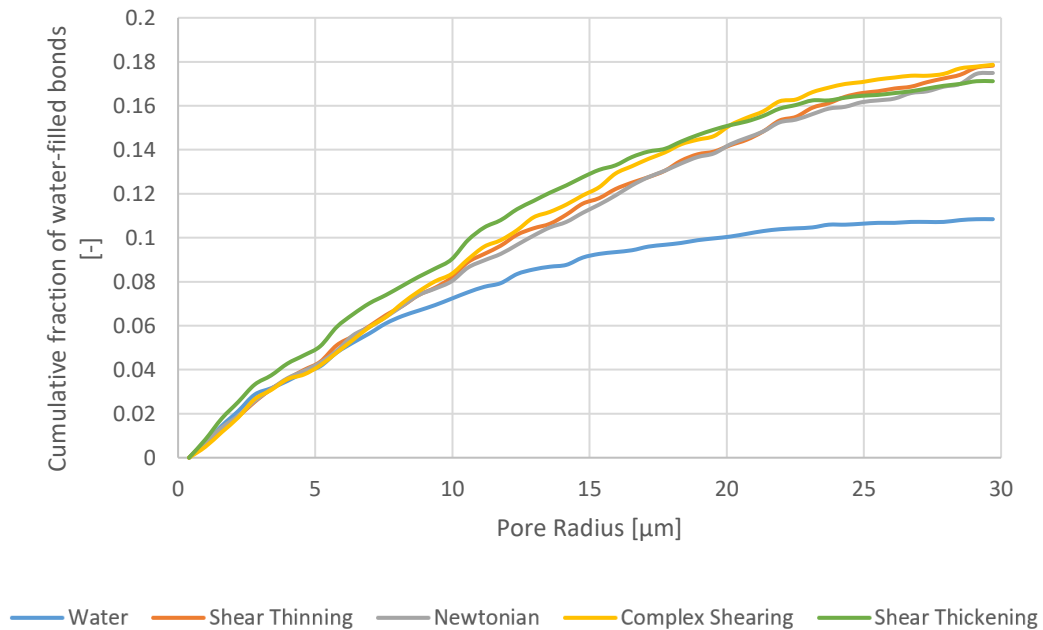


Figure 7.24: Cumulative fraction of water-filled bonds after 1 PV injection across rheology models for the “uniform” PSD.

Figure 7.24 shows the different polymer rheology models displace a similar amount of bonds when we look at accumulated bonds. Water is less effective than the polymers from pore radius $\sim 7\mu\text{m}$ and upwards. Shear thickening ends up displacing the least amount of bonds in total despite leading up until about pore size $20\mu\text{m}$. To investigate the bond displacements in more detail, we look at the accumulated water-filled bonds in parts in Figure 7.25.

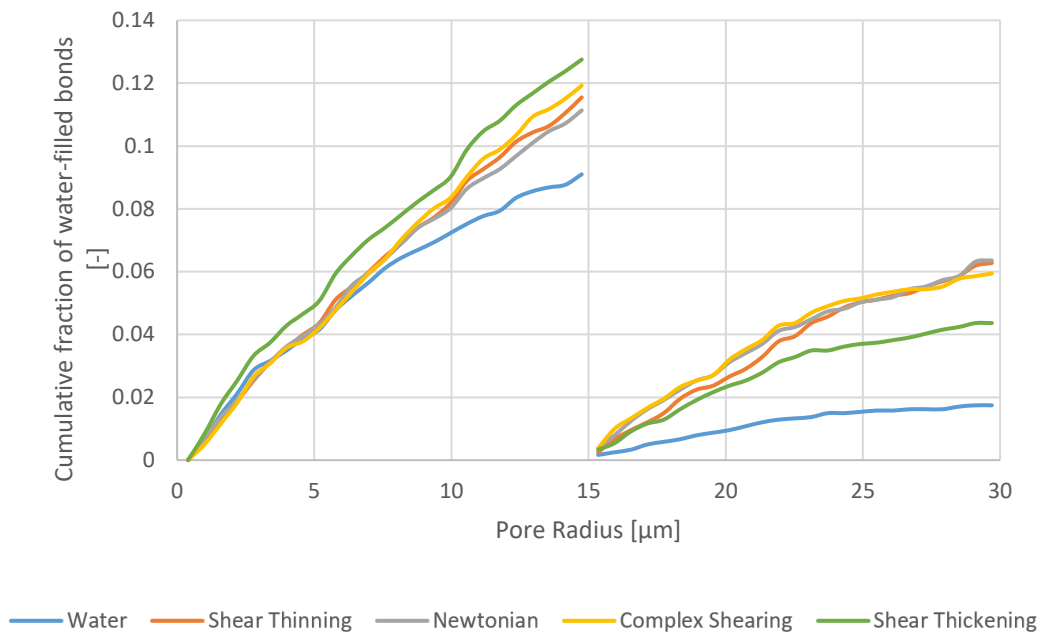


Figure 7.25: Cumulative fraction of water-filled bonds after 1 PV injected fluid. Divided into two sections: small bonds $[0\mu\text{m}, 15\mu\text{m})$ and large bonds $[15\mu\text{m}, 30\mu\text{m}]$.

Figure 7.25 reveals that the pure shear thickening model outperforms every rheology model up to $15\ \mu\text{m}$. However, it also shows that it does not displace as many large pores thus resulting in a low oil recovery. It is now possible to distinguish the three remaining polymer rheology models (Newtonian, shear thickening and complex shearing). The models displace the same amount of bonds up until about $10\ \mu\text{m}$. From $10\ \mu\text{m}$ to $\sim 27\ \mu\text{m}$ the complex rheology displaces the most bonds and therefore is the most effective rheology model in this case as well.

7.5 Reducing Injection Rate

In this chapter, we would like to reduce the injection rate to see if the trends observed thus far still hold. The differential pressures found for the simulations carried out in the base case vary within the range ~ 800 to ~ 200 bar. This is not a realistic range for pressures in a pore segment as small as the ones dealt with so far. By reducing the injection rate by a hundredth ($Q = 1 * 10^{-10} m^3 /s$), the pressures should drop by a similar factor, and in turn reduce bond velocities. The injection rate is carefully chosen not to overstep the boundaries of the pressure solver used by the network code. For smaller injection rates, the code encounters numerical instabilities. Due to the changing the injection rate, the polymer parameters governing the onset of shear thinning and shear thickening behavior are once again adjusted. The models now intersect at $Q = 10^{-10} m^3 /s$ and $\bar{\mu}_p = 5.44 cP$ as shown in Figure 7.26.

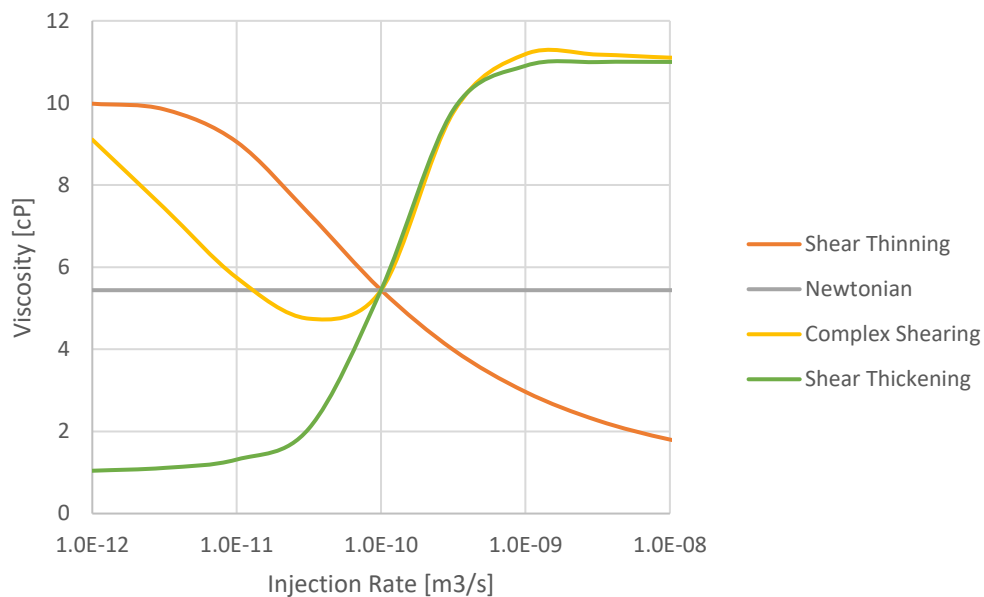


Figure 7.26: Polymer parameters are adjusted so that the rheology models are evaluated at the same injection rate and apparent viscosity.

Oil recovery and differential pressure vs. pore volume injected is presented in Figure 7.27.

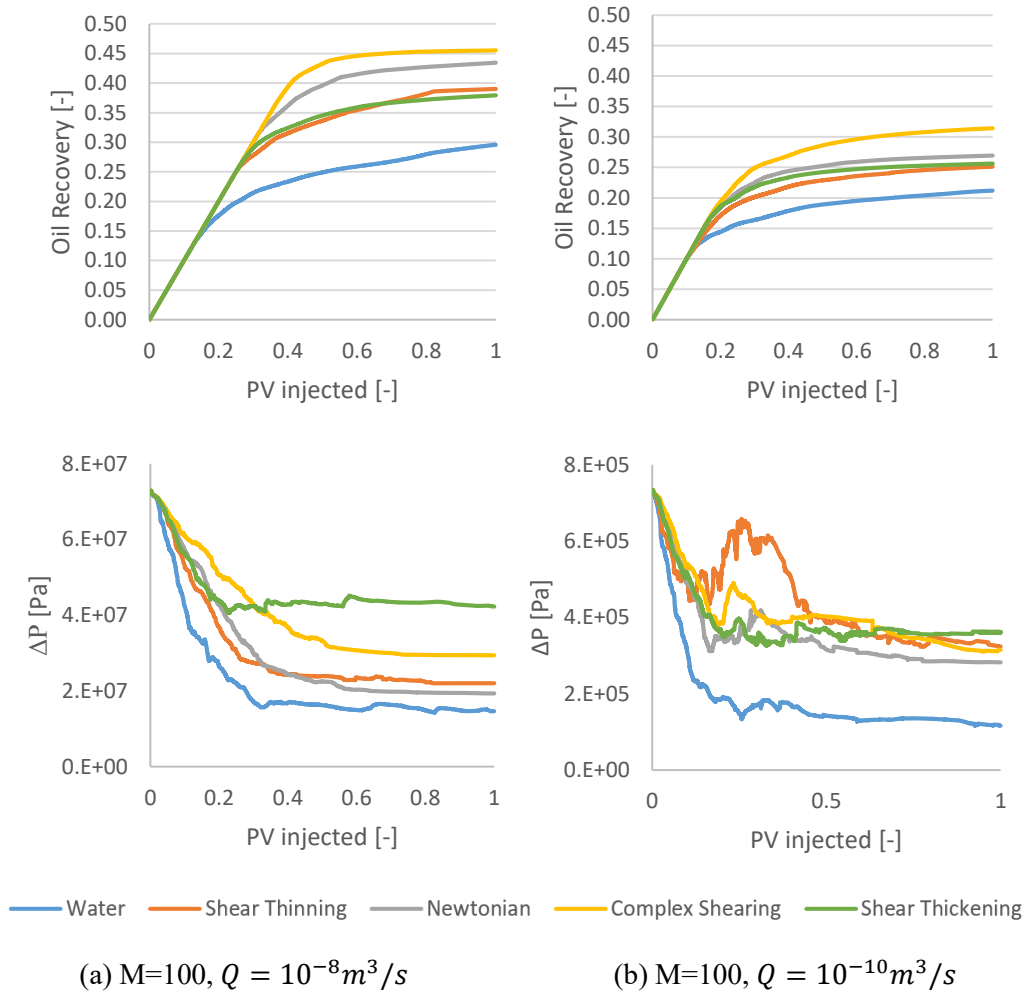
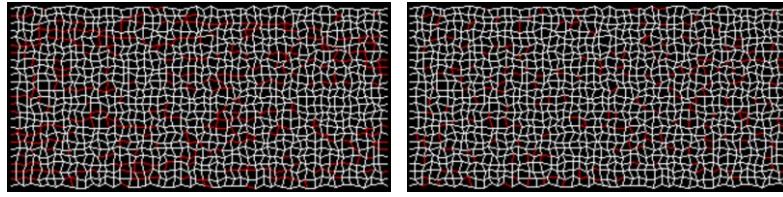


Figure 7.27: Oil recovery and differential pressure vs PV injected for the base case injection rate (a) and the lowered injection rate (b).

Figure 7.27 shows that pressure was successfully lowered by a factor of 100. Pressures are now within a range of 8 to 2 bar, which is closer to a realistic case. As expected, the oil recoveries drop across all rheology models. BT seems to occur earlier, especially for the polymer rheology models. The general oil recovery trends observed this far in the thesis still hold. Assessing the order of ΔP across the polymer rheology models is less straightforward than in the base case. It is however, perceptible that the complex rheology model has the highest ΔP up to 0.1 PV and that the shear thinning and shear thickening show lower ΔP in the same range.

The reduction of injection rate also influences the fluid distributions after waterflooding:



(a) $M=100, Q = 10^{-8}m^3/s$ (b) $M=100, Q = 10^{-10}m^3/s$

Figure 7.28: Final fluid distribution across pore network after 1 PV injected by waterflooding. Red is water, white is oil.

The water in 7.28 (b) looks to be disconnected and “spotty” throughout the network. This is because water now displaces oil by snap-off to a larger degree than in (a). Pores do not turn red (water-filled) unless fully filled with water. Recall from chapter 6.1, equation 6.1, the switch parameter λ , which controls if the flow is capillary or viscous dominated. Reducing the injection rate leads to a reduction in viscous forces (differential pressure), making the flow more capillary dominated (i.e. λ closer to 1). This switch parameter is visualized vs. pore volume injected in Figure 7.29.

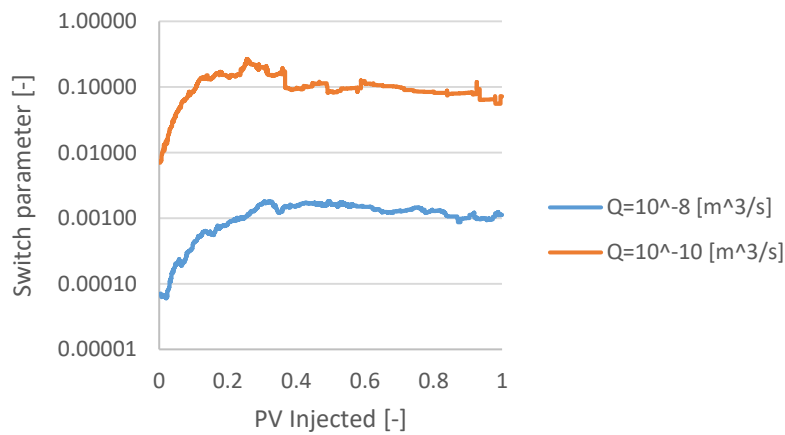


Figure 7.29: Switch parameter vs. PV injected for the two injection rates investigated for waterfloods. The switch value can vary from 0 – fully piston-like displacement to 1 – fully snap-off displacement. N.B: y-axis is displayed logarithmic.

Figure 7.29 shows how dramatically the injection rate influences the switch parameter. The switch parameter increases sharply in the beginning because in this area the differential pressure falls substantially.

Figure 7.30 shows the velocity distribution.

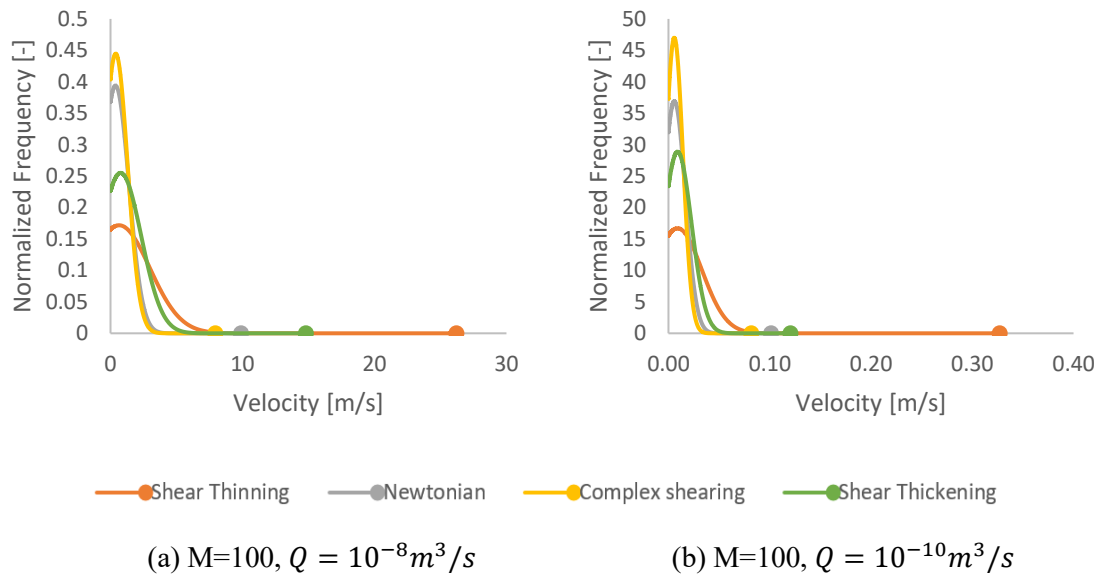


Figure 7.30: Velocity distribution for the models (a) and (b) across polymer rheology behaviors.

Figure 7.30 shows that the velocity is within the network is reduced by a factor of 100 as expected, and that the distribution trend is very similar.

Finally, in Figure 7.31, we compare oil occupancy across pore radii for this case and the base case. All the simulations show a reduced number of bonds being displaced, especially the larger bonds. Comparing the waterflood to the polymer simulations in (b) the most notable difference is that the polymers displace more bonds prior to BT. Only a miniscule amount of large bonds are displaced by the polymer models. When comparing the polymers of (a) and (b) the only improvement in oil displacement is seen in the smallest bonds.

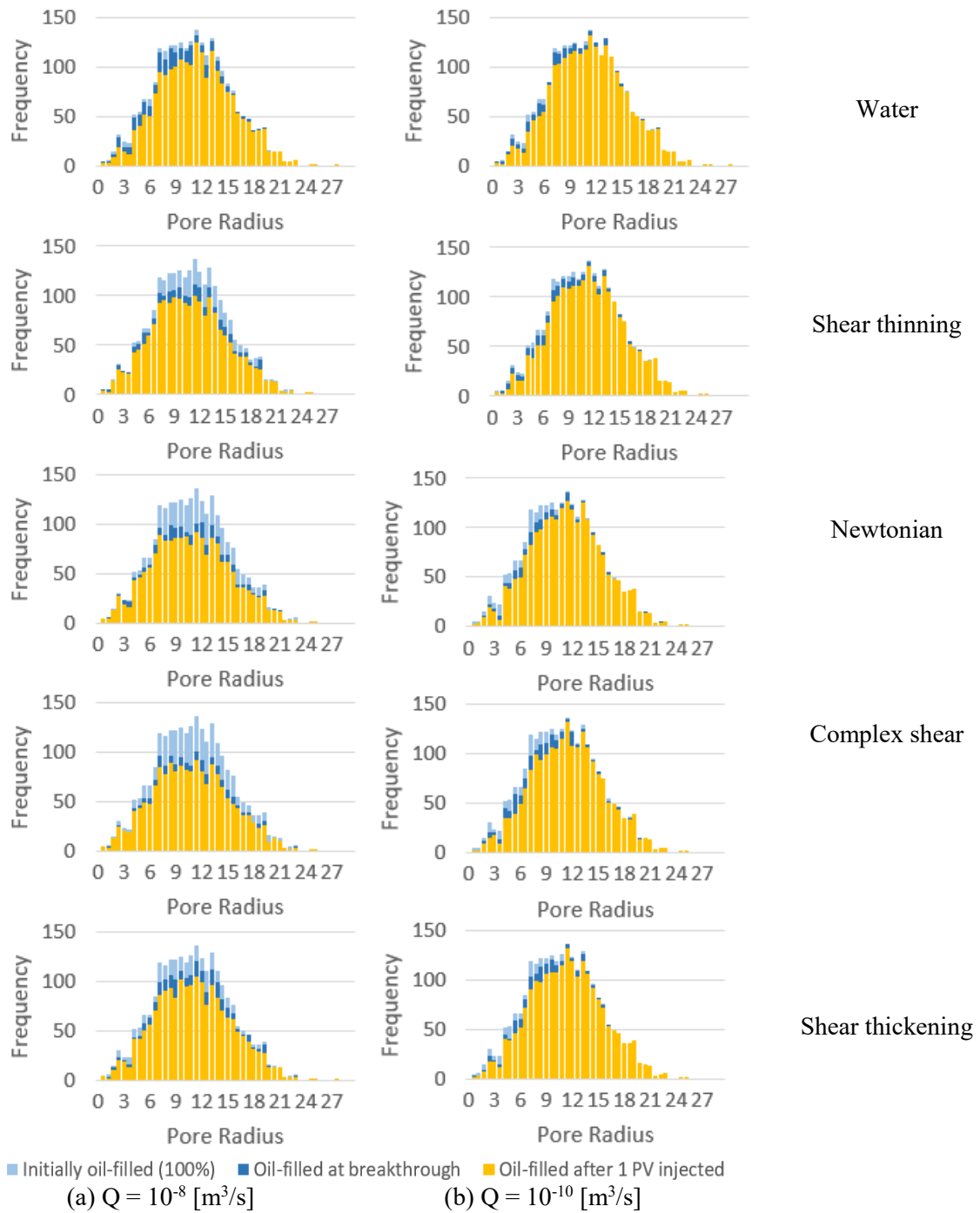


Figure 7.31: Oil filled bonds for the two cases (a) and (b). Light blue is the initial oil-filled bonds, dark blue is the oil-filled bonds at breakthrough, yellow is the oil left behind after 1 PV injected.

7.6 Expanding Network Length

In this chapter, the model is extended in the x-direction from 50 to 100 nodes. The capillary number will remain the same as in the base case, because the inlet area is not affected by the change. The simulations can therefore still be carried out at $Q = 10^{-8}m^3/s$. Fluid distributions after waterflooding is illustrated for the grid sizes in Figure 7.32.

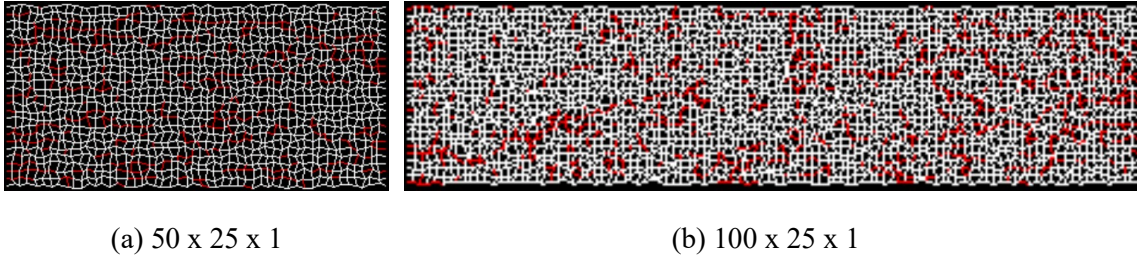


Figure 7.32: Fluid distributions after waterflooding for the two network grid sizes (a) and (b). White is oil, red is water.

Increasing the network size influences ΔP for polymer- and waterflooding across the sample in a single-phase injection. This means that polymer parameters need to be altered in order for the rheology models to intersect at $\overline{\mu}_p = 5.44cP$ for the given injection rate Q . Oil recovery and differential pressure vs. pore volume injected is presented in Figure 7.33.

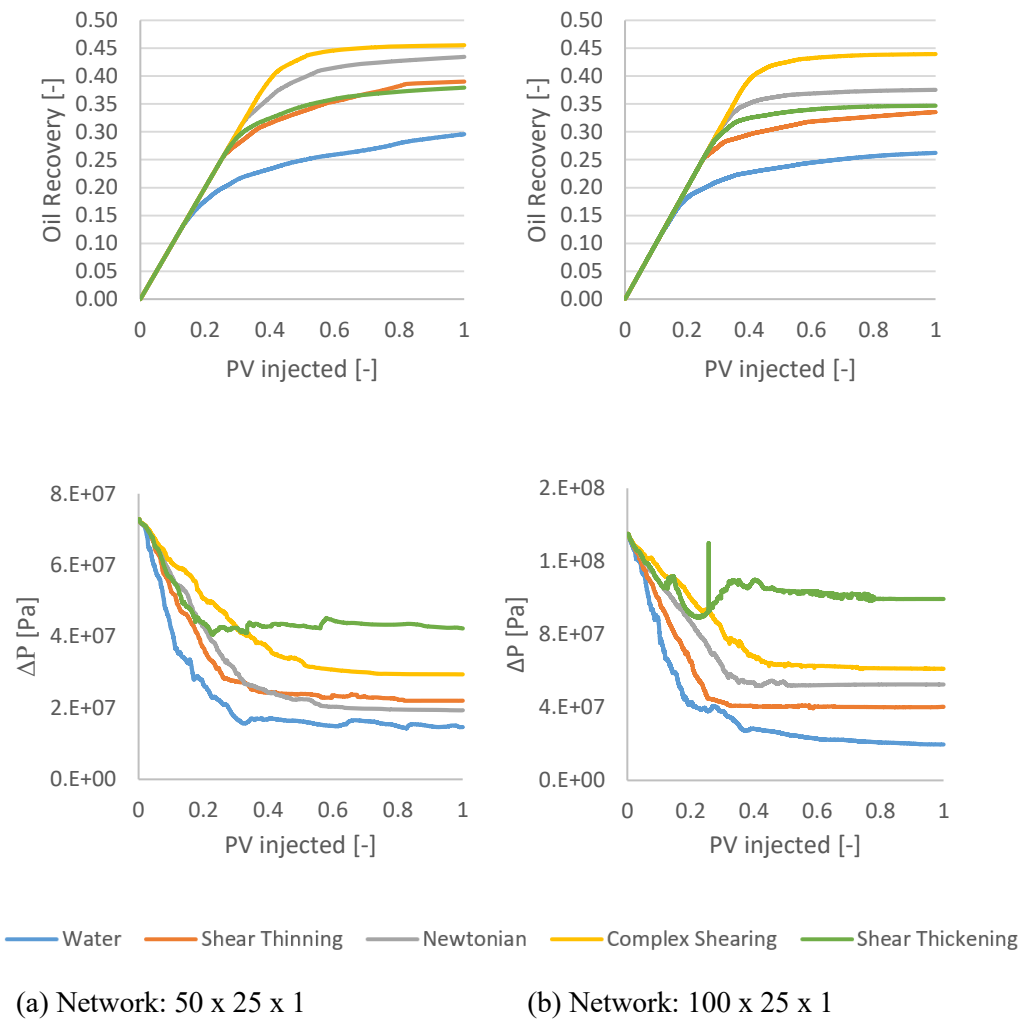


Figure 7.33: Oil recovery and differential pressure vs. PV injected for the two different network size cases (a) and (b).

The oil recovery in the extended model follows the same trends as have been observed earlier. The endpoint oil recoveries across the simulations are reduced; however, the complex rheology is less influenced. The simulations reach BT at around the same fraction; however, the production after BT is reduced for all simulations except the complex shearing rheology. The differential pressures in (b) are roughly twice as high compared to the pressures in (a). This matches well with the fact that the model is twice the size. The pressures for the shear thinning, Newtonian and complex shearing rheology models flatten more abruptly than in (a) and is more or less constant until the end of the simulation. The abrupt pressure increase seen for the shear thickening rheology is briefly investigated in the Appendix (A.2).

Oil occupancy distributions are presented at different stages in Figure 7.34.

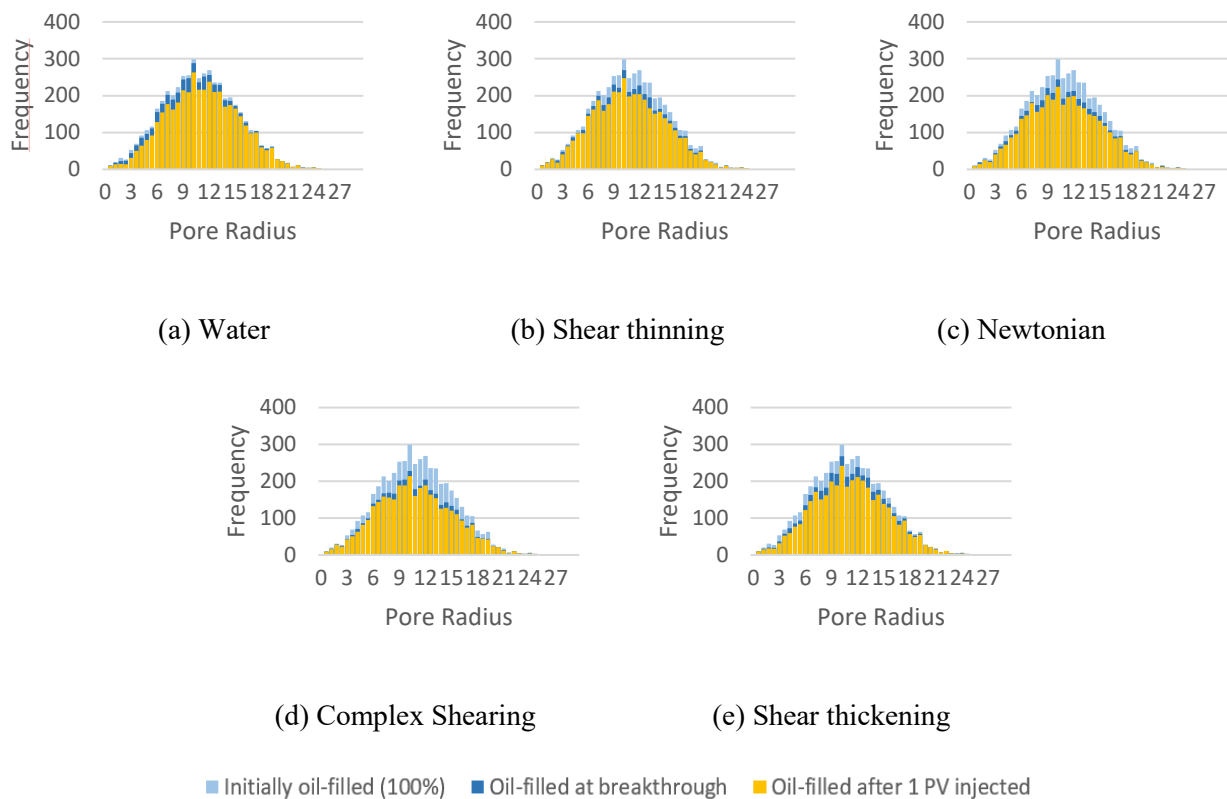


Figure 7.34: Oil filled bonds for the extended network: 100 x 25 x 1. Light blue is the initial oil-filled bonds, dark blue is the oil-filled bonds at breakthrough, yellow is the oil left behind after 1 PV injected.

Oil occupancy across pore radii are shown in Figure 7.34. The various rheology models agree very well with the distribution presented and discussed in the base case (Figure 7.7). There is however, a small difference for shear thinning as it displaces slightly fewer medium-sized bonds prior to BT. This agrees well with the endpoint oil recovery, as the shear thinning rheology falls behind the shear thickening model.

7.7 Network Model Expanded to Three Dimensions (3D)

The network model is now altered to describe a network in three dimensions (3D). The simulations are run for a network size of $20 \times 10 \times 10$. The network is still fully coordinated, meaning the average coordination number is increased from 4 to 6. The injection rate was increased in order to counter the decrease to inlet area, thus keeping the capillary number in line with the one used in the base case. Polymer properties regarding the onset of shear thinning and shear thickening behavior were altered to accommodate this new injection rate, meaning the rheology models still show an apparent viscosity of $\bar{\mu}_p = 5.44 \text{ cP}$ (Figure 7.35). The injection rate was adjusted from $Q = 1 \cdot 10^{-8} \text{ m}^3/\text{s}$ to $Q = 2.42 \cdot 10^{-7} \text{ m}^3/\text{s}$ in order to keep the capillary number constant.

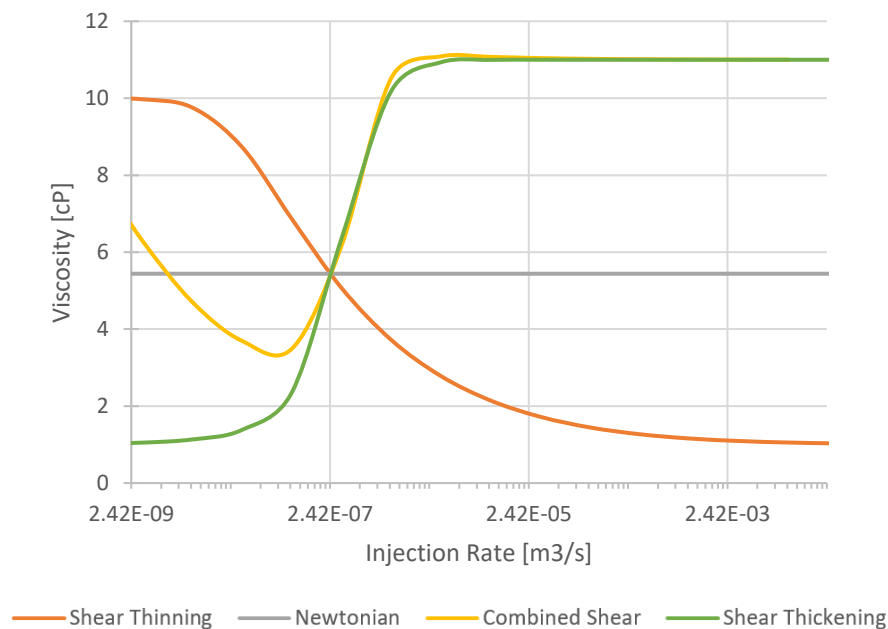


Figure 7.35: In-situ rheology for the four cases investigated showing their point of intersection ($Q_{inj} = 2.42 \cdot 10^{-7} \text{ m}^3/\text{s}$ and $\bar{\mu}_p = 5.44 \text{ cP}$).

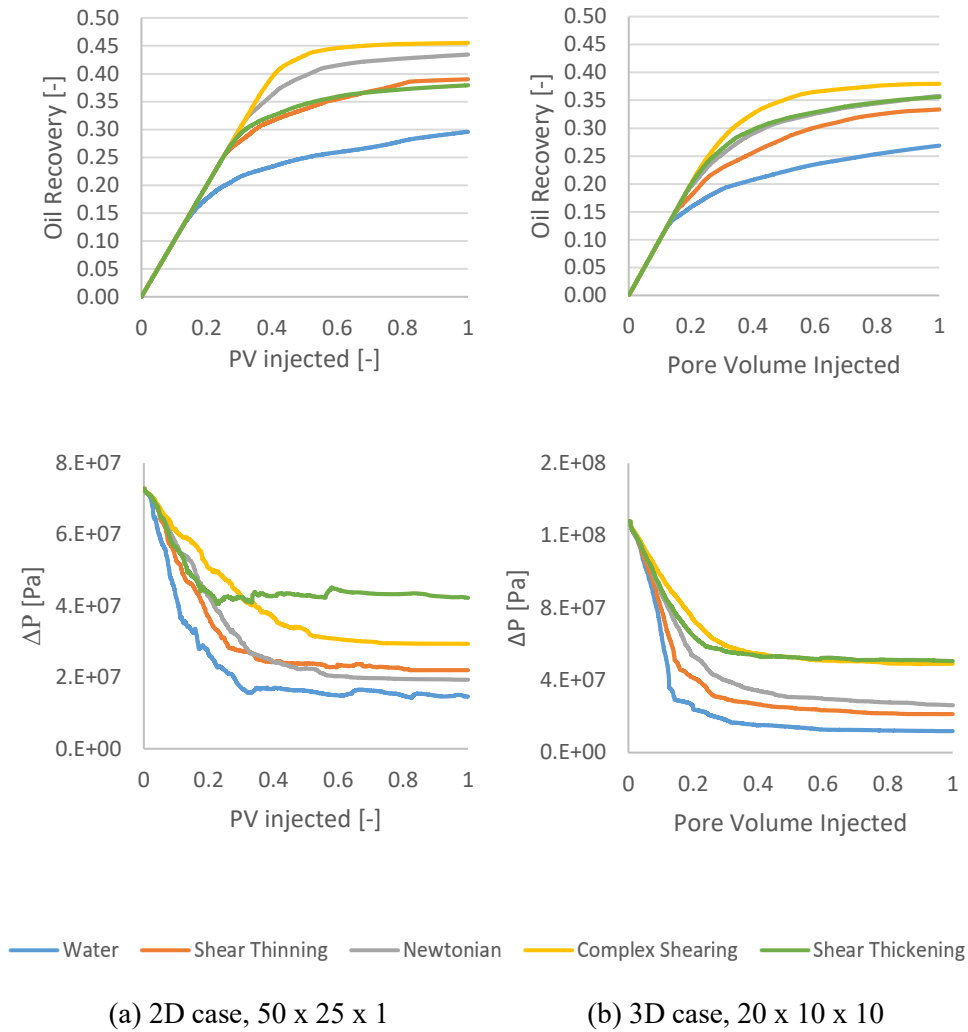
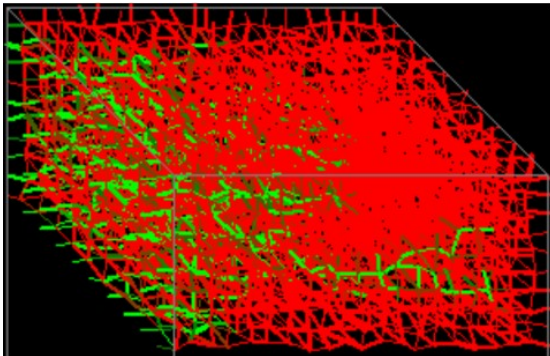


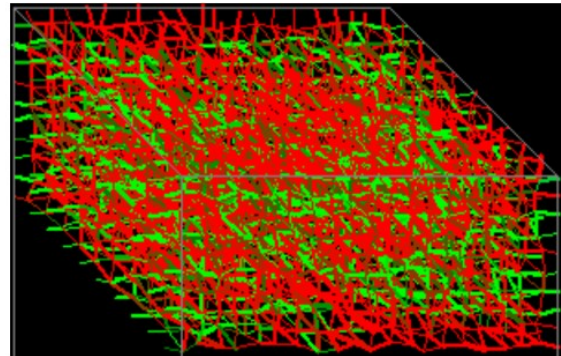
Figure 7.36: Oil recovery and differential pressure vs. PV injected for the two cases (a) 50 x 25 x 1 (two-dimensional) and (b) 20 x 10 x 10 (three-dimensional).

Figure 7.36 shows that the oil recovery is reduced for all rheology models. The pressure curves are less jittery for the 3D case. The coordination number is increased from 4 to 6, so the displacing fluid has more options to divert flow towards bonds that are more easily entered. Breakthrough occurs at lower PV injected because the model has fewer (20) nodes from inlet to outlet. After breakthrough, a significant amount of oil is produced, probably because the fluid now can be diverted in three dimensions within the network.

Figure 7.37 shows 3D fluid distributions for the Newtonian polymer (a) just before breakthrough (b) after 1 PV injected.



(a) 3D model before BT



(b) 3D model at 1 PV injected

Figure 7.37: Fluid distribution for the three-dimensional model, 20 x 10 x 10. (a) just before BT and (b) after 1 PV injected. Oil is red and polymer is green.

Because of the added dimension of Figure 7.37, it is not easy to compare fluid distributions between rheology models after 1 PV injected. However, snapshots during the displacement can be valuable as in Figure 7.37 (a), where significant fingering is observed prior to breakthrough. This would not be evident just by looking at Figure 7.37 (b), where polymer is well diverted into adjacent bonds.

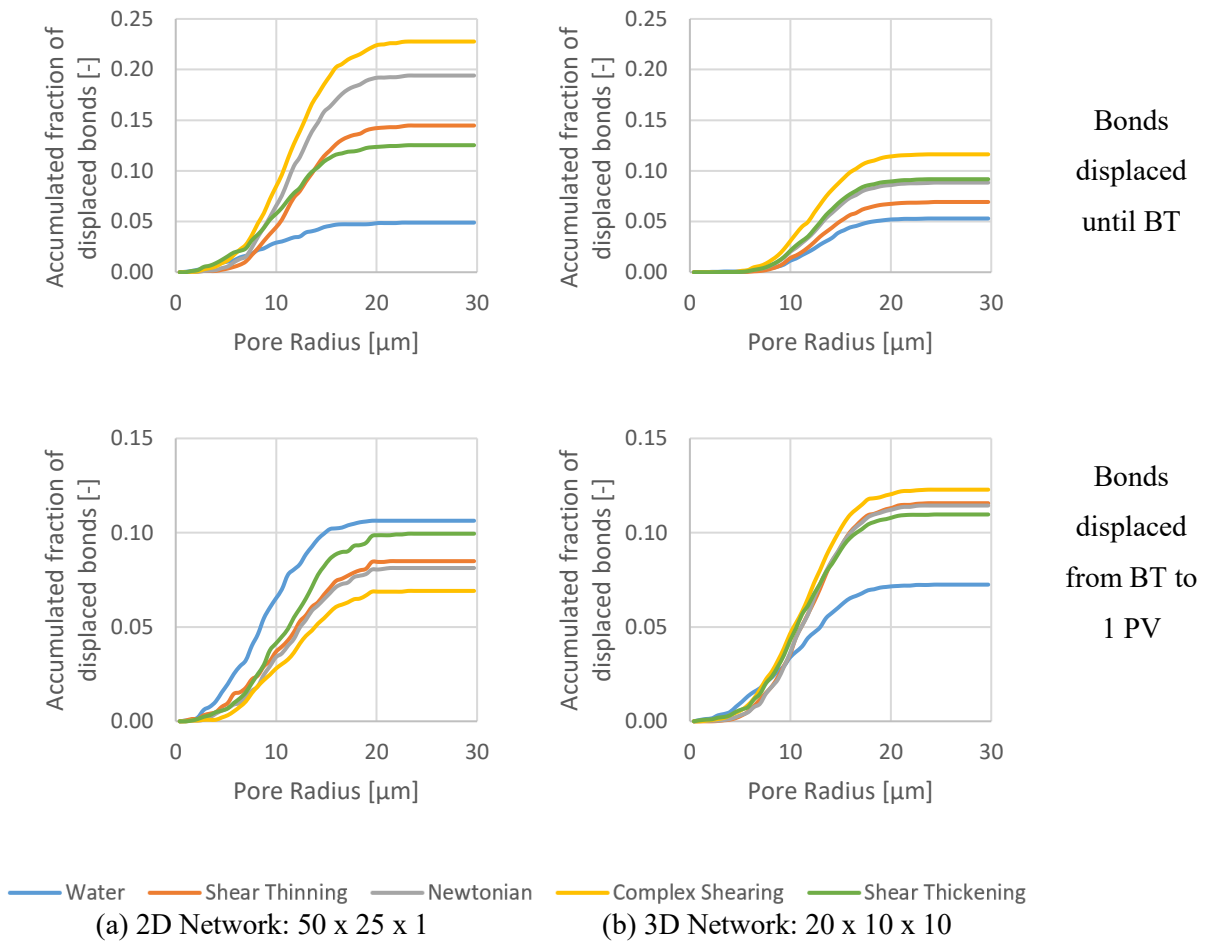


Figure 7.38: Accumulated fraction of bonds that have been displaced until BT (top) and from BT to 1 PV injected (bottom) for the 2D and 3D cases (a) and (b), respectively.

Figure 7.38 shows that for the 3D case, the amount of bonds displaced before and after BT are similar (e.g. complex shearing shows ~ 0.12 before and after). The complex rheology model displaces the most bonds both before and after BT, whereas water displaces the least in the same period.

For the 2D case, it is clear that most of the bonds are displaced before BT for the four polymer rheology models. What is interesting is that the order of which model displaces the most bonds after BT is reversed, so that water displaces the most bonds after BT in this case.

8 Summary and Conclusions

8.1 Summary of sensitivity analysis

Chapter 7.1: Adverse Viscosity

Running simulations across adverse viscosity ratios showed reduced oil recovery. Polymers increased oil recovery for all viscosity ratios. The oil production after breakthrough decreased with increasing viscosity ratios. Despite the rheology models showing the same single-phase apparent viscosity, they behave very differently when flowing through the pore network. The complex rheology model provided the best oil recovery for all viscosity ratios.

For the viscosity ratio $M=100$, the shear thinning and shear thickening models ended up with similar oil recovery. Looking at the viscosity distribution, the shear thinning rheology had a higher, more favorable, viscosity than the shear thickening rheology. However, it also had the highest velocity distribution, showing that it had fewer of the low-velocity bonds.

The best performing rheology model, the complex shearing, displaced a wide range of pores and mostly before breakthrough. The worst, waterflood, displaced mostly small and some medium sized pores and mostly after breakthrough. Water displaces the model fast because of viscous fingering, but is able to produce a significant amount of oil despite the unfavorable viscosity ratio, $\mu_o = 100cP$ and $\mu_w = 1cP$.

The accumulated bond displacements showed that the ordering of which model displaced most/least was reversed when looking at bonds displaced before and after breakthrough separately.

Chapter 7.2: Polymer Viscosity

Here the simulations from the base case $M=100$, was compared with a simulation with $M=1000$. The polymer viscosity was however increased by a factor 10, to see how the rheology models compared to the ones in the base case.

The simulations had similar oil recoveries, apart from the shear thickening model, which had a large increase in oil recovery. The model had a more favorable viscosity distribution, and a wider velocity distribution, which is likely the reason for the increased oil recovery. This is

consistent with experimental and numerical studies where an increase in polymer concentration has been known to influence the onset of extensional viscosity. The pore occupancy models showed that the shear thickening model displaced more medium and large bonds prior to breakthrough. It also displaced less of the smaller bonds in total.

Chapter 7.3: Coordination Number

The average coordination number was lowered, this influences the accessibility of the model and a drop in oil recoveries was observed. The general oil recovery trends were similar to the base case. The order of differential pressure up until breakthrough for the models seem to still dictate the oil recovery as previously observed for the base case.

Compared to the fully coordinated base case, water mostly swept medium pores and had its breakthrough delayed. The opposite happened for the complex rheology, where breakthrough occurred earlier.

Chapter 7.4: Pore-size Distribution

Here two alternative pore-size distributions were simulated, one with a larger mean radius called “large” PSD, and a uniform distribution called “uniform” PSD.

For the “large” distribution, a decrease in oil recovery was seen across all rheology models. The simulations had earlier breakthrough, but managed to produce much oil afterwards. The order of differential pressure until breakthrough seemed to correlate well with the final oil recovery across the models. When this observation was first reported in the paper by Zamani et al. [1] it was stressed that this might only be valid under the “main period of oil production”. In this case, however, oil production is significant after this point and the observation is still valid for this case.

The “uniform” distribution also had a lower oil recovery. The differential pressure graphs were less usable due to the pressure being more unstable. It was suggested that the pressure was highly influenced by the fact that more small and large pores are present in the model. Previously observed trends in oil recovery across rheology models were still valid. When the accumulated bonds displaced was investigated, the polymer rheology models were seen to displace a similar amount of bonds across the pore-size distribution.

Chapter 7.5: Injection Rate

In this part, the injection rate was lowered in order to get pressures and flow rates that are more realistic. The pressure and velocity plots showed a good correlation with the reduction in injection rate. Oil recovery dropped across simulations and the polymers saw earlier breakthroughs. The fluid distribution after waterflooding showed an apparent increase in snap-off displacements. This behavior was confirmed by comparing the switch parameter, λ , with the base case. It was significantly higher throughout the displacement, meaning the flow was more capillary dominated (i.e. more snap-off). This behavior is easily understood by looking at equation 6.1, where a reduction in viscous forces clearly increases the switch parameter.

In the bond occupancy plots it was clear that fewer bonds were displaced for all rheology behaviors for the reduced injection rate. Large bonds were almost untouched by both polymers and water, leaving only small to medium bonds being displaced.

Chapter 7.6: Extended 2D Network

The simulations saw a drop in oil recovery, but the complex shearing rheology was less reduced. This was mainly due to the other rheology models producing less oil after breakthrough than before. Oil recovery trends were mainly the same as in the base case. The same was seen for the bond occupancy distributions. A minor difference was observed for the shear thinning model as it displaced fewer of the medium sized bonds prior to BT, and therefore fell below the shear thickening rheology in oil recovery.

Chapter 7.7: 3D Network

For this case, a drop in oil recovery was observed. The models showed early breakthrough, probably because the model was reduced to 20 bonds from inlet to outlet. Pressure curves were observed to be much smoother than before, possibly due to the increase in coordination number. Similar to the “large” PSD, a lot of oil was produced after the early breakthrough. Once again, the order of pressures until breakthrough correlated well with the final oil recovery. The fluid distribution snapshots illustrated that the Newtonian polymer did not sweep the model well before BT.

8.2 Main observations

The simulations showed that the polymer floods had higher oil recovery than waterfloods for all the cases investigated. This comes as no surprise because the polymer adds to the viscous forces, influencing the switch parameter (Eq. 6.1) in a way that enables more piston-like displacements. However, the rheology models were tuned in a way that for a given constant injection rate they showed the same apparent viscosity. When the fluids propagate through the pore network, their velocities will vary with pore size. Therefore, large differences were observed across the polymer rheology models.

In the preliminary stages of this thesis, the result obtained by Zamani et al. for the viscosity ratio $M=100$ was reproduced and then compared to higher viscosity ratios, $M=1000$ and $M=10000$. Oil recovery trends and their coupling to differential pressure prior to breakthrough were found to be valid for these cases as well.

Further sensitivity testing of the code was conducted for a variety of fluid and network properties: polymer concentration, network geometry, injection rate, network size in 2D and 3D. The oil recovery and pressure trends previously found across the polymer rheology models were largely maintained across the sensitivity tests with some exceptions. Improved oil recovery and viscosity distribution was seen for the shear thickening model in Chapter 7.2. This behavior is consistent with some experimental (Chauveteau) and numerical (Zamani et al.) studies regarding the effect polymer concentration may have on the onset of extensional viscosity [36], [41].

Oil/water occupancy distributions proved to be a powerful tool when visualizing local bond displacements throughout the displacement processes (i.e. at BT and 1 PV injected). It showed that the polymers tend to displace medium-sized pores, whereas the waterfloods mainly target the small pores. The occupancies also revealed that the polymers that displaced the highest number of bonds before breakthrough often displaced the least after breakthrough.

The complex rheology model proved to be the most robust across all the simulations performed in this thesis. This is due to the model being able to exhibit favorable viscosities across a large range of shear rates. The Newtonian rheology model usually followed with the second highest recovery and then the shear thickening and shear thinning models. The latter two models performed variably because they are the most sensitive to variable flow rates. The order of oil

recovery by rheology model is in agreement with an experimental study (Vik et al. [42]), where bentheimer rock slabs were displaced by secondary injections of polymer solutions. They found that HPAM (complex rheology) had the most efficient oil recovery, followed by glycerol (Newtonian rheology) and Xanthan (shear thinning rheology).

The differential pressures observed for the injection rate of $Q = 10^{-8}m^3/s$ started at ~ 800 bar for the base case $M=100$. In some of the other results, the pressures were even higher. This pressure is high for such a small model, and the resulting bond velocities are unrealistically high. An attempt was made to remediate this by lowering the injection rate by a hundredth, to $Q = 10^{-10}m^3/s$. It was not possible to lower this further due to the pressure solver encountering numerical instabilities for lower injection rates. The results showed differential pressures starting at a much better ~ 8 bar, with the same oil recovery trends across rheology models.

The results from the 3D simulation followed the same oil recovery trends as seen for the various 2D cases. This helps strengthen the generality of the findings from the 2D simulations, as real porous media is three-dimensional.

8.3 Conclusions

In this thesis, a dynamic pore-scale network model has been tested for waterflooding and polymer flooding. Four different polymer rheology models were tuned so that for a constant injection rate, the polymers show the same apparent viscosity for single-phase displacement.

The pore network model represents a small part of the porous medium, and therefore exemplifies possible changes in microscopic displacement. All simulations with polymer led to a higher oil recovery compared to the waterfloods. The results contribute to the discussion of viscoelastic effect or, more general, non-Newtonian behavior and influence of oil recovery.

The polymer rheology models showed consistent oil recovery and pressure trends throughout parametric sensitivity testing. The order of ΔP among rheology models until breakthrough correlated well with the final oil recoveries, even for cases where much of the oil was produced after breakthrough.

The various polymer rheology models displaced more bonds and larger bonds compared to the waterfloods. Much of the difference is attributed to the polymers being able to displace more bonds before breakthrough. There were differences among the rheology models as well, where the shear thinning and shear thickening models displaced slightly different bond sizes. The complex model consistently displaced the most bonds at a wide range of pore sizes.

Throughout the sensitivity testing in this thesis, the complex rheology model can be regarded as having the optimal rheology behavior. It consistently had the highest oil recovery of the rheology models, likely because it has the ability to maintain a high viscosity for a wide range of flow velocities. The effectiveness of each rheology model found in the simulations is in agreement with experimental results shown for polymers with similar rheology behavior. It is however important to stress that this may not always be the case, and could change for other conditions and network configurations. The abnormally high pressures recorded may also be an uncertainty with regards to the results.

An unexpected finding from the simulations was the effect that increased polymer concentration had on the shear thickening model. This seems to agree well with the effect higher concentration has on the onset of extensional viscosity.

9 Further work

The pressures found in our sensitivity analysis are very high. If the injection rate is further reduced to accompany this, the pressure solver in the model encounters numerical instabilities. A suggestion for further work is therefore to increase the network size substantially, so that the pressure gradients may decrease and become comparable to field cases. Would the trends and findings of this thesis still hold? With the current model, a drawback would be the long run-time for simulations of these grid-sizes to complete. This however, may not work because the network code only allows at most one pore to fill at a given time-step. Because of this, the local velocities and pressures may still be too high, despite the network size increasing.

The code could also be expanded to allow for surfactant floods, high-salinity and low-salinity waterfloods and mixed wettability such as mixed-wet large, mixed-wet small and fractional wetting.

References

- [1] N. Zamani, I. C. Salmo, K. Sorbie, and A. Skauge, "Numerical Study of Polymer Flow in Porous Media using Dynamic Pore Network Modelling," in *IOR 2019 - 20th European Symposium on Improved Oil Recovery, Pau, France, 2019*, no. April.
- [2] United Nations and D. o. E. a. S. A. United Nations Population Division, "World Population Prospects: The 2017 Revision, Key Findings and Advance Tables," New York, 2017.
- [3] Equinor, "Energy Perspectives 2018, Long-term macro and market outlook," Stavanger, 2018.
- [4] M. Skarestad and A. Skauge, *Reservoarteknikk II, PTEK 213 - Course Compendium*. University of Bergen, Norway, 2012.
- [5] Norwegian Petroleum Directorate, "Norwegian Continental Shelf: A global focal point for boosting recovery," *NPD Factpages*, 2018. [Online]. Available: <https://www.npd.no/en/facts/publications/norwegian-continental-shelf/norwegian-continental-shelf-no.-1---2018/a-global-focal-point-for-boosting-recovery/>.
- [6] I. Sandrea and R. Sandrea, "GLOBAL OIL RESERVES-1: Recovery factors leave vast target for EOR technologies," *Oil Gas J.*, vol. 105, no. 41, 2007.
- [7] Oil & Gas Authority United Kingdom, "Polymer Enhanced Oil Recovery - Industry lessons learned," no. October, p. 44, 2017.
- [8] T. Urbissinova, J. J. Trivedi, and E. Kuru, "Effect of Elasticity during Viscoelastic Polymer Flooding - A Possible Mechanism of Increasing the Sweep Efficiency," *SPE Western Regional Meeting*. Society of Petroleum Engineers, Anaheim, California, USA, p. 12, 2010.
- [9] A. Afsharpoor and M. Balhoff, "Static and Dynamic CFD Modeling of Viscoelastic Polymer: Trapped Oil Displacement and Deformation at the Pore-Level," *SPE Annual Technical Conference and Exhibition*. Society of Petroleum Engineers, New Orleans, Louisiana, USA, p. 7, 2013.
- [10] Y. Bai, X. Zhang, and G. Zhao, "Theoretical analysis of microscopic oil displacement mechanism by viscoelastic polymer solution," *Theor. Appl. Mech. Lett.*, vol. 1, no. 2,

Jan. 2011.

- [11] H. Xia, D. Wang, G. Wang, W. Ma, H. W. Deng, and J. Liu, “Mechanism of the Effect of Micro-Forces on Residual Oil in Chemical Flooding,” *SPE Symposium on Improved Oil Recovery*. Society of Petroleum Engineers, Tulsa, Oklahoma, USA, p. 10, 2008.
- [12] J. Li, “A Pore-Scale Network Modelling Study to Explain the Observed Differences Between Steady-State and Unsteady-State Relative Permeabilities,” Heriot-Watt University, Edinburgh, Scotland, 2016.
- [13] L. W. Lake, J. Russell, and B. Rossen, *Fundamentals of Enhanced Oil Recovery*. Society of Petroleum Engineers, 2014.
- [14] K. S. Sorbie, *Polymer-Improved Oil Recovery*. Glasgow, Scotland: Blackie & Son Ltd, 1991.
- [15] Y. D. Castillo and G. Gillis, “Enhanced Oil Recovery,” *Schlumberger Oilfield Glossary*. [Online]. Available: <https://www.glossary.oilfield.slb.com/en/Terms/e/eor.aspx>.
- [16] Norwegian Petroleum Directorate, “Resource report 2017,” 2017. [Online]. Available: <https://www.npd.no/link/7ecc8e5f11e24738b9cbbbed57cabe3c0.aspx>.
- [17] J. R. Lien, *Grunnleggende reservoar fysikk, PTEK 211 - Course compendium*. Bergen, Norway: Department of Physics and Technology, University of Bergen, 2004.
- [18] Y. D. Castillo and G. Gillis, “Trapped Oil,” *Schlumberger Oilfield Glossary*. [Online]. Available: https://www.glossary.oilfield.slb.com/en/Terms/t/trapped_oil.aspx.
- [19] I. Chatzis, N. R. Morrow, and H. T. Lim, “Magnitude and Detailed Structure of Residual Oil Saturation,” *Soc. Pet. Eng. J.*, vol. 23, no. 02, pp. 311–326, 1983.
- [20] D. Wang, J. Cheng, Q. Yang, W. Gong, Q. Li, and F. Chen, “Viscous-Elastic Polymer Can Increase Microscale Displacement Efficiency in Cores,” *Soc. Pet. Eng. J.*, 2000.
- [21] K. Kamaraj, G. Zhang, Y. Liu, and R. S. Seright, “Effect of Residual Oil Saturation on Recovery Efficiency during Polymer Flooding of Viscous Oils,” *OTC Arct. Technol. Conf.*, p. 9, 2011.
- [22] J. R. Lien, *Reservoarteknikk I, PTEK 212 - Course compendium*. Bergen: Department of Physics and Technology, University of Bergen, 2014.

- [23] A. B. Zolotukhin and J.-R. Ursin, *Introduction to Petroleum Reservoir Engineering*, 2nd printi. Kristiansand, Norway: Høyskoleforlaget, 2000.
- [24] A. Skauge, *PTEK 312 - Pore Scale Physics and Network Modelling*, Fall 2018. Bergen: University of Bergen - Department of Chemistry, 2018.
- [25] J. I. Gates and W. T. Lietz, “Relative Permeabilities of California Cores by the Capillary - Pressure Method,” *Spring Meet. Pacific Coast Dist. Drill. Prod. Pract.*, no. May, pp. 285–302, 1950.
- [26] I. Fatt, “The Network Model of Porous Media,” *Soc. Pet. Eng. J.*, vol. 207, pp. 144–181, 1956.
- [27] J. M. Hammersley, “Percolation processes,” *Math. Proc. Cambridge Philos. Soc.*, vol. 53, no. 03, p. 642, 2008.
- [28] A. A. A. Helba, M. Sahimi, L. E. E. Scriven, and H. T. T. Davis, “Percolation theory of two-phase relative permeability,” *SPE Reserv. Eng.*, vol. 7, no. 01, pp. 123–132, 1992.
- [29] S. R. McDougall, “THE APPLICATION OF NETWORK MODELLING TECHNIQUES TO STEADY- AND UNSTEADY-STATE MULTIPHASE FLOW IN POROUS MEDIA,” Heriott-Watt University, Edinburgh, 1994.
- [30] S. R. McDougall and K. S. Sorbie, “The Impact of Wettability on Waterflooding: Pore-Scale Simulation,” *SPE Reserv. Eng.*, vol. 10, no. 03, pp. 208–213, 1995.
- [31] K. S. Sorbie and M. I. J. Van Dijke, “Fundamentals of three-phase flow in porous media of heterogeneous wettability,” *Inst. Pet. Eng. Heriot-Watt Univ. Edinburgh, Scotl.*, 2004.
- [32] P. E. Oren, S. Bakke, and O. J. Arntzen, “Extending Predictive Capabilities to Network Models,” *SPE Annual Technical Conference and Exhibition*. Society of Petroleum Engineers, San Antonio, Texas, p. 13, 1997.
- [33] A. Skauge, N. Zamani, J. Gausdal Jacobsen, B. Shaker Shiran, B. Al-Shakry, and T. Skauge, “Polymer Flow in Porous Media: Relevance to Enhanced Oil Recovery,” *Colloids and Interfaces*, vol. 2, no. 3, p. 27, 2018.
- [34] T. Skauge *et al.*, “Radial and Linear Polymer Flow - Influence on Injectivity,” *Soc. Pet. Eng. J.*, no. April, 2016.

- [35] P. G. De Gennes, “Coil-stretch transition of dilute flexible polymers under ultrahigh velocity gradients,” *J. Chem. Phys.*, vol. 5030, no. August 2003, pp. 5030–5042, 1974.
- [36] N. Zamani, I. Bondino, R. Kaufmann, and A. Skauge, “Effect of porous media properties on the onset of polymer extensional viscosity,” *J. Pet. Sci. Eng.*, vol. 133, pp. 483–495, 2015.
- [37] E. Aker, K. J. Måløy, A. Hansen, and G. G. Batrouni, “A Two-Dimensional Network Simulator for Two-Phase Flow in Porous Media,” *Transp. Porous Media*, pp. 163–186, 1998.
- [38] M. Delshad, D. H. Kim, O. A. Magbagbeola, C. Huh, G. A. Pope, and F. Tarahhom, “Mechanistic Interpretation and Utilization of Viscoelastic Behavior of Polymer Solutions for Improved Polymer-Flood Efficiency,” *Soc. Pet. Eng. J.*, 2008.
- [39] W. J. Cannella, C. Huh, and R. S. Seright, “Prediction of Xanthan Rheology in Porous Media,” *SPE Annual Technical Conference and Exhibition*. Society of Petroleum Engineers, Houston, Texas, p. 16, 1988.
- [40] N. Zamani, I. Bondino, R. Kaufmann, and A. Skauge, “Computation of polymer in-situ rheology using direct numerical simulation,” *J. Pet. Sci. Eng.*, vol. 159, no. April 2016, pp. 92–102, 2017.
- [41] G. Chauveteau, “Molecular Interpretation of Several Different Properties of Flow of Coiled Polymer,” *56th Annu. Fall Tech. Conf. Exhib. Soc. Petroleum Eng. AIME*, 1981.
- [42] B. Vik *et al.*, “Viscous Oil Recovery by Polymer Injection; Impact of In-Situ Polymer Rheology on Water Front Stabilization,” *SPE Europec featured at 80th EAGE Conference and Exhibition*. Society of Petroleum Engineers, Copenhagen, Denmark, p. 21, 2018.

Appendix A

A.1: Adverse Viscosity Ratio extended to 2.5 PV injected

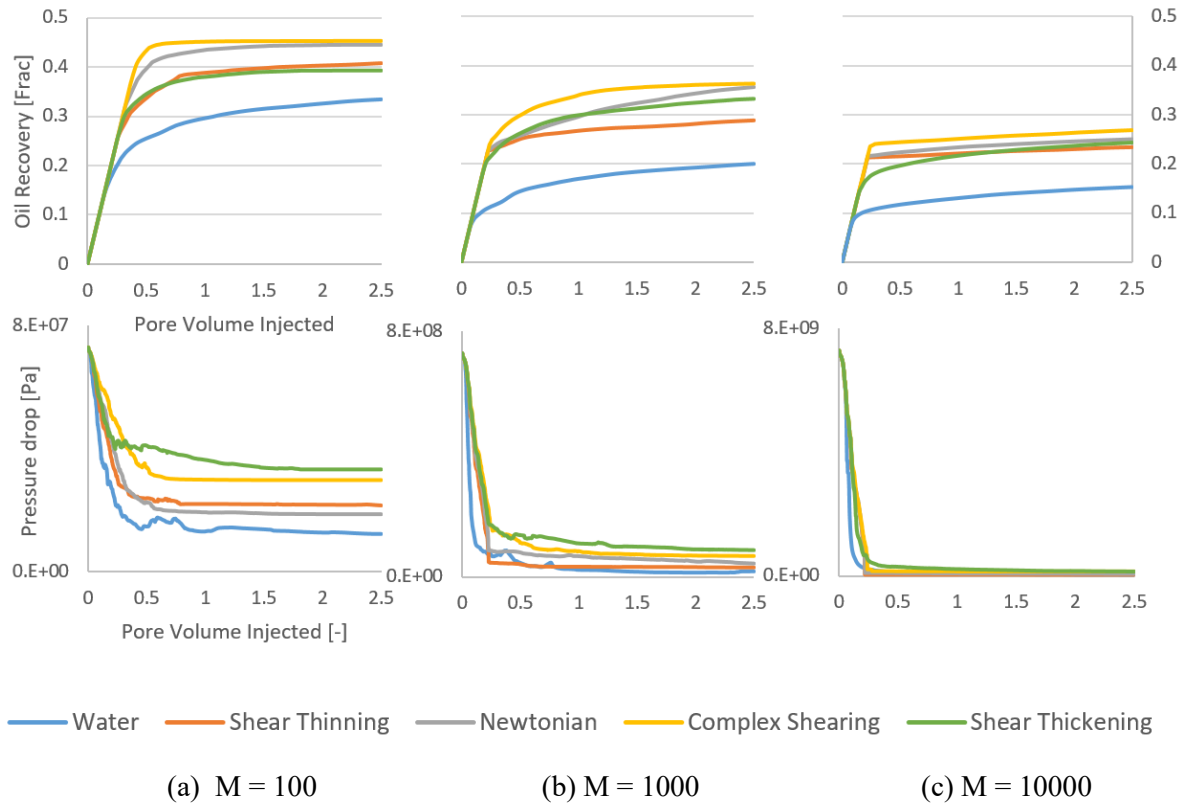


Figure A.1: Oil recovery and differential pressure vs. pore volume injected for adverse viscosity ratios (a, b and c). Extended to 2.5 pore volume.

The simulations were re-run for 2.5 PV injected to see if the polymer rheology models converge. There was little change in oil recoveries for (a) and (c), but some increased oil recovery for the Newtonian rheology for (b) $M = 1000$.

A.2: Pressure spike in 2D model: 100 x 25 x 1

A spike in pressure was observed for the shear thickening rheology model in Figure 7.33. Differential pressure is closely linked with the switch parameter, which relates the balance between capillary and viscous forces (Eq. 6.1). Figure A.2 shows the switch parameter and pressure plotted against PV injected.

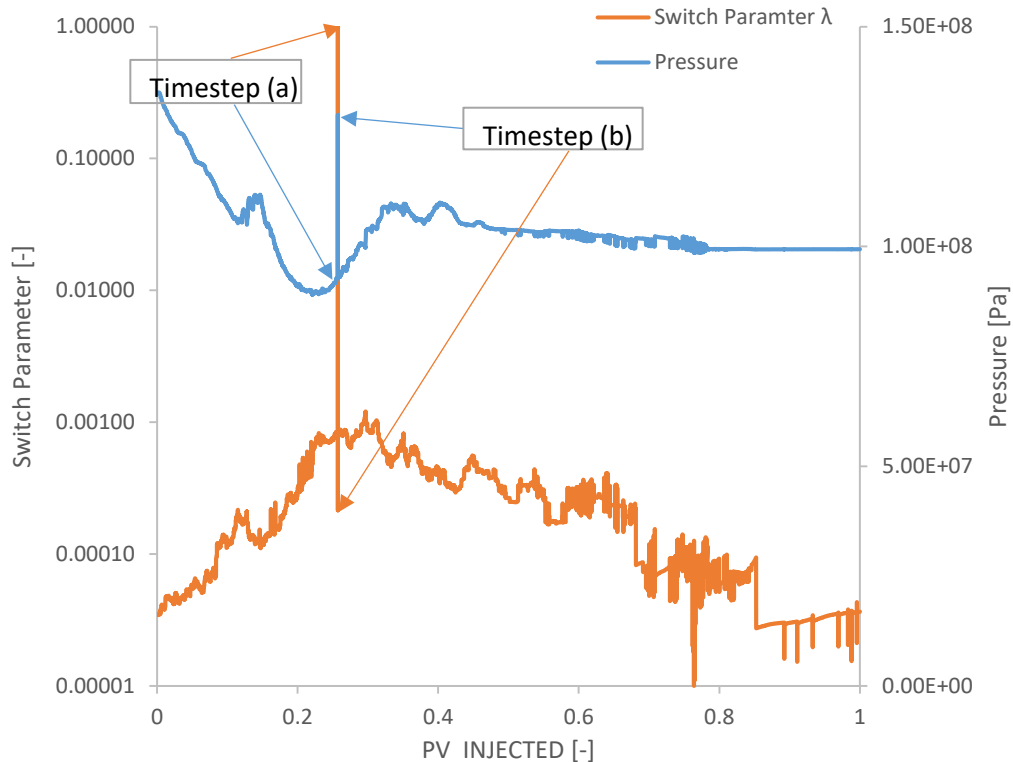


Figure A.2: Switch parameter (orange) and pressure (blue) vs. pore volume injected.

Figure A.2 reveals that in timestep (a), the switch parameter suddenly spikes to 1, which means the displacement is only occurring by snap-off. Also, because the code only allows for a maximum of one bond-filling per timestep, this is likely due to a particular bond in the network. At the following timestep (b), the pressure increases substantially, leading to a natural drop in the switch parameter. It is not clear why this pressure-anomaly occurred in the results (Chapter 7.6), but it looks to correlate nicely with the switch parameter.

